In Vitro Reconstitution of the Anaphase Central Spindle

Jonathon Hannabuss

University College London

and

The Francis Crick Institute

PhD Supervisor: Dr Thomas Surrey

A thesis submitted for the degree of

Doctor of Philosophy

University College London

October 2017

Declaration

I Jonathon Hannabuss, confirm that the work presented in this thesis is my own. Where information has been derived from other sources, I confirm that this has been indicated in the thesis.

Abstract

The anaphase central spindle is the major regulatory scaffold for coordinating cytokinesis; the final stage in cell division. It is constructed from two populations of microtubules, which emanate from opposite halves of the cell, until they meet at the centre, form antiparallel overlaps, and are cross-linked by microtubule bundling proteins. This cross-linked overlapping region marks the division plane, and recruits proteins that promote the membrane cleavage furrow, and the final abscission of the two daughter cells. For robust cortical signalling, and localisation of the abscission apparatus, the cell must regulate the length and alignment of the overlapping region to create a clear narrow band. What are the molecular mechanisms underlying this regulation? To address this question, I use a novel assay, which allows me to use TIRF microscopy to study free-floating, dynamic, microtubule bundles, nucleated *de novo* in solution, and organised by purified recombinant proteins. By reverse engineering the anaphase central spindle in this way, I have discovered that only two human central spindle proteins, PRC1 and KIF4a, are necessary to organise dynamic microtubules into bundled structures with narrow, aligned, antiparallel overlaps. These results also suggest a novel functional role for human KIF4a, as an antiparallel sliding motor, capable of aligning microtubule overlaps in a bundle.

Impact Statement

Cells in cancerous tissues are commonly found to contain more than two homologous sets of chromosomes; they are polyploid. This can encourage further mutagenesis, and lead to a more aggressive, drug resistant form of malignant cancer. Polyploidy is a sign that cells have begun the process of cell division, but have failed to complete it. Failure to assemble a robust central spindle, the major regulatory scaffold for cytokinesis, has been shown to lead to failed cell division, and polyploid cells. How then does a cell build and maintain such an important structure? This work helps to answer that question by shining a light on the underlying molecular mechanisms. The two major proteins studied in this work, PRC1 and KIF4a, have both recently been recognised as potential diagnostic markers for several different types of cancer, but their roles in cancer pathology are as yet poorly understood. I hope this work will aid in that understanding.

In this work I present a novel assay, which allows for the study of free floating microtubules by TIRF microscopy. I hope this work will help others in the cytoskeleton field, and potentially beyond, to study the self-organisation of free floating structures using TIRF microscopy. I have also shown how this technique can be used to study microtubule bundles. Microtubule bundles are important for many systems. They play a vital role in neurons, and are key participants in the development of neurodegenerative disease. Assays such as the one outlined in this thesis may be adapted to help better understand the inner workings of neurons, and other systems, which rely on the organisation of microtubule bundles.

This work also postulates a new way of thinking about human KIF4a, as a functional sliding motor. This may help to explain some of the as yet unexplained sliding forces apparent in anaphase central spindles.

Acknowledgements

I would firstly like to thank my PhD supervisor, Thomas Surrey, for allowing me to join his lab, for teaching me how to think like a scientist, his tremendous patience, and for always having an open door. I am grateful to Carolyn Moores and Steve Royle for agreeing to examine my thesis. I am grateful to my thesis committee, Mark Petronczki, Frank Uhlman and Nathan Goehring, for their encouragement and input throughout my PhD.

I would like to thank the members of the Surrey lab, past and present, for all their support. I especially want to thank: Iris Lueke, for teaching me most of what I know about cloning and protein expression; Hella Baumann and Nicholas Cade, for teaching me what a microscope is and which way up the slides go; Nicholas Cade, for fixing the microscope when I forgot how to use one, and also for programming the imageJ macros used in this thesis, and showing me how to use Origin; Frank Fourniol, for giving me the viruses for PRC1 and KIF4a used in this thesis, and for teaching me how to do TIRF microscopy assays; Johanna Roostalu, for giving me the virus for CAMSAP3ΔN used in this thesis, but mostly for being the fountain of knowledge on which we all rely; Claire Thomas, for coordinating the many tubulin preps that made the tubulin used in this thesis; Julian Gannon, for ordering all the stuff I needed to complete my thesis, and telling me where its kept, again; Tanja Consolati, Rupam Jha, Jayant Asthana, Einat Schnur, Mike Juniper, Todd Fallesen, Christel Michel, Jamie Rickman, Dalia Gala and Gil Henkin for all their valuable help and support, and sometimes cake.

I would like to thank Lottie, my girlfriend, for her tireless love and support and encouragement throughout my PhD. Whenever I was down, she picked me up, and got

me fighting again. I couldn’t have made it this far without her. I would like to thank my parents, for providing me with everything I needed to get here, and the freedom to have my own mind. If you give a man a rod and some fish, he’ll have the time and energy to come up with a better rod. To all my friends and family: thanks for all the fish.

‘What I cannot create, I do not understand’

- Richard Feynman

Table of Contents

Declaration 2
Abstract 3
Impact Statement 4
Acknowledgements 6
Table of Contents 9
Table of Figures 13
List of Tables 16
Chapter 1: Introduction 17
1.1 Mitosis and the Cell Cycle 17
1.1.1 The Cell Cycle 17
1.1.2 Mitosis 18
1.1.3 The Anaphase Central Spindle 20
1.2 The Microtubule Cytoskeleton 23
1.2.1 Microtubule Structure 23
1.2.2 Microtubule Dynamics 23
1.2.3 Microtubule Nucleation 25
1.3 MAPs and Motors of the Central Spindle 27
1.3.1 Kinesins and Dynein 27
1.3.2 KIF4a 29
1.3.3 Centralspindlin 30
1.3.4 PRC1 31
1.4 The Microtubule Mass of the Spindle 32
1.4.1 The Source of the Spindle 32

1.4.2 Controlling Spindle Length and Symmetry 33
1.5 Sliding and Braking in the Central Spindle 34
1.5.1 Anaphase B 34
1.5.2 Resisting Cortical Pulling Forces: PRC1 and Centralspindlin 35
1.5.3 Chromosome Separation in Mammalian Central Spindles 36
1.6 Constructing an Anaphase Central Spindle: Measuring the Overlap 37
1.6.1 KIF4a Recruitment to the Central Spindle 38
1.6.2 The End Caps Model 39
1.6.3 The Steady State Overlap Model 40
1.6.4 The Slide and Brake Model 41
1.7 Summary and Aims 42
Chapter 2: PRC1 and KIF4a: Interactions with Each Other and Microtubules 46
2.1 Purification of Fluorescently Labelled Proteins for use in Total Internal Reflection Fluorescence (TIRF) Microscopy 46
2.2 Higher Salt Concentrations Reduce the Size of KIF4a/PRC1 End Caps 49
2.3 PRC1/KIF4a Interaction Increases Affinity for Microtubules, and Decreases KIF4a Run Velocity 52
2.4 Hs.KIF4a Can Turn Off MT Dynamics in MSB but Not HSB 54
2.5 Discussion 58
Chapter 3: Self Organisation of Microtubule Bundles by KIF4a and PRC1 61
3.1 Solution Nucleated MTs Are Organised Around MT Seeds in the Presence of KIF4a and PRC1 in Mid Salt Buffer 61
3.2 Removing the Seed 66
3.3 Reducing KIF4a Concentration Prevents Sliding 69
3.4 Increasing PRC1 Concentration Inhibits Sliding 72
3.5 KIF4a Requires PRC1 to Crosslink Microtubules 74
3.6 Spindle Growth Caused By Minus End Growth 78

3.7 Spindles Actively Fuse and Align With One Another 79
3.8 Discussion 82
Chapter 4: A Model of Self-Organising Microtubule Bundles 85
4.1 Collecting and Measuring Data 85
4.2 Increasing PRC1 concentration and reducing KIF4a concentration increases overlap length 88
4.3 PRC1/KIF4a ratio correlates with overlap length 92
4.4 KIF4a per microtubule tracks overlap length 97
4.5 Discussion 100
Chapter 5: Materials and Methods 104
5.1 Gel Electrophoresis 104
5.2 Protein Expression 104
5.3 Protein Purification and Labelling 105
5.3.1 Purification of KIF4a-mGFP and KIF4a-mBFP 105
5.3.2 Purification of PRC1-SNAP 108
5.3.3 Purification of mCherry-CAMSAP3ΔN 110
5.3.4 Tubulin Purification and Labelling 112
5.4 Slide Preparation and Surface Chemistry 112
5.4.1 Covalent Passivation of Coverslips with PEG and Biotin-PEG 112
5.4.2 Preparation of Flow Cells 113
5.5 Preparation of GMPCPP Seeds 114
5.6 *In vitro* Microscopy: Buffers 115
5.7 *In vitro* Microscopy: Assays 116
5.7.1 Dynamic Seed Assays (Fig 2.7 and 2.8) 116
5.7.2 Non-Dynamic Seed Assay (Fig 2.3, 2.4 and 2.5) 117
5.7.3 Single Molecule Assay 117

5.7.4 Self-Organisation Assay (Figures from chapter 3 onwards) 117
5.7.5 FRAP Experiments 118
5.8 Kymograph Tracking 118
5.9 Data Analysis 119
5.9.1 Kymograph Analysis 119
5.9.2 End Point Analysis 121
5.9.3 Measuring Microtubule Growth Rates and KIF4a Run Velocities 123
5.8 General Computer Software 123
Chapter 6: Future Directions 125
Appendix 1 128
Appendix 2 129
Reference List 132

Table of Figures

Figure 1.1: Schematic of the cell cycle 17

Figure 1.2: Schematic of the phases of mitosis.....19

Figure 1.3: Schematic Illustration of an Anaphase Central Spindle 21

Figure 1.4: Schematic of a growing and shrinking microtubule.....24

Figure 1.5: In vitro microtubule nucleation 26

Figure 1.6: ATP cycle of a processive kinesin motor protein.....28

Fig 1.7: Schematic Illustration of Central Spindle Length Control by KIF2a and Aurora B Kinase 33

Figure 1.8: Schematic demonstrating the end caps model.....39

Figure 1.9: Schematic demonstrating the steady state overlap model 40

Figure 1.10: Schematic demonstrating the slide and brake model.....42

Figure 2.1: Schematic illustrating TIRF microscopy of surface-attached MT seed ..47

Figure 2.2: Coomassie gel of purified proteins.....48

Figure 2.3: Behaviour of PRC1 and KIF4a in Low Salt Buffer.....50

Figure 2.4: Behaviour of PRC1 and KIF4a in High Salt Buffer at high protein concentration.....51

Figure 2.5: Behaviour of PRC1 and KIF4a in Mid Salt Buffer at high protein concentration.....52

Figure 2.6: KIF4a-mGFP slowed down by PRC1-Alexa546 binding and transport in single molecule experiments.....53

Figure 2.7: Examples of MT buckling in antiparallel overlaps 55

Figure 2.8: KIF4a suppresses MT dynamics in MSB.....57

Figure 3.1: Solution-nucleated MTs self-organise overlaps around surface fixed GMPCPP seeds 62

Figure 3.2: 4 colour TIRF microscopy shows solution-nucleated MTs self-organising around surface fixed GMPCPP seeds.....64

Figure 3.3: Solution-nucleated MTs land antiparallel on GMPCPP seeds, and are transported to plus ends by KIF4a and PRC1 65

Figure 3.4: Characteristic end point of the KIF4a/PRC1 Self-Organisation Assay...67

Figure 3.5: De novo, dynamic MTs self-organise into polar spindles in presence of PRC1 and KIF4a 68

Figure 3.6: Reduction in KIF4a concentration leads to loss of dynamic suppression and sliding.....69

Figure 3.7: Kymograph tracking software produces kymographs from moving objects 70

Figure 3.8: Kymographs of KIF4a reduction experiments 71

Figure 3.9: Increasing PRC1 concentration resists sliding, decreasing rescues it. 73

Figure 3.10: PRC1 is incapable of sliding or controlling MT growth in the absence of KIF4a 75

Figure 3.11: PRC1 selects for antiparallel overlaps.....76

Figure 3.12: KIF4a alone is incapable of crosslinking microtubules.....77

Figure 3.13: Addition of CAMSAP demonstrates the importance of minus-end growth for determining the length of the mini-spindle 78

Figure 3.14: FRAP experiments demonstrate a lack of growth and sliding 79

Figure 3.15: Overlaps move towards the plus-ends of naked MTs to find and align with others 80

Figure 3.16: Steric hindrance leads to buckling in mini-spindle fusion events 81

Figure 4.1: Overlaps have mostly stabilised by the time of end point analysis 86

Figure 4.2: Box plots of overlap length and Tubulin, KIF4a and PRC1 Total intensities 88-89

Figure 4.3: Scatter plots comparing overlap length with tubulin total intensity and density 91

Figure 4.4: Scatter plots comparing overlap length with PRC1/KIF4a concentration and total intensity ratios 93

Figure 4.5: Box plots of PRC1 and KIF4a total intensities / total tubulin intensity ..95

Figure 4.6: Box plot of KIF4a total intensity/ tubulin density 96

Figure 4.7: Line plots comparing overlap length and PRC1/Tubulin ratio over time 98

Figure 4.8: Line plots comparing overlap length and KIF4a/Tubulin density over time.....99

Figure 4.9: Schematic demonstrating the KIF4a steady state end caps mechanism ..101

Figure 5.1: Analysis of the purification of KIF4amBFP and KIF4amGFP 107

Figure 5.2: Analysis of the purification of PRC1-SNAP 109

Figure 5.3: Analysis of the purification of mCherry-CAMSAP3ΔN.....111

Figure 5.4: Example images taken from data measurement process 120

Figure A1: Heatmap of correlation coefficients comparing different variables.....128

List of Tables

Table 5.1: Table presenting the number of events included in end point analysis for each concentration condition.....122

Table A2.1: Table presenting mean values for different protein concentration conditions comparing maximum and end point (EP) values of $PRC1_{Int}/Tub_{Int}$ taken from kymograph data with non-illuminated end point values 129

Table A2.2: Table presenting mean values for different protein concentration conditions comparing maximum and end point (EP) values of $PRC1_{Int}$ taken from kymograph data with non-illuminated end point values.....130

Chapter 1: Introduction

1.1 Mitosis and the Cell Cycle

1.1.1 The Cell Cycle

In order for multi-cellular eukaryotic organisms to grow, repair and reproduce, their constituent cells must divide. The process by which this happens is called the cell cycle, and it is traditionally divided into four main phases: G_1, S, G_2 and M phases (Fig 1.1). G_1, S and G_2, are collectively referred to as interphase [4]. The two G phases (G_1, and G_2) are characterised by growth of the cell. In between these phases is S phase, which is characterised by the duplication of the DNA in the cell nucleus to give two cohesin-bound sister chromatids, and the duplication of the cell's centrosome in the cells cytoplasm. Centrosomes act as nucleating sites for microtubules, dynamic cellular fibres which form the spindle apparatus responsible for positioning and dividing the sister chromatids in the

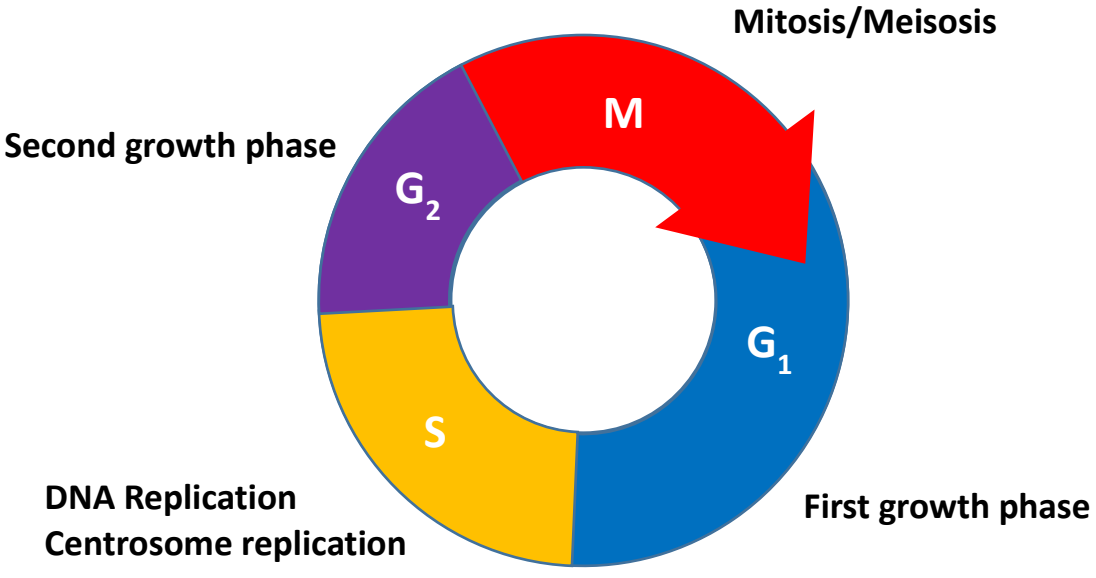

Figure 1.1: Schematic of the cell cycle
Schematic illustrating the order of the cell cycle from G_1 to S to G_2 to M phase.

final stage of the cell cycle, M-phase (Fig 1.2) [5-7]. Most cells entering M-phase will undergo mitosis, in which cells perform a single division to give two diploid cells. In the production of gametes, however, cells undergo meiosis, in which cells undergo two sequential divisions to give four haploid daughter cells [8].

The master regulators of the cell cycle are the cyclin dependent kinases (Cdks) and their cyclin counterparts [9, 10]. There are four primary Cdks in vertebrates responsible for the cell cycle. Cdk4, Cdk6 and Cdk2 are responsible for regulation during interphase, whereas Cdk1 is responsible for regulation during M-phase, and as such will feature in our understanding of mitotic cell division.

1.1.2 Mitosis

As with the cell cycle as a whole, mitosis can also be conceptualised into sequential phases: prophase, prometaphase, metaphase, anaphase, telophase and cytokinesis (Fig 1.2) [11]. During interphase, DNA is in the form of chromatin, where it is coiled around complexes of histone proteins called nucleosomes. At the onset of prophase, however, SMC complexes further condense this chromatin into the familiar X-shaped mitotic chromosomes, ready for segregation [12-14]. The exact way in which the chromatin is structured in these chromosomes remains an active area of research. Up until this point, the chromosomes have been contained within the cell nucleus, but as prophase leads to prometaphase, the nuclear envelope breaks down, releasing the condensed chromosomes, along with proteins important for the subsequent stages of mitosis, into the cytoplasm [15]. Once in the cytoplasm, the microtubules of the bipolar spindle can bind to the chromosomes via their kinetochores. In mammalian cells, each sister chromatid has a single kinetochore, a highly complex layered protein structure [16-18]. The kinetochore is built on the centromere, itself a complex hierarchical protein structure, which forms at a

specific area of chromatin containing a special histone, CENP-A [17, 19]. Though centromeres, and many kinetochore components are already present before the onset of mitosis, many kinetochore components are recruited only after chromosome condensation. The attachment of the microtubules of the bipolar spindle to the kinetochores of sister chromatids, and the subsequent alignment of those sister chromatids down the cell equator characterises metaphase [20, 21]. At this stage of mitosis the cell is prevented from progressing into anaphase by the spindle assembly checkpoint [18, 22, 23]. Only when all kinetochores are successfully attached to opposite poles via the bipolar spindle can the cohesin binding sister chromatids be cleaved, and the sister chromatids be separated into opposite halves of the cell, helping to prevent any errors in chromosome segregation. This segregation of the chromosomes, and increase in the pole to pole distance, characterise anaphase A and B respectively [24, 25]. Chromosome segregation away from the cell equator is followed by cleavage of the cell membrane along the cell

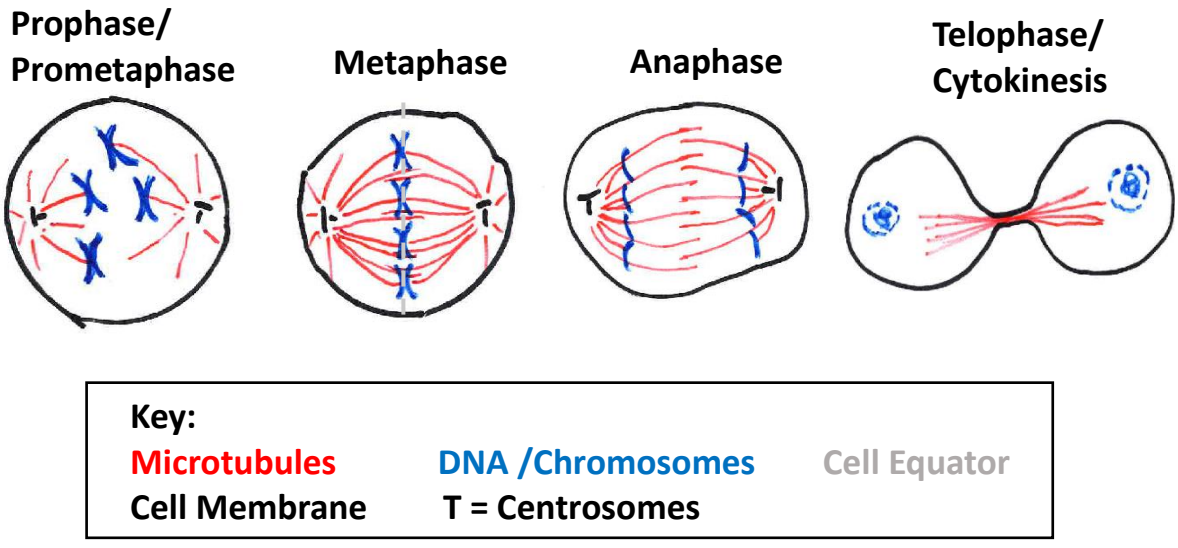

Figure 1.2: Schematic of the phases of mitosis
Schematic showing the various stages of the cell cycle, and the positioning of the microtubule spindle (red) and DNA (blue) at the different stages. The cell equator is marked with a grey dotted line. Centrosomes are marked with a black T shape, and the black outer boundary represents the cell membrane.

equator, until it meets in the middle, forming the midbody [26, 27]. Telophase is characterised by the formation of a new nuclear envelope around each complete set of chromosomes, and typically follows the onset of membrane cleavage [15]. The final stage of mitosis is cytokinesis, where the abscission of the membrane takes place to give two new daughter cells [28, 29].

1.1.3 The Anaphase Central Spindle

How does the cell know where the cleavage of the membrane should take place, and how does it accumulate the components necessary for abscission in the centre of the cell? The answer is that it forms what is known as the central spindle. The central spindle is a microtubule based structure, which forms in between segregating chromosomes during anaphase where the two sets of microtubules, emanating from opposite halves of the cell, overlap, and become arranged into antiparallel bundles by various microtubule associated proteins (MAPs) and motor proteins [29-32] (Fig 1.3). The central spindle is widely regarded as a key regulating centre for cytokinesis, recruiting proteins for successful cleavage furrow positioning and membrane abscission. For these important roles to be achieved successfully, the central spindle has to be carefully regulated to control the size of the microtubule overlap region, the alignment of those overlaps and the overall length and symmetry of the structure. Without this regulation, signalling faults in cytokinesis can occur, resulting in unequal chromosome segregation or polyploid cells, greatly increasing the risk of cancer [33].

The start of anaphase, and central spindle formation, is signalled by the anaphase promoting complex (APC^{Cdc20}) [34]. This complex acts as a ubiquitin ligase, which tags proteins for degradation including cohesin [35]. The most important APC^{Cdc20} target for the

organization of the microtubule spindle is cyclin-B, a protein needed to activate Cdk1. As mentioned above, Cdk1 is commonly seen as the master regulator of mitosis, as its activation triggers mitotic entry, and its depletion, mitotic exit. Many Cdk1 substrates are involved in the regulation of the pre-anaphase bipolar spindle, and the anaphase central spindle. Depletion of Cdk1 before the cell is ready to enter anaphase is lethal, as proteins important for the structural integrity of the metaphase spindle are depleted by dephosphorylation [36, 37], whilst others involved in the formation of the anaphase spindle are activated or relocalised [38-40], causing fatal disruptions in chromosome alignment [41].

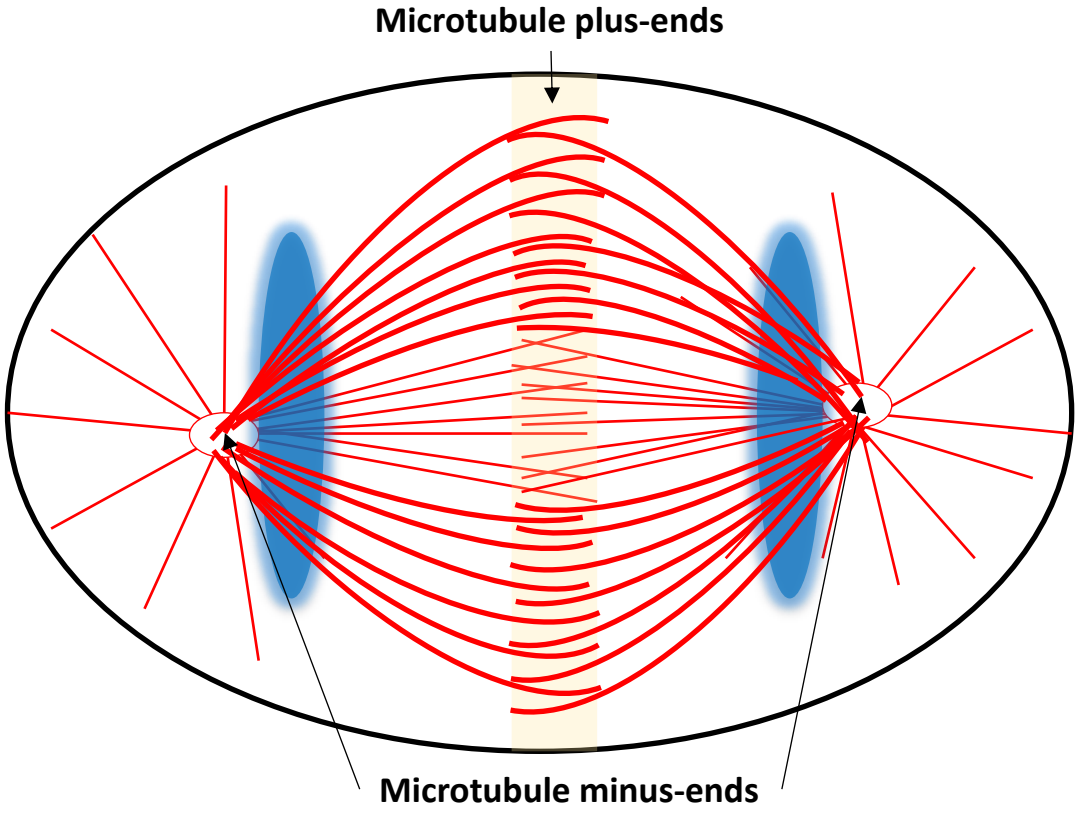

Fig 1.3: Schematic Illustration of an Anaphase Central Spindle
Schematic showing the structure of the central spindle, with microtubule (red) plus-ends emanating from opposite halves of the cell overlapping in between segregated chromosomes (blue) to form a regulatory scaffold (yellow) that recruits factors involved in cleavage furrow initiation and membrane abscission.

From the perspective of the microtubules, the deactivation of Cdk1 is like the setting of the sun, where the proteins and their roles change after dark.

This thesis is concerned only with the formation and regulation of the anaphase central spindle; the night time spindle. Because of the complex nature of cytokinesis, many proteins and regulators localize at the central spindle during anaphase, and they can have multiple overlapping functionalities, making it highly challenging to extract the molecular mechanisms regulating the structural integrity of the spindle itself. Excellent work in the area of cell and structural biology has elucidated some of the key proteins necessary for central spindle formation, and the interactive and regulatory networks in which they operate [30, 31]. Some of these proteins will be directly responsible for constructing the central spindle, but others may only be necessary to resist external disruptors, be they proteins, such as microtubule depolymerases [3], or forces, such as cortical pulling forces that will try to pull the overlapping microtubules apart [42]. Elucidating the intrinsic properties of important central spindle associated proteins, and how these function together to construct a central spindle, will require complimentary methods. I have chosen to use *in vitro* reconstitution to study the formation of the central spindle. This method builds minimal systems outside of the cell, using purified recombinant proteins, in an attempt to reverse engineer dynamic molecular systems. To build a central spindle in this way, I must first hypothesise what the minimal number of central spindle components could be to build a minimal central spindle structure *in vitro*. The most important component of the central spindle, and one which I must include in my minimal reconstitution, is its major structural constituent: microtubules.

1.2 The Microtubule Cytoskeleton

1.2.1 Microtubule Structure

Microtubules are dynamic polymer filaments involved in a variety of cellular processes, including, but not limited to: intracellular transport [43], neuronal plasticity [44], the structure of cilia [45], chromosome segregation [24, 25], and the coordination of cytokinesis [29]. They consist of multiple single stranded protofilaments of the αβ-tubulin heterodimer protein, arranged to form hollow molecular tubes with a diameter of approximately 25 nm [46, 47] (Fig 1.4). Within the microtubule lattice, individual tubulin heterodimers experience both the longitudinal, head-to-tail, interdimer interactions of the protofilament, which occur in an α-β-α-β fashion; and the lateral interdimer interactions between protofilaments, which occur as α-α and β-β interactions. Additionally, each protofilament is longitudinally offset slightly from its neighbour, adding a helical twist to the microtubule. This twist necessitates a seam, which runs along the length of the microtubule, where the α-α and β-β lateral interactions are replaced with α-β interactions [48]. The unidirectional arrangement of the polar protofilaments translates into structural polarity for the microtubule as a whole, with an α-tubulin face at the so called 'minus-end', and a β-tubulin face at the 'plus-end'. These two faces show marked differences in their dynamic behaviour [49].

1.2.2 Microtubule Dynamics

Microtubules exhibit what is known as dynamic instability. This is characterized by stochastic switches between periods of polymerization, 'growth', and rapid shrinkage, 'catastrophe' [50] (Fig 1.4). This is as a result of GTP hydrolysis along the microtubule lattice [51]. Both α and β tubulin subunits bind to GTP, in the N- and E-site respectively, however, only the β bound GTP is capable of being hydrolysed, and as such, gives rise to

dynamic instability. GTP to GDP hydrolysis is very slow in the case of free unassembled tubulin, but GTP bound tubulin biases the assembly of microtubules, and GTP hydrolysis is better catalysed when heterodimers are incorporated into the microtubule lattice. Once hydrolysed, the now GDP tubulin may favour the free disassembled state, but it is unable to disassociate, as it is trapped in the lattice by lateral and longitudinal interactions on all sides. If, however, the rate of hydrolysis outstrips the on rate of new GTP tubulins, the 'cap' of GTP tubulin, which locks in the GDP tubulin behind it, will be hydrolysed, and

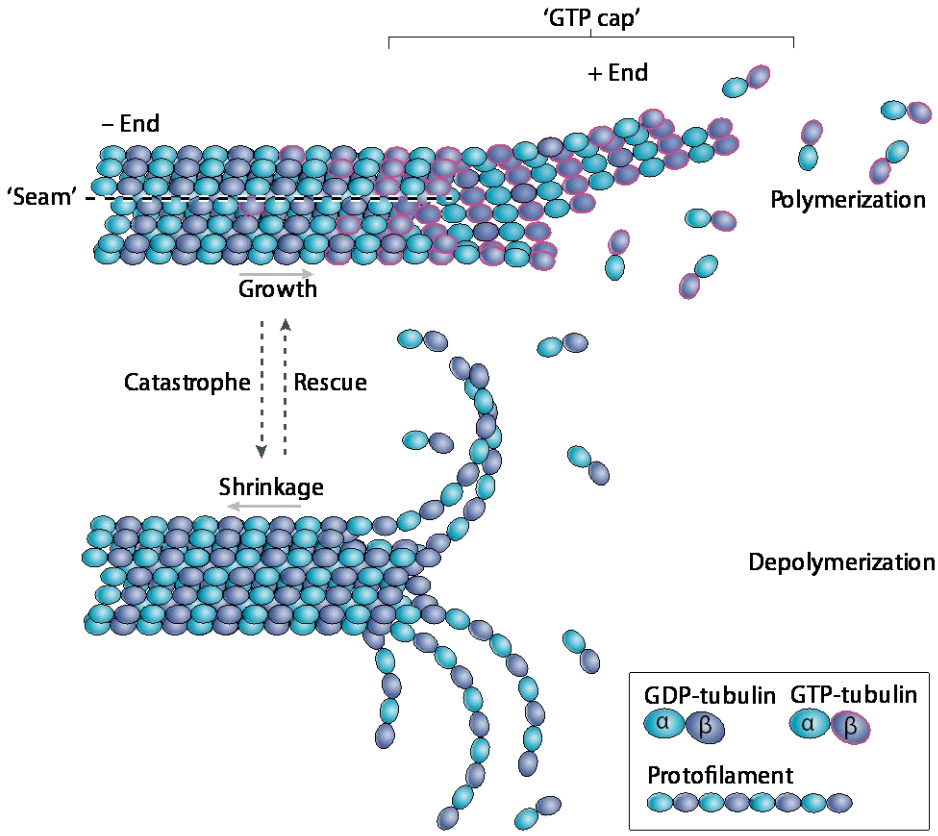

Figure 1.4: Schematic of a growing and shrinking microtubule

Schematic shows GTP tubulin being added to a microtubule plus-end. Figure adapted from Roostalu and Surrey, 2017 [2].

the microtubule will experience a catastrophe, as the protofilaments peel away, and dissolve back into free GDP bound tubulin heterodimers [52, 53].

Even though both plus- and minus-ends of the MT experience dynamic instability, as described above, the plus-ends of microtubules exhibit much faster rates of growth [49]. This is especially true in cells, where minus ends are more often capped by proteins that prevent growth, while plus-ends can interact with proteins that encourage it [54-57]. In spite of this, it would be wrong to assume that plus-ends are always free to grow in cells. Many proteins important for cell function bind to microtubule plus-ends, either directly or through interaction networks, and some of these proteins can suppress plus-end dynamics [58, 59]. The primary driver of the growth rate, in the absence of other proteins, is the free tubulin concentration, which shows a positive linear correlation with MT growth rate when measured in controlled *in vitro* experiments [60]. This is also true for minus ends *in vitro* where they are uncapped, as microtubules are typically grown from small stabilized seeds, made using non-hydrolysable variants of GTP, such as GMPCPP, or small molecule stabilizers, such as paclitaxel. Part of the reason minus-ends remain capped in cells is because the cap is what the MT has nucleated from in the first instance.

1.2.3 Microtubule Nucleation

In mammalian cells microtubules are primarily nucleated from a template called the γ-tubulin ring complex (γTuRC), and consequently consist of 13 protofilaments [7]. However, microtubules do not require such a template to nucleate, and can form spontaneously in the presence of GTP and Mg^{2+} ions, in buffer, outside of the cell, from purified tubulin heterodimers [60]. Spontaneous nucleation, *in vitro*, can lead to varying protofilament numbers, with a mean of 14 for mammalian brain tubulin, as measured by electron microscopy [61]. Nucleation in this way requires several thermodynamically unfavourable steps to reach a structure from which microtubules can grow from (Fig 1.5). This stable nucleus has been estimated to consist of around 5-20 tubulin heterodimers, independent

of tubulin concentration [60]. It is possible to lower the barrier to nucleation by increasing the tubulin concentration, but this will also increase the growth rate of your MTs once they have nucleated. You could also fix the tubulin in a GTP-bound state using unhydrolyzable GMPCPP, but this will drastically alter MT dynamics by effectively preventing disassembly [62]. Small molecules which enhance interdimer interactions, and can stabilize the intermediate structures, are also predicted to lower the nucleation threshold, but may not affect dynamics in the same way as increasing the tubulin concentration, or blocking GTP hydrolysis.

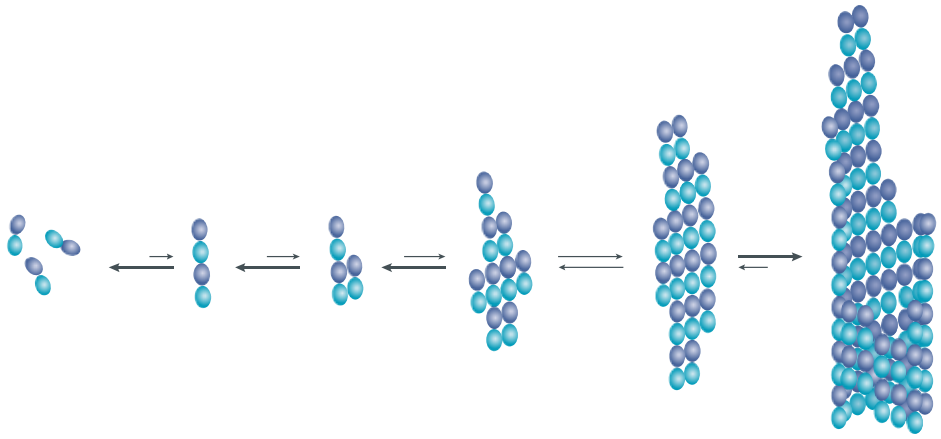

Figure 1.5: In vitro microtubule nucleation
Schematic shows the spontaneous formation of a microtubule via a series of thermodynamically unfavourable events. Figure adapted from Roostalu and Surrey, 2017[2].

Another way in which nucleation can be controlled is temperature. MT nucleation is an entropically driven process, and so keeping solutions on ice can prevent nucleation, whereas warming them can trigger it [63]. This is commonly used with *in vitro* experiments where sample solutions are kept on ice, before being placed on the warm microscope, so data can be collected from the onset of MT nucleation. This entropic drive translates into

a force, which the MT can excerpt as it grows, to push against membranes, organelles and other cell bodies [59].

1.3 MAPs and Motors of the Central Spindle

1.3.1 Kinesins and Dynein

Kinesins are a large group of microtubule-dependent motor proteins important for utilizing and regulating microtubules for cell functions, such as transport of cargos along microtubules [43], sliding microtubules over one another to separate poles during cell division [6, 64], and controlling microtubule dynamics [59]. There are 45 kinesin genes in the mammalian genome, and these are further divided into 14 kinesin families, which reflect their evolutionary lineage, and as a result, their associated structure and behaviour [65, 66].

All mammalian kinesins contain a motor domain capable of hydrolysing ATP to do work, which, with the exceptions of the kinesin-13s and -14s, resides at the N-terminus of the protein sequence [67]. For the majority, this work is used to drive the stepping of kinesins along microtubules with a specific directionality, usually towards the MT plus-end. The exceptions to this are the Kinesin-14s, which have their motor domain at the C-terminus, and walk towards the MT minus-end [68]. The major minus-end directed motor in the cell, however, is not a kinesin motor at all, it is dynein. Unlike the kinesins, where evolution has provided diversity of function by having a menagerie of motors, with dynein, it has provided diversity of function by having one large motor complex, and a menagerie of activators, which alter what dynein binds to, and how it functions [69, 70]. The most important motors for central spindle assembly are members of the kinesin-4 and kinesin-6 families. Members of these two families are typically plus-end directed, homodimeric, and have an N-terminal motor domain [71, 72].

Homodimeric kinesins consist of two N-terminal motor domains tethered, via a necklinker, to a coiled coil domain, the domain responsible for the homodimerisation, and ending with a C-terminal tail [67]. The motor domain binds to the microtubule in the intradimer site, contacting both α and β tubulin [73]. Binding of ATP to the MT bound motor head causes a conformational change in the necklinker, which causes the other, ADP-bound, motor head to swing forward. At this stage, weakly processive kinesins are prone

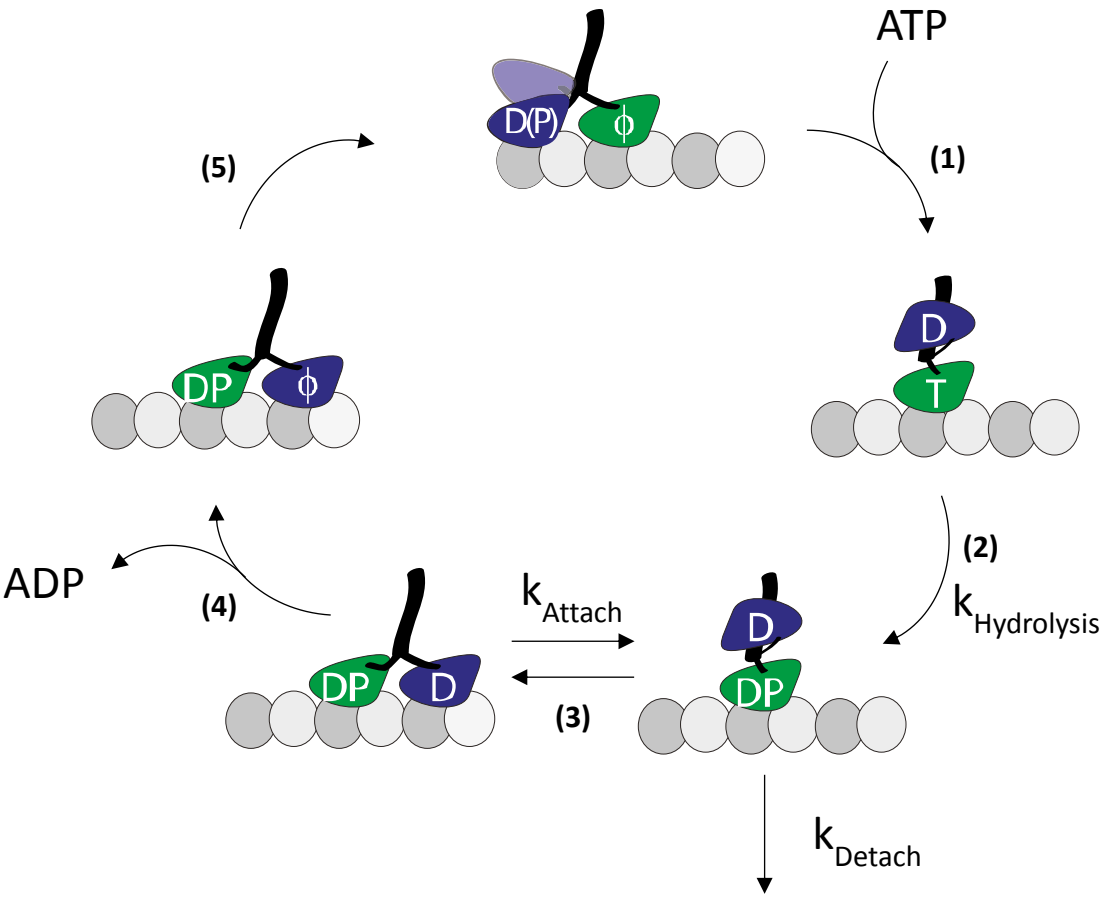

Figure 1.6: ATP cycle of a processive kinesin motor protein
From top going clockwise: (1) Phosphate release causes the lagging motor head to unbind thrusting it forwards. ATP binds to the MT bound motor. (2) ATP is hydrolysed by the motor domain, but free Pi remains bound. (3) Equilibrium between bound and unbound states of the ADP bound motor domain. At this stage motors are vulnerable to the detachment of the bound ADP+Pi head. (4) ADP release locks in binding of the previously unbound motor domain. (5) Phosphate release begins the start of the next cycle. Figure adapted from Mickolajczyk and Hancock, 2017[1].

to detachment, possibly dependent on the competition between the reattachment of the tethered ADP bound motor head, and the hydrolysis and detachment of the ATP bound motor head [1]. Reattachment of the tethered motor head is locked in by the release of ADP, and the cycle begins again (Fig 1.6).

Though most kinesins exhibit this behaviour, they vary in their run velocity, MT affinity and processivity (the amount of steps it takes before falling off). This is in addition to their differing functionalities within the cell. The kinesin-5 proteins are homotetramers, capable of walking along two microtubules simultaneously, making them useful for cross-linking and sliding microtubules over one another [74]. The kinesin 13s are incapable of processive walking, being the only kinesins to have their motor domains in the middle of the amino acid sequence, and instead act as ATP-driven MT depolymerases [75]. This diversity of function allows the cell to control and manipulate microtubules to complete what is one of the greatest feats in nature, the division of a cell.

1.3.2 KIF4a

KIF4a, a kinesin-4 and the focus of this thesis, plays important roles in both metaphase and anaphase of cell division. Its C-terminal tail is capable of binding to DNA, a function it shares with the kinesin-10s, and it is involved in chromosome congression and alignment in the metaphase spindle [20]. During anaphase, KIF4a relocalises from the chromosomes to the central spindle. *In vitro* studies on both *X. laevis* and human KIF4a, have shown that alone it can accumulate at MT plus-ends and suppress plus-end dynamics [58, 76, 77]. In HeLa cells, KIF4a has been shown to limit overlap growth during anaphase [78, 79]. The precise molecular mechanism by which this occurs is unknown. KIF21B, another kinesin-4 which shows similar activity, suppresses microtubule dynamics with a

combination of the motor domain and a portion of its stalk domain [72]. KIF4a lacking the C-terminal tail appears capable of suppressing microtubule growth *in vivo* [79], and an N-terminal motor fragment of Xenopus KIF4a was shown to suppress microtubule dynamics *in vitro* [58]. Work by Kurasawa et. al. revealed that HeLa cells depleted of KIF4a had overgrown central spindles, and that this can ultimately lead to cytokinesis failure [78]. The human kinesin-8 KIF18A has also been shown to suppress plus-end dynamics *in vitro,* similar to KIF4a [80, 81], however, others suggest KIF18A acts as a microtubule depolymerase similar to kinesin-8s from other species, suggesting its intrinsic function may differ from that of the kinesin-4s [82, 83].

1.3.3 Centralspindlin

The centralspindlin complex is a heterotetramer consisting of a homodimeric, plus-end directed, kinesin-6, MKLP1, and a homodimeric RhoGAP, MgcRACGAP [84, 85]. MKLP1 has an unusually long neck-linker between its motor domain and its coiled coil, and it is in this necklinker region that MgcRACGAP binds [86, 87]. Both components are necessary for the formation of well organised central spindles in mammalian cells [88, 89]. Centralspindlin is a microtubule bundling protein which crosslinks microtubules in the central spindle both to each other, and, as cytokinesis progresses, to the cell cortex [87, 90]. The microtubule interaction of MKLP1 is Cdk1 inhibited during metaphase [40], and centralspindlin is further inhibited by binding to the 14-3-3 protein. Individual centralspindlins are not highly processive motors, but clusters of centralspindlins are able to processively move along microtubules, and accumulate at the overlapping plus-ends [91]. Aurora B kinase phosphorylation of centralspindlin releases 14-3-3, allowing it to form these processive plus-end directed clusters [92].

At the onset of anaphase, aurora B kinase is transported as a component of the chromosomal passenger complex (CPC) to the overlapping region by another kinesin-6, MKLP2, a process that is also negatively regulated by Cdk1 [39, 93, 94]. Aurora B kinase acts as a major regulator of the central spindle in cells [95].

1.3.4 PRC1

As well as motor proteins, cells also use a menagerie of non-motor microtubule associated proteins (MAPs) to utilise and manipulate the microtubule cytoskeleton for its needs. These include proteins that bind to microtubule ends, such as the EB proteins which bind and recruit others to microtubule plus-ends, or the CAMSAP proteins, which stabilise non-centrosomal microtubules by capping their minus-ends [54]. The most important MAP with regards to the central spindle, however, is PRC1. PRC1 is a homodimeric MAP that has a specific affinity for crosslinking and bundling antiparallel overlaps [76, 96-98]. Its homodimerisation domain is in its N-terminus, and its microtubule binding domain is a spectrin domain in the C-terminal half of the protein [98, 99]. When bound to a single microtubule, PRC1 is relatively flexible, allowing it to search for other microtubules. Once in an antiparallel overlap it becomes far more rigid. This is proposed to aid PRC1 in aligning microtubules antiparallel to one another [99]. Like MKLP1, its microtubule binding domain is negatively regulated by Cdk1 phosphorylation in metaphase [97]. Inactivation or depletion of PRC1 leads to the absence of a stable central spindle in cells [38, 78, 97]. PRC1 is important for recruiting other proteins important for central spindle integrity in cells, such as CLASP [100], KIF4a [78], and possibly aurora B, via an interaction with MKLP2 [101]. CLASP is a non-motor MAP that is thought to prevent microtubule catastrophes, and promote plus-end growth, making it important for spindle stability in an environment of microtubule depolymerases, and disruptive external forces [55, 102].

1.4 The Microtubule Mass of the Spindle

1.4.1 The Source of the Spindle

As mentioned above, the depletion of Cdk1 and the transition from metaphase to anaphase is accompanied by a transition from the metaphase bipolar spindle to the anaphase central spindle. But does the anaphase spindle require the metaphase spindle as a template around which to form? Is the anaphase spindle simply a repurposing of the microtubules already present in metaphase? Work by Uehara et. al. suggests that in wild type central spindles ~70% of the microtubules are generated *de novo* at the start of anaphase by way of the augmin complex, which, with the aid of the γ-tubulin ring complex, nucleates microtubules off of pre-existing microtubules [103, 104]. Augmin is a Y-shaped protein complex which angles the γ-tubulin ring complex in such a way as to nucleate microtubules in the same orientation as the source microtubule, meaning that spindles amplify, rather than lose, their polarity [105, 106]. In spite of this, central spindles have been shown to form in cells treated with microtubule depolymerases at metaphase, and were seen to successfully complete cytokinesis in ~30% of cases [107]. Experiments with Xenopus egg extract have shown that microtubule asters, nucleated from artificial centrosomes in the absence of chromosomes, or an existing metaphase spindle, can interact to form stable overlaps that recruit central spindle proteins [108]. It is, therefore, tempting to think that one could build a central spindle architecture *de novo* using purified recombinant proteins. Yet, it is worth noting that certainly in the latter case, the bipolar symmetry of the system has been pre-set by having microtubule plus-ends growing out from singular points. For my *in vitro* reconstitution, I will either need to use a similar sort of device, or add a molecular motor capable of polarity sorting microtubules.

1.4.2 Controlling Spindle Length and Symmetry

The central spindle is constructed in between segregated chromosomes, orienting the division plane, so as to give two new daughter cells, each with a single complete copy of the DNA. In order to position the division plane between segregated chromosomes, the central spindle must be able to position itself relative to them. If the minus-ends of the central spindle are too short, then the spindle is prone to rotation. If they are too long,

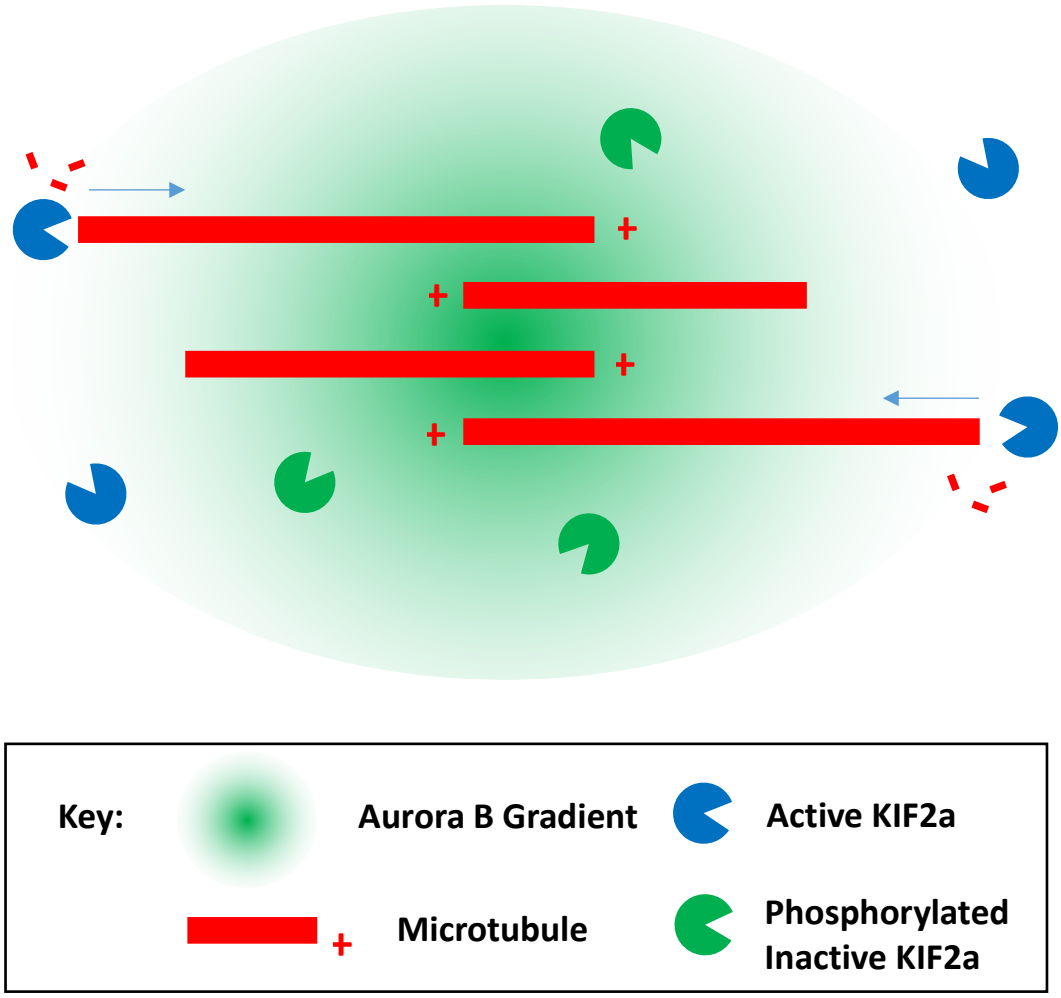

Fig 1.7: Schematic Illustration of Central Spindle Length Control by KIF2a and Aurora B Kinase
Schematic representing the model proposed by Uehara et. al. in which an aurora B gradient emanating from the overlap zone protects microtubule minus-ends from depolymerisation by the kinesin-13 KIF2a [3].

they are prone to buckling, which will twist the spindle, disrupting the overlapping region [3]. In order to control the lengths of the microtubules, the cell makes use of a microtubule depolymerase, KIF2a. KIF2a is a kinesin-13, which depolymerizes microtubule minus-ends. Depleting KIF2a at anaphase leads to cytokinesis failure, as overgrown central spindle microtubules buckle and distort the overlap zone [3]. It is believed that an Aurora B gradient emanates out from the overlap zone during anaphase, and deactivates KIF2a within a certain radius; thus controlling the overall length of the spindle (Fig 1.7) [3]. Length control is likely important when spindles are in enclosed confinements, such as cells, or artificial droplets [109, 110]. I intend to perform my *in vitro* experiments in bulk solution, however, and so may not require KIF2a, or indeed aurora B, though this is not the only role of aurora B in central spindle assembly.

1.5 Sliding and Braking in the Central Spindle

1.5.1 Anaphase B

Anaphase is commonly divided into two processes: anaphase A [25], the separation of the sister chromatids by depolymerizing kinetochore microtubules; and anaphase B [24], the separation of cell poles, which can be driven by pulling forces from the cortex, or antiparallel sliding forces from the central spindle. Whether from the cortex or the spindle, these forces have the potential to severely disrupt or destroy the central spindle overlap. The relative contributions of these two forces changes between species. *D. melanogaster* anaphase B is driven primarily by antiparallel sliding forces by the kinesin-5 KLP61F [111, 112], whereas *C. elegans* anaphase B is driven primarily by the result of dynein-driven pulling forces from the astral cortex [113]. Though microtubule minus-ends have detached from poles by the time of telophase, some of the microtubules that form the central spindle

are believed to remain attached to the poles, directly or indirectly, after anaphase B onset, and so will experience these pulling forces [103, 114].

1.5.2 Resisting Cortical Pulling Forces: PRC1 and Centralspindlin

Two key proteins resisting cortical pulling forces in *C. elegans* are the two proteins responsible for crosslinking the antiparallel microtubules: PRC1 and centralspindlin. As the major microtubule crosslinking proteins, PRC1 and centralspindlin have long been believed to be structurally integral to the central spindle. As mentioned above, the microtubule interactions of both are Cdk1 inhibited during metaphase [38, 40]. In *C. elegans*, RNAi depletion of either PRC1 or centralspindlin results in considerable central spindle disruption, and faster chromosome separation, though only two thirds of central spindles in cells depleted of centralspindlin actually broke apart, whereas nearly all central spindles in the PRC1 depleted cells did [115]. In both cases, simultaneous depletion of cortical pulling forces restored central spindle integrity, suggesting that in the absence of cortical pulling forces, centralspindlin may not be required to form a central spindle [116]. Work by Lee et. al. has shown that this braking of cortical-induced sliding is reliant on an interaction between PRC1 and centralspindlin [42], and that the amino acids involved in this interaction are conserved in the human proteins, for which an interaction has already been established in pull down assays [117].

In my minimal *in vitro* reconstitution there will be no cortical pulling forces, as there will be no cortex. Both PRC1 and centralspindlin have been shown to preference antiparallel overlaps, which will be important for the spatial polarity of the system, but it is not clear why I would require two antiparallel crosslinking motors? Centralspindlin is important in cytokinetic signalling pathways[90, 118, 119], but unlike PRC1, is not known to recruit any of

the other proteins important for central spindle assembly discussed here. I hypothesise that centralspindlin may be surplus to requirements in my experiments, though its clustering ability could be important for structural integrity across multiple overlaps.

As mentioned above, approximately a third of central spindles survived cortical pulling forces with PRC1 alone, whereas none did in the absence of PRC1. The yeast homologue of PRC1, Ase1, has been shown in controlled *in vitro* reconstitution experiments to act alone as a brake against motor sliding forces [120]. Optical trap experiments demonstrate how as overlaps are shortened, the Ase1 therein is retained and compressed, storing potential energy, which can be used to generate expansionary forces, which act to expand the overlap once the optically trapped microtubule has been released [121]. In agreement with *C. elegans*, however, human PRC1 alone was found not to brake antiparallel microtubule sliding driven by EG5 in controlled *in vitro* reconstitution experiments, albeit performed under differing buffer conditions. These *in vitro* experiments were performed on microtubule pairs, not bundles of microtubules, and so it is unknown whether higher order effects may alter PRC1's ability as a brake against sliding forces. The observations in *C. elegans* could also be due to PRC1 having an important role in recruiting CLASP to the central spindle [100].

1.5.3 Chromosome Separation in Mammalian Central Spindles

In mammalian cells, the picture is far less clear with regards to anaphase B. In PTK cells, spindles experience plus-end growth and antiparallel sliding, generating microtubule flux as seen in metaphase spindles, but to a much lesser degree [122]. Laser ablation of central spindles in PTK cells, however, increased the rate of pole separation [114, 123], and EG5, the mammalian kinesin-5, which in *D. melanogaster* drove pole-pole separation, has been

reported to act as a brake against cortical pulling forces, demonstrating how sliding motors can be repurposed as brakes by the cell when an external force is applied [124, 125]. Conversely, in HeLa cells, EG5 has been reported as being detached from the spindle by PP2a phosphatase in late metaphase, prior to the onset of anaphase [126]. Despite PRC1-MT binding being inhibited by Cdk1 phosphorylation, work by Tolić et. al. has shown that in several mammalian cell lines, including PTK cells, PRC1 can be found bound to antiparallel overlaps called bridging fibres, which lie adjacent to kinetochore fibres in the metaphase spindle, and become incorporated in the central spindle in anaphase [127]. Laser ablation of one side of the bridging fibre, detaching it from the pole, reveals that during anaphase, there is antiparallel sliding in these overlaps, which contributes to chromosome separation. Antiparallel sliding was found not to be driven by either of the sliding motors which produce anaphase B in flies, and metaphase spindle bipolarity, EG5 and Hklp2 (a kinesin-12) [128]. Investigations into centralspindlin as the sliding motor proved inconclusive, even though centralspindlin depletion did result in a 28% reduction in kinetochore separation velocity. Evidence from *in vitro* experiments on microtubule pairs suggests centralspindlin is not an antiparallel sliding motor [87], and so centralspindlin's contribution to sliding velocity may lie in its role in maintaining the structural integrity of the central spindle, and hence better organization of the proteins responsible for the sliding force; proteins which remain unknown.

1.6 Constructing an Anaphase Central Spindle: Measuring the Overlap

So far we have seen where the anaphase central spindle comes from, how it controls its scale to orient itself in confinement, and how it resists destructive cellular forces, which try to drive the antiparallel overlaps apart. Though the separation of the antiparallel overlaps is clearly problematic for cytokinetic signalling, overgrowth of the overlaps is

also problematic, as proteins important for cytokinetic signalling become spread across the wider interpolar region, as opposed to concentrated in a clear narrow signalling band. Why do central spindle microtubules not keep growing into the opposite halves of the cell? The answer to this question lies with the kinesin-4 motor protein, KIF4a [129].

1.6.1 KIF4a Recruitment to the Central Spindle

KIF4a interacts with the N-terminal, homodimerisation domain of PRC1, with its C-terminal tail domain. In spite of this, KIF4a recruitment to the central spindle was delayed relative to PRC1. In metaphase, KIF4a is bound to chromosomes where it contributes to chromosome alignment, and may also limit the number and length of spindle microtubules [20]. Recent evidence suggests KIF4a's association with chromosomes is promoted by Aurora B phosphorylation (also at chromosomes during metaphase) [130]. As chromosomes are segregated during anaphase A, KIF4a likely becomes separated from Aurora B, which is transported to the central spindle overlap by MKLP2 [93]. This would theoretically result in KIF4a detaching from chromosomes, and diffusing back towards the centre of the cell where it is rephosphorylated. Work by Nunes Bastos et. al. has shown that Aurora B also enhances KIF4a's interaction with PRC1, and its accumulation in the overlap [131]. This might explain the delay seen between PRC1 and KIF4a accumulation, as well as explaining the longer overlaps initially seen in early anaphase [114]. This could conceivably be seen as another mechanism by which the central spindle avoids disassembly during anaphase B, by allowing overlaps to grow longer before pole separation begins. AMPK, a kinase involved in energy homeostasis, negatively regulates KIF4a at anaphase in a competitive manner with Aurora B, leading to longer overlaps. AMPK is involved in the glucose stress response, potentially linking this process with overlap length in the central spindle [132].

1.6.2 The End Caps Model

The exact mechanism by which PRC1 and KIF4a cooperate to control overlap length is somewhat controversial. Work by Zhu et. al., also working in HeLa cells, concluded that KIF4a was necessary to transport PRC1 to microtubule plus-ends during anaphase, in total contrast to what was seen by Kurasawa et. al. [133]. KIF4a has also been seen to form PRC1 end caps on parallel and single microtubules *in vivo* and *in vitro*, supporting the idea that KIF4a transports PRC1 to plus-ends [77, 79, 134, 135]. A truncated construct of mouse KIF4a lacking the PRC1 binding domain was able to focus overlaps in KIF4a depleted HeLa cells, suggesting that overlap focusing is not reliant on KIF4a transporting PRC1. It has been postulated that central spindle overlaps form from the crosslinking of these end tags [77] (Fig 1.8), however it is not clear how these ideas fit with the longer overlaps

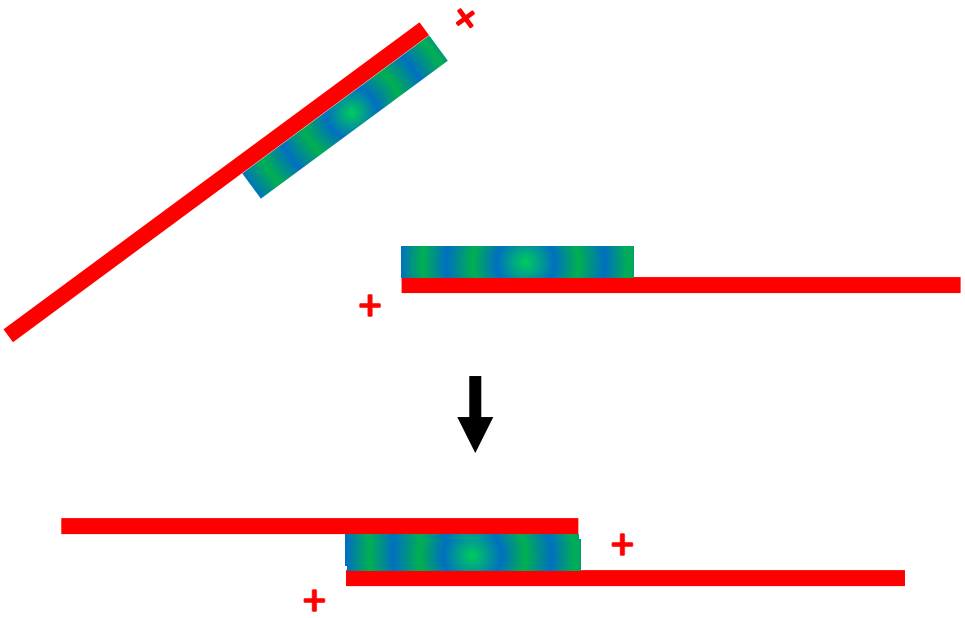

Figure 1.8: Schematic demonstrating the end caps model.
KIF4a transports PRC1 to microtubule plus-ends, forming steady state end-caps of PRC1 and KIF4a. These end caps can then fuse with one another. Microtubules (red) PRC1 (green) KIF4a (blue).

seen in early anaphase [114], or how it would act as a regulator of overlap length in what is a dynamic system.

1.6.3 The Steady State Overlap Model

In vitro experiments by Bieling et. al. on *X. laevis* PRC1 and KIF4a showed no evidence of PRC1/KIF4a end caps, and instead has shown that overlap length can be measured by the recruitment of KIF4a to overlaps by PRC1 [76]; the inverse of the end cap model, which relies on KIF4a transporting PRC1 [77] (Fig 1.9). They also did not report seeing end caps on single microtubules. The larger the antiparallel overlap, the more PRC1 is recruited. The more PRC1 is recruited, the more KIF4a is recruited. At a particular concentration of KIF4a, there will be an overlap length at which enough KIF4a is recruited at the microtubule plus-ends to stop the growth. Raising the KIF4a concentration in solution will mean shorter overlaps can accumulate enough KIF4a to stop the growth, and vice

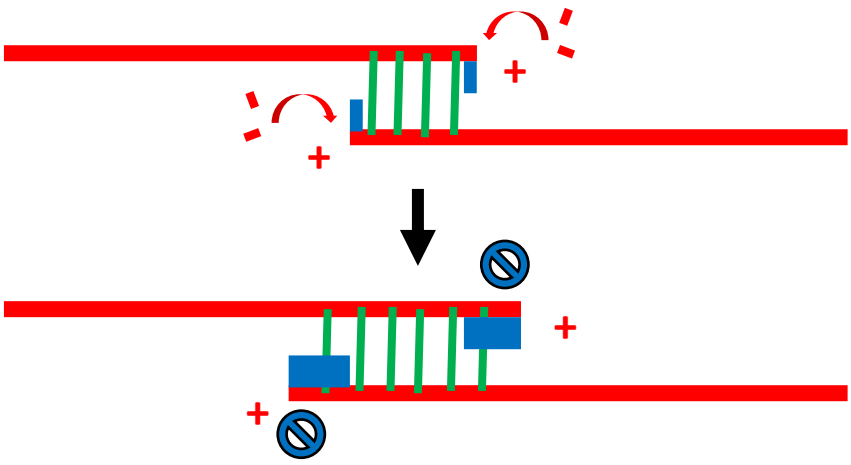

Figure 1.9: Schematic demonstrating the steady state overlap model
As overlaps grow, they recruit more PRC1, which in turn recruits more KIF4a to microtubule plus-ends. Eventually the overlap reaches a length that can sustain a large enough amount of KIF4a at the microtubule plus-ends, and the microtubules stop growing. Microtubules (red) PRC1 (green) KIF4a (blue).

versa. This has also been seen for the human proteins, though overlaps were twice as long as with the *Xenopus* homologues for a similar ratio of PRC1:KIF4a. Aurora B phosphorylation of human KIF4a brought overlaps back into line with what was seen with the *Xenopus* homologues [131]. Bieling et. al. also reported a small degree of sliding in the overlap, though these experiments were performed by attaching microtubule seeds to a cover slip, and so the effect of any sliding was to buckle the microtubules. The true effect of this sliding behaviour on overlap length, cannot be fully understood using this method, though the authors concluded it was a minor effect under their conditions. Experiments on late anaphase spindles suggests that there is still a degree of flux in the spindle driven by growth and sliding [122]. Static overlap lengths, therefore, could be due to an equilibrium steady state between growth and sliding, where sliding shrinks overlaps, which reduces the amount of KIF4a at plus-ends, allowing microtubules to grow. They could equally be due to the system continuously hitting up against some sort of barrier that prevents sliding below a certain length.

1.6.4 The Slide and Brake Model

KIF4a is clearly necessary for preventing the overgrowth of microtubules in the central spindle, but *in vivo,* overlaps appear longer at early anaphase, and become shorter until they stabilize at ~2 μm in late anaphase/telophase spindles [114]. How then are they prevented from becoming too short? This 2 μm length may simply be the length at which a molecular brake kicks in, be that from the centralspindlin/PRC1 interaction [42], or EG5 [124], or by compression of overlap retained PRC1, as seen for the yeast homologue, Ase1 [120] (Fig 1.10). Human PRC1 was not retained in antiparallel overlaps slid apart by EG5 [99], but in a tightly packed bundle of microtubules, this behaviour may change, leading to a build-up of PRC1 density, as overlaps shorten. Likewise the centralspindlin/PRC1

interaction may resist external cortical pulling forces, but that does not necessarily mean it can also resist internal sliding forces in the same way, as some molecules, such as EG5, can even drive both antiparallel sliding and braking [125].

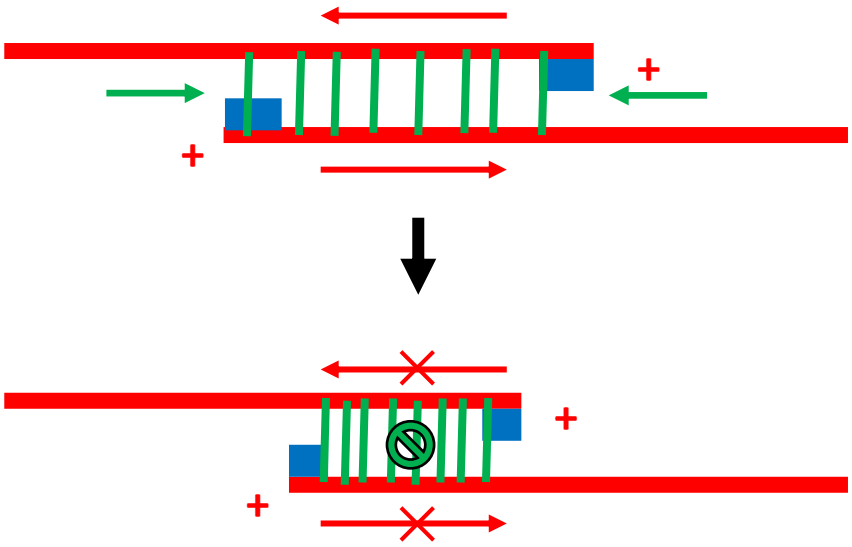

Figure 1.10: Schematic demonstrating the slide and brake model
PRC1 is retained in the overlap as it is slid apart. This results in an increase in PRC1 overlap density, and an increase in the frictional resistance force. At a certain overlap length, the frictional force is large enough to resist any further sliding. Microtubules (red) PRC1 (green) KIF4a (blue).

1.7 Summary and Aims

Central spindles have been visible for over a century, and yet we still have not got a firm understanding of how they are built and regulated. Literature on the topic can appear contradictory, and differences between model organisms and cell lines confuses matters further, while the potential for redundant pathways can mask functional roles of depleted proteins. This introduction has focused on proteins believed to be important for the structural integrity of the central spindle in cells, but they are only a handful of the proteins that actually accumulate there. In systems such as these, with highly complex

overlapping networks of proteins, *in vitro* reconstitution can be a highly useful tool in reverse engineering the underlying molecular mechanisms.

Previous *in vitro* studies in this area have focused on single microtubules, or microtubule pairs [76, 77, 131]. These microtubules are surface fixed, and nucleated from artificially stabilized seeds. In wild type central spindles, many individual microtubule overlaps are carefully aligned down the middle of the cell. Very little attention has been given to this phenomenon. Needless to say, it is unlikely we can truly understand the alignment of multiple antiparallel overlaps by studying single overlaps alone. This thesis, therefore, aims to go beyond previous work in this area by attempting to build a central spindle from bundles of dynamic microtubules, nucleated *de novo* in solution, and free to organize in the absence of chemical surface attachments or artificial confinements. In trying to achieve this goal, I hope to learn more about how the intrinsic properties of central spindle proteins can interact to form and regulate a central spindle, with the added aim of understanding how multiple antiparallel overlaps can align in a bundle.

For my *in vitro* reconstitution I will require the following: a microtubule crosslinking protein; a way of polarizing the system, so as to have MT minus-ends pointing out, and MT plus-ends pointing in; a way of preventing antiparallel overlaps growing too long; a way of preventing antiparallel overlaps becoming too short; and a protein capable of aligning multiple overlaps in a microtubule bundle. This may seem like a lot of proteins, but the literature suggests we may need only a handful, or even just two. PRC1 is our antiparallel microtubule cross-linker. KIF4a can prevent antiparallel overlaps growing too long. However, if the human KIF4a is capable of antiparallel sliding in the presence of PRC1, as was seen for the *Xenopus* homologue, then it may also act as a way of aligning

MT plus-ends in a bundle by accumulating at plus ends, and carrying those plus-ends to other plus-ends. This sliding behaviour would, in theory, also result in the polarization of the system, with minus ends being slid out, and plus-ends aligning in the centre. How will this sliding be prevented from destroying the overlap? Will human PRC1 act as a brake when in a bundle, or will centralspindlin be required in our system after all? There may be a third way. One could imagine a scenario where overgrown overlaps would lead to excessive amounts of KIF4a at microtubule plus-ends, which may then result in antiparallel sliding. As overlaps shrink, the amount of KIF4a at MT plus-ends would reduce, preventing further sliding, and stabilizing the overlap.

Over the following chapters I will address the following questions:

- What explains the apparent contradictions in the *in vitro* literature?
- Does human KIF4a slide antiparallel microtubules *in vitro*?
- What is the minimum required to build a basic central spindle architecture?
- How are many antiparallel overlaps aligned in a bundle?
- What mechanism determines the overlap length in the central spindle?

Chapter 2: PRC1 and KIF4a: Interactions with Each Other and Microtubules

The aim of this thesis is to reconstitute an anaphase central spindle from the minimal necessary components. Previous work in this area has focussed on single microtubules, or single pairs of microtubules. Though much can be gained from this approach, a real central spindle consists of bundles of many microtubule plus-ends, which have to be aligned along the line of the cleavage furrow. Microtubules can theoretically polymerise and depolymerise, without the system as a whole being destroyed; something which cannot be said for microtubule pairs. To try to understand these higher order properties of the central spindle, we will have to move to a higher order system, but before we do, it is important to first understand the lower order phenomena. In this chapter, therefore, we will attempt to understand and explain the differences between the works of Bieling et. al. [76] and Subramanian et. al. [77], establish the interactions between KIF4a, PRC1 and microtubules, and understand how these interactions affect the intrinsic functions of the proteins.

2.1 Purification of Fluorescently Labelled Proteins for use in Total Internal Reflection Fluorescence (TIRF) Microscopy

The majority of the data in this thesis have been collected using TIRF microscopy. TIRF microscopy is a technique which uses an angled laser to create an evanescent field, which is only able to penetrate ~200 nm into the sample solution (Fig 2.1) [136]. Only fluorescently labelled proteins near the coverslip are excited, which reduces the level of background fluorescence, and improves the signal to noise ratio. The TIRF microscope used primarily in this thesis was equipped with four lasers (405 nm, 561 nm, 488 nm and 640 nm), which

when combined with corresponding emissions filters, allowed me to visualise a maximum of 4 different fluorescently labelled proteins independently in a single experiment.

For TIRF experiments, I use coverslips, which I have passivated covalently with a mix of polyethylene glycol (PEG), and Biotin-PEG. Biotin-PEG is used for attaching GMPCPP stabilised biotin-labelled microtubule seeds to the coverslip surface. The surface and tubulin biotins are linked via neutravidin, creating a neutravidin sandwich (Fig 2.1).

The tubulin used in this thesis was purified from pig brain in collaboration with others. I

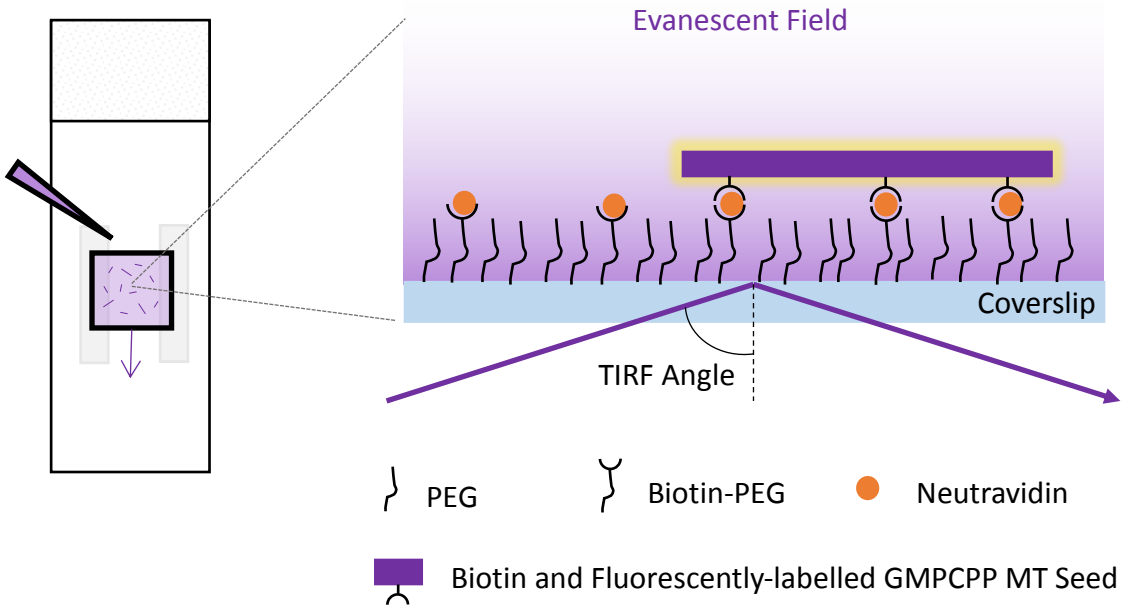

Figure 2.1: Schematic illustrating TIRF microscopy of surface-attached MT seed
(Left) Flow cell created by attaching a biotin functionalised coverslip to a PLL-PEG passivated slide using two strips of double sided tape. (Right) Illustration of the coverslip after MT seed attachment during a TIRF microscopy experiment. The fluorescently labelled MT seed is undergoing illumination by a laser angled to create an evanescent field.

used commercially bought Atto488, Alexa647 and biotin labels to label tubulin. The human KIF4a-mGFP, KIF4a-mBFP, PRC1-SNAP and mCherry-CAMSAP3ΔN used in this thesis were made recombinantly, using insect SF21 cells as the expression system. I purified the proteins from the insect cell pellets using affinity purification. KIF4a and

PRC1 constructs were His-tagged, and mCherry-CAMSAP3ΔN was Strep tagged. Purification tags were cleaved during the purification. Yields were typically 1-1.5 mg of protein purified from a 600 mL cell pellet. Purity was assessed by gel electrophoresis (Fig 2.2).

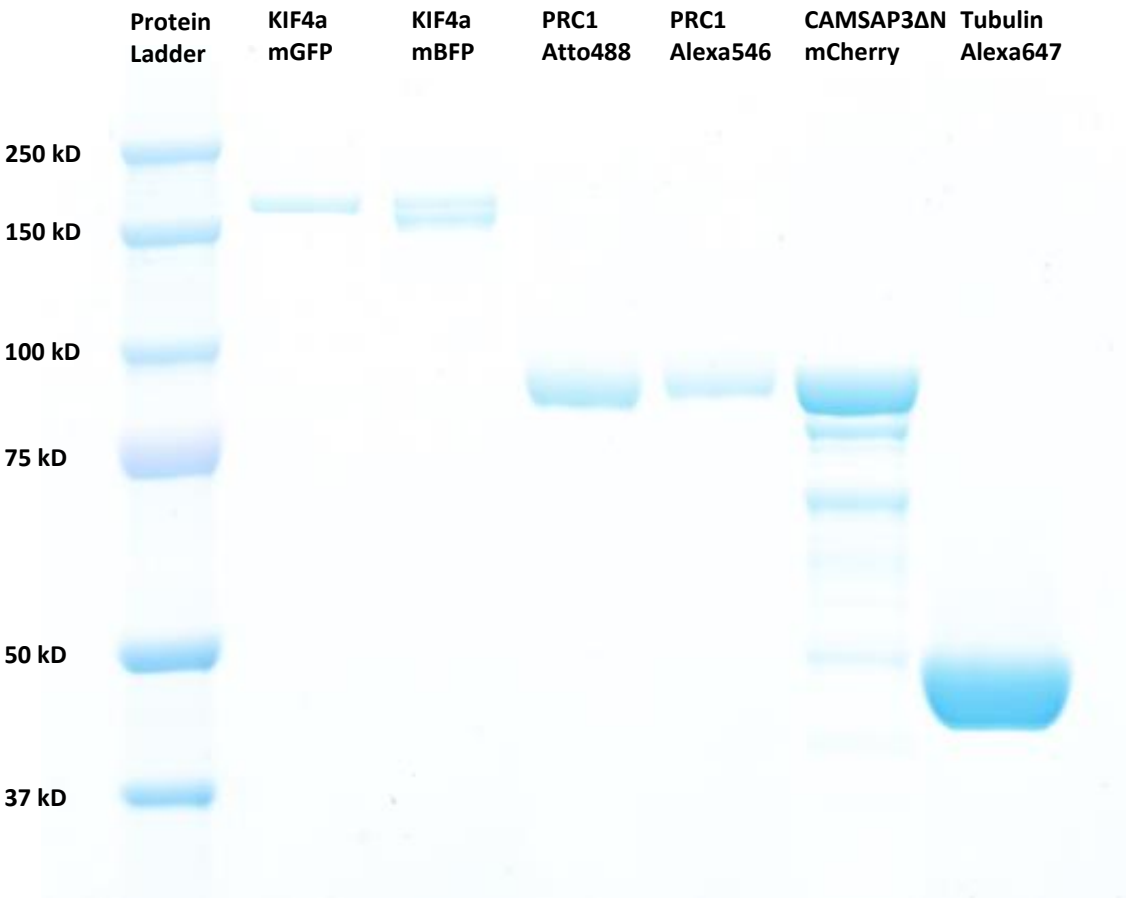

Figure 2.2: Coomassie gel of purified proteins
Coomassie gel of purified KIF4a-mGFP, KIF4a-mBFP, PRC1-Atto488, PRC1-Atto546, mCherry-CAMSAP3ΔN and Alexa647-tubulin. See materials and methods for purification protocols. Precision Plus Protein Dual Xtra Standard protein ladder was used (BioRad).

2.2 Higher Salt Concentrations Reduce the Size of KIF4a/PRC1 End Caps

This project began with two differing visions. On the one hand, the work of Bieling et. al., and on the other, the work of Subramanian et. al. The former, using the Xenopus proteins, and using TIRF microscopy to look at microtubule overlaps formed from two dynamic, surface-attached, microtubules growing towards one another, suggested Xl.PRC1 first accumulates in antiparallel overlaps, followed by recruitment of Xl.KIF4a. Neither were seen to bind single microtubules [76]. Subramanian et. al.'s work, using the human proteins, and using TIRF microscopy to look at non-dynamic, surface-attached, seeds, suggested both PRC1 and KIF4a alone bind single microtubules, and KIF4a transports PRC1 to plus-ends, forming end caps [77]. This thesis concerns itself only with the human proteins, as it aims to study the human central spindle. However, the differences between the two experiments were not confined to the protein's species. The salt concentration differed between the two cases, and this is expected to have a major effect on protein-protein interactions. The buffer used by Bieling et. al. was a high salt buffer (HSB) contained 85 mM of both potassium chloride and potassium acetate. The buffer used by Subramanian et. al. was a low salt buffer (LSB), which contained neither of these, nor an equivalent substitute. In LSB, using the same low protein concentrations as Subramanian et. al., I found that 0.25 nM of Atto488-Hs.PRC1 alone could bind to single stabilised microtubules, and that 1.5 nM mBFP-KIF4a alone appeared at MT plus-tips. When combined, KIF4a and PRC1 colocalised, and were able to form end caps, much larger than the plus-tip labelling seen in the case of KIF4a alone. This corresponds with what was found by Subramanian et. al. At the much higher protein concentrations

used by Bieling et. al., 5 nM Atto488-Hs.PRC1 and 100 nM KIF4a, the seeds were completely decorated with both KIF4a and PRC1 (Fig 2.3).

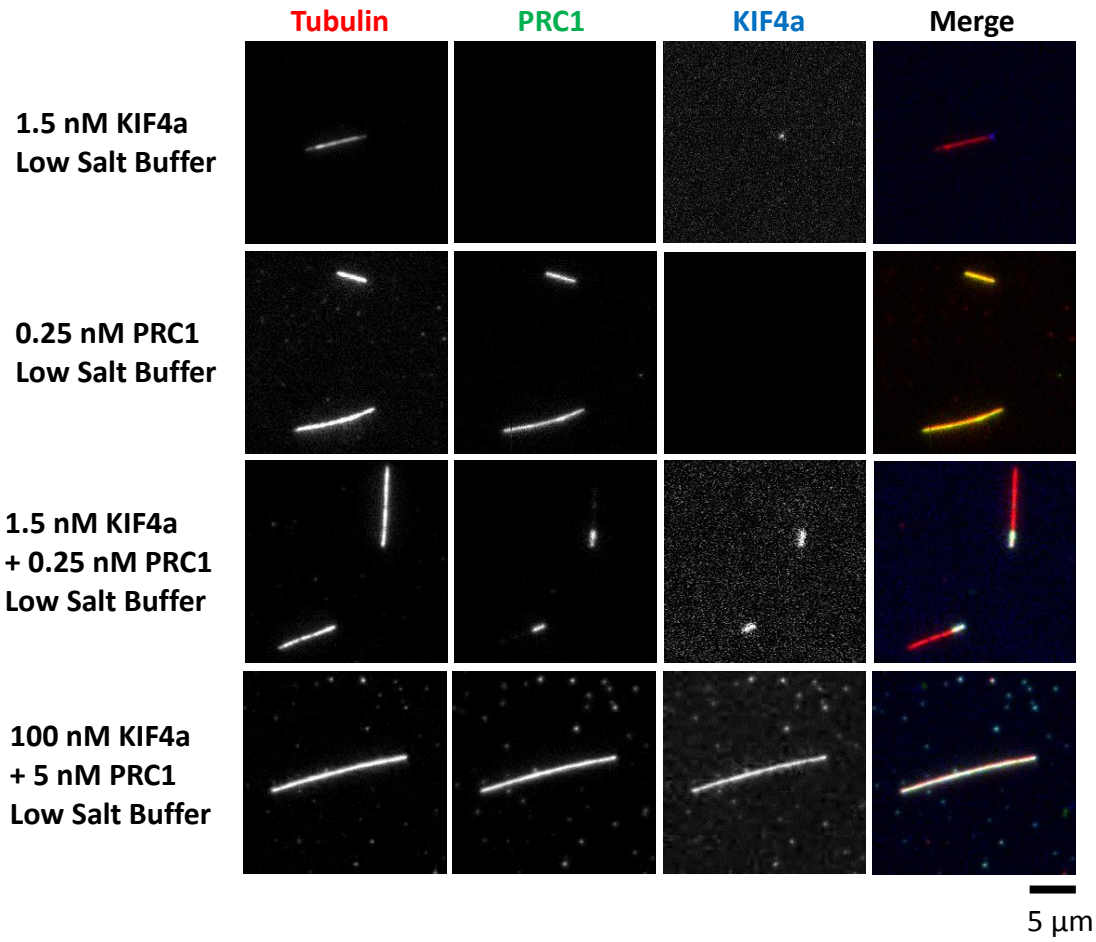

Figure 2.3: Behaviour of PRC1 and KIF4a in Low Salt Buffer
TIRF microscopy on stabilised GMPCPP MT seeds. Series demonstrates the formation of PRC1/KIF4a end tags in Low Salt Buffer, as reported by Subramanian et. al. It also shows how protein concentrations used by Bieling results in total seed decoration. Alexa647 Tubulin seed (red), Atto488-PRC1 (green), mBFP-KIF4a (blue). Data are representative, results have been successfully reproduced on separate days with different batches of protein.

I then wanted to test whether this was also the case for the human proteins in HSB (Fig 2.4). In this buffer, I saw no evidence of 5 nM Atto488-PRC1 alone binding to single MTs. Nor did I see 100 nM mBFP-KIF4a alone binding to single MTs. When KIF4a and PRC1 were added simultaneously, very small accumulations of PRC1 and KIF4a could be seen at MT plus-tips. This is in stark contrast to the fully decorated seeds in LSB at

these protein concentrations. The lack of binding in the absence of antiparallel overlaps chimes with what Bieling et. al. reported for the Xenopus proteins, however, they did not report an interaction with single MTs when KIF4a and PRC1 were combined, suggesting the human PRC1/KIF4a complex has a stronger affinity for microtubules.

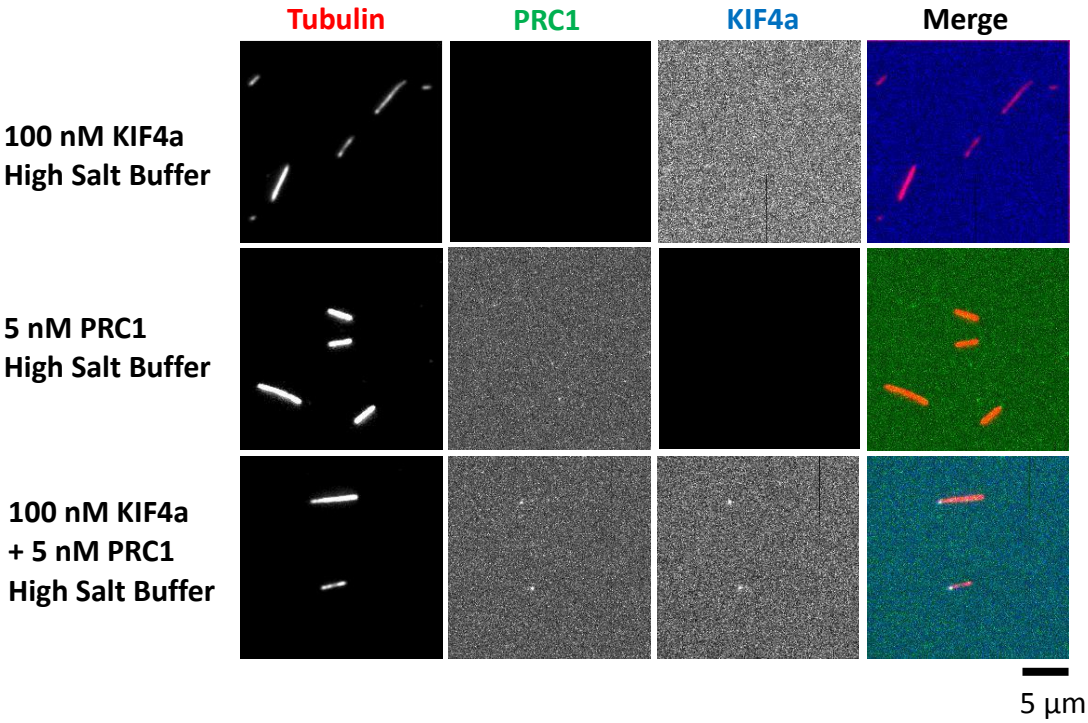

Figure 2.4: Behaviour of PRC1 and KIF4a in High Salt Buffer at high protein concentration
TIRF microscopy on stabilised GMPCPP MT seeds. Series demonstrates the absence of PRC1 and KIF4a binding alone on single MTs, but forming very small end tags in High Salt Buffer. Alexa647 Tubulin seed (red), Atto488-PRC1 (green), mBFP-KIF4a (blue). Data are representative, results have been successfully reproduced on separate days with different batches of protein.

The most important difference between the Bieling and Subramanian experiments, though, is arguably the salt concentration. In mid salt buffer (MSB) made by removing the potassium chloride from the HSB, but leaving the potassium acetate at 85 mM, the

Subramanian phenotype is restored, but at 5 nM Atto488-PRC1 and 100 nM mBFP-KIF4a (Fig 2.5).

2.3 PRC1/KIF4a Interaction Increases Affinity for Microtubules, and Decreases KIF4a Run Velocity

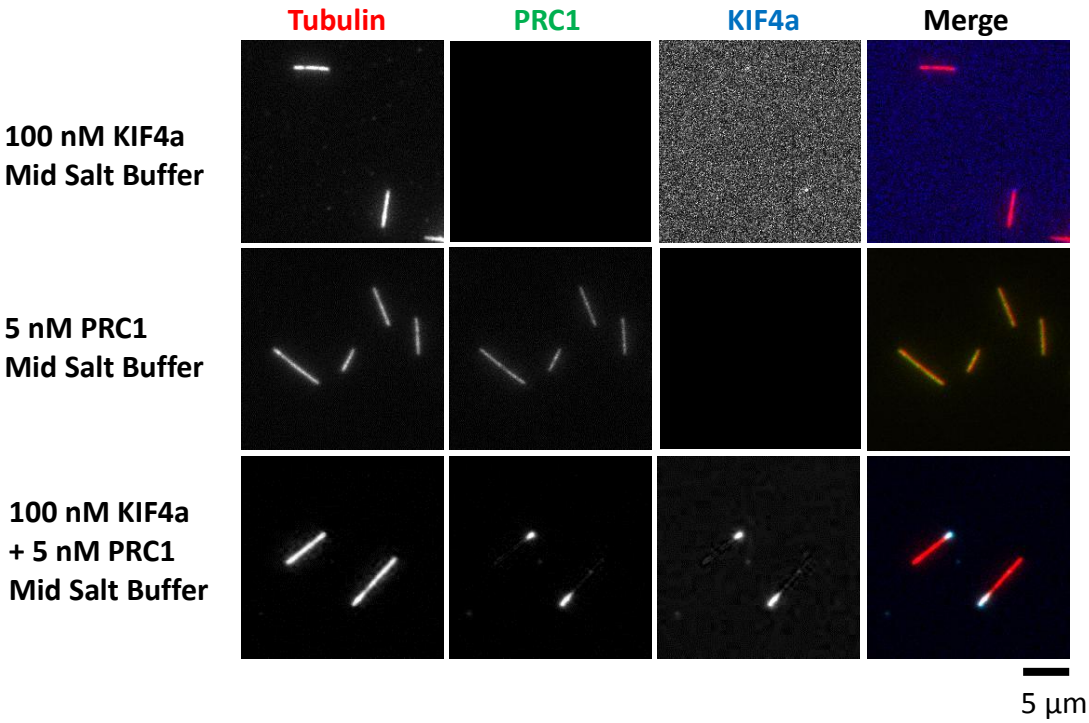

Figure 2.5: Behaviour of PRC1 and KIF4a in Mid Salt Buffer at high protein concentration
TIRF microscopy on stabilised GMPCPP MT seeds. Series demonstrates how removing KCl from HSB can restore PRC1/KIF4a end caps at high protein concentrations. Alexa647 Tubulin seed (red), Atto488-PRC1 (green), mBFP-KIF4a (blue). Data are representative, results have been successfully reproduced on separate days with different batches of protein.

The work on end caps suggested that the interaction between KIF4a and PRC1 strengthened their interaction with MTs. Both PRC1 and KIF4a can bind microtubules individually, but could a complex of the two bind MTs simultaneously? As discussed in chapter 1, KIF4a interacts, via its C terminal tail, to the N-terminal part of PRC1, which in the PRC1 homodimer is furthest away from PRC1's microtubule binding domain. One

might expect this would leave both KIF4a motor domains and PRC1 MT binding domains free to bind to microtubules. Kinesins have been shown to carry beads orders of magnitude their own size without drastically altering their run velocities. If KIF4a was

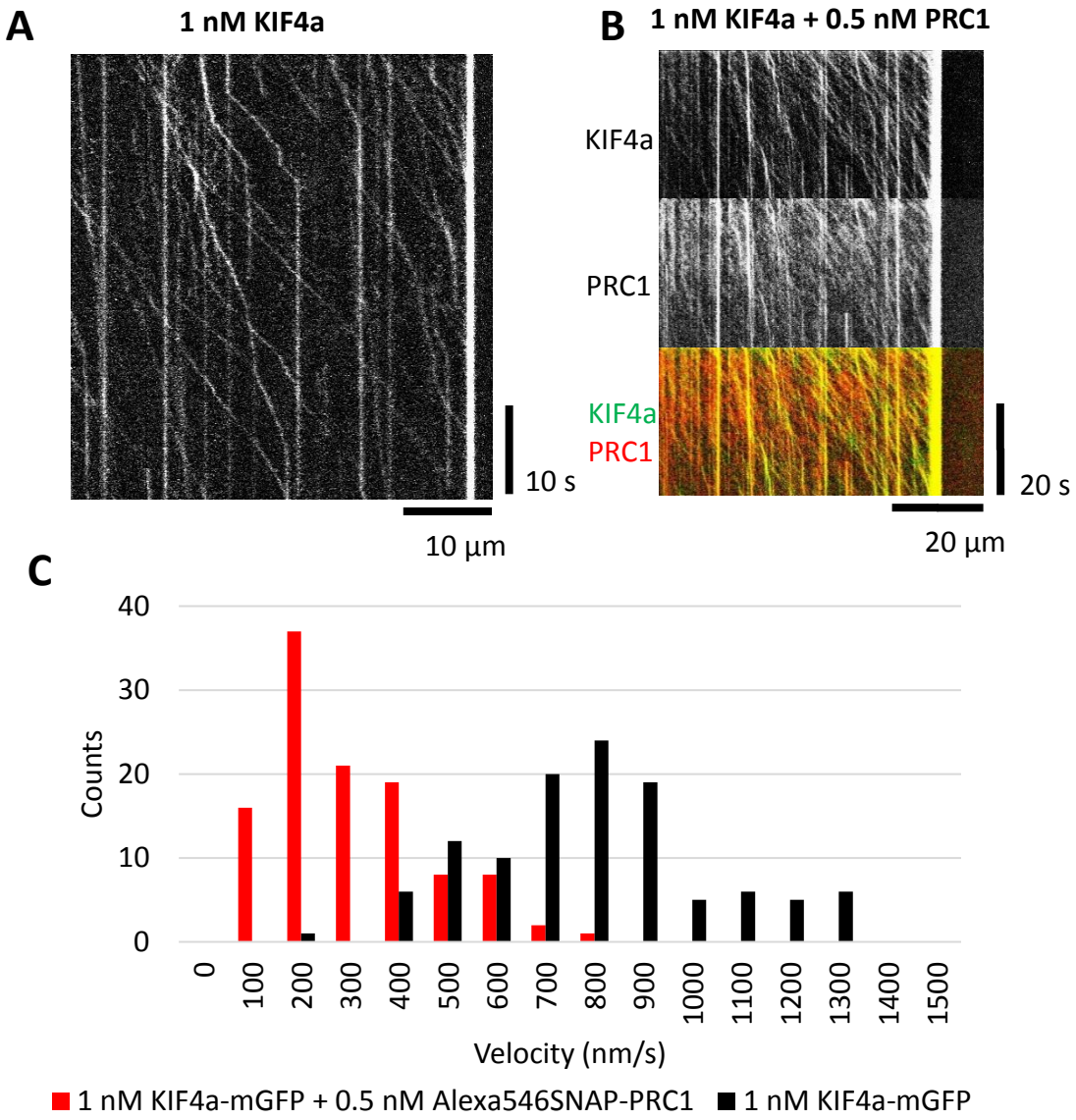

Figure 2.6: KIF4a-mGFP slowed down by PRC1-Alexa546 binding and transport in single molecule experiments
(A) Kymograph, taken from TIRF microscopy, demonstrating KIF4a processivity along stabilised microtubules in Low Salt Buffer (tubulin channel not shown). (B) Kymograph demonstrating KIF4a-mGFP transporting PRC1-Alexa546 along stabilised microtubules (tubulin channel not shown). (C) Histogram showing the reduction in KIF4a run velocity in the presence of PRC1; results for each condition are taken from 3 experiments performed with the same batch of protein on the same day.

simply transporting a passive PRC1, we would expect its run velocity to be unaffected. On the other hand, if PRC1 were able to interact with microtubules simultaneously, we would expect an increase in affinity for microtubules relative to KIF4a alone, but also a decrease in KIF4a run velocity, as it would be held back by the frictional force generated by the PRC1-MT interaction. I therefore conducted single molecule experiments on 1 nM mGFP-KIF4a alone, and with 0.5 nM Alexa546-PRC1, to measure any change in run velocity. Kymographs were used to assess run velocities. Kymographs are produced by measuring the pixels along a single line drawn on a timestack of images, and then stacking the 1D lines of pixels chronologically, one on top of the other, to create a 2D image with distance along what would be the x axis, and time increasing down the y axis (Fig 2.6A/B).

When measuring run velocity it was found that KIF4a alone had a run velocity of ~800 $nm.s^{-1}$ (Fig 2.6C); similar to that measured by Bieling et. al. for Xl.KIF4a [76]. Addition of PRC1 led to there being a noticeable increase in the number of KIF4a runs on microtubules (Fig 2.6B). When transporting PRC1, the run velocity of KIF4a was shown to decrease by a factor of 4 to ~200 $nm.s^{-1}$ (Fig 2.6C). The PRC1 is, we can assume, not just a passenger. It is clearly affecting KIF4a run velocity, most likely due to it interacting with microtubules simultaneously, causing a drag effect.

2.4 Hs.KIF4a Can Turn Off MT Dynamics in MSB but Not HSB

To understand the differences between the Xenopus and human proteins, how they interact, and how they control overlap lengths, I performed Bieling's microtubule overlap experiments in HSB as reported [76], but with the human proteins. I found that antiparallel

overlaps form, recruit Alexa546-PRC1 (5 nM) and mBFP-KIF4a (100 nM), but don't stop growing as was seen for Xl.PRC1 and Xl.KIF4a (Fig 2.7A). Having said that, microtubule

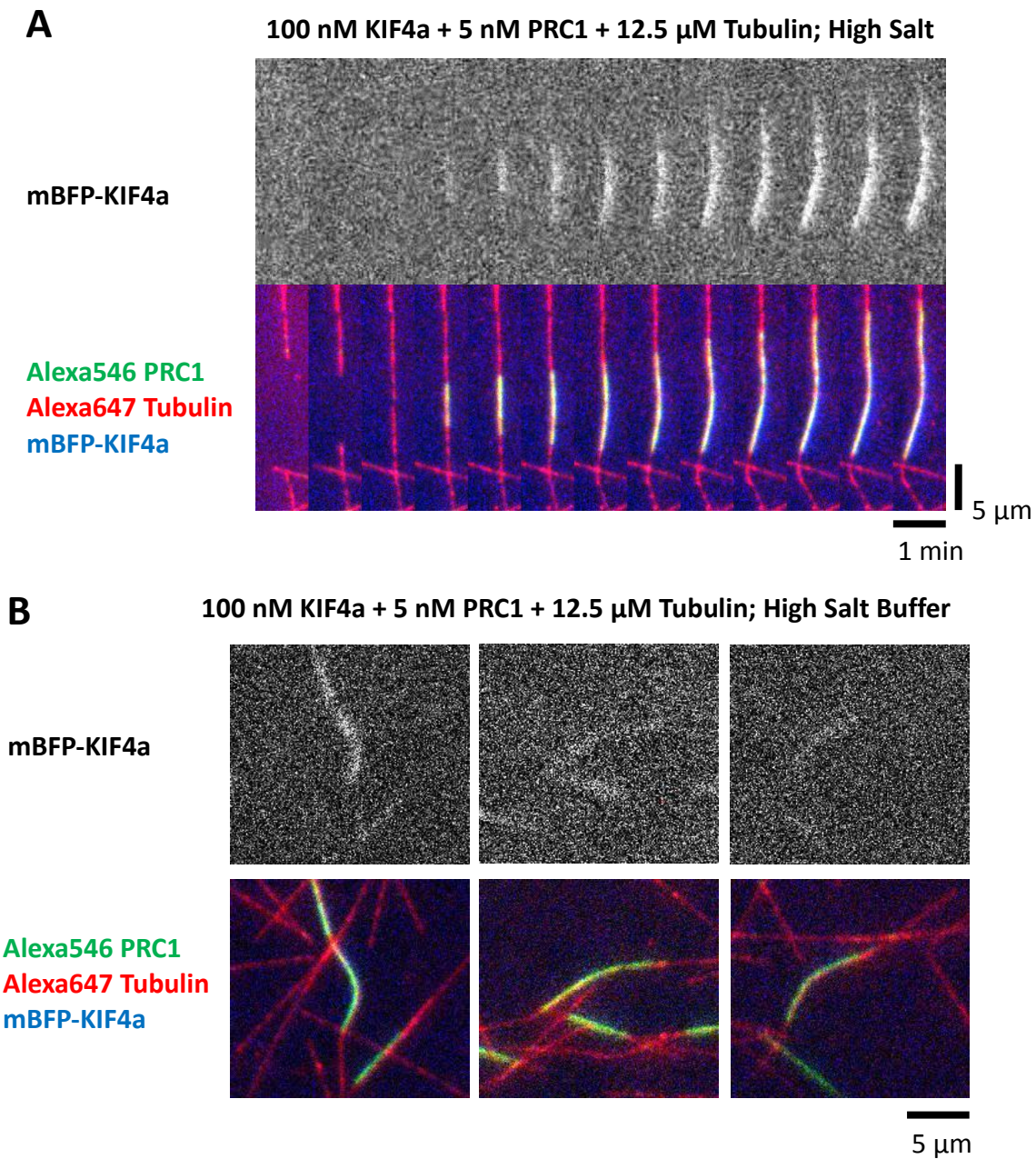

Figure 2.7: Examples of MT buckling in antiparallel overlaps
TIRF microscopy of microtubules grown from GMPCPP seeds (A) Timelapse of overlapping MTs grown from surface attached GMPCPP seeds in HSB. KIF4a and PRC1 accumulate in the overlap, slowing MT growth, and encouraging buckling. (B) Still images taken at t =12.5 min of overlapping MTs grown from surface attached GMPCPP seeds in HSB. KIF4a and PRC1 accumulate in the overlap, and KIF4a sliding causes the microtubules to buckle. Data are representative, results were successfully reproduced in 7 experiments across two separate days with different batches of protein.

growth did slow in the overlaps. In the example in (Fig. 2.7A), the MTs initially grow at an average of ~44 nm.s^{-1}, whilst in the overlap, they grow at ~11 nm.s^{-1}, so a 4 fold decrease in MT growth rate.

What was also clear was the presence of MT buckling in the overlaps. The MTs in these experiments are growing out from surface attached seeds, so if there is any antiparallel sliding being generated in the overlaps by KIF4a, the MTs will not be capable of sliding apart, as their minus-ends are fixed, and so buckling will ensue (Fig 2.7B). Buckling was reported for the Xenopus proteins as well, though this was not seen as a major factor in setting the overlap length, which was the main focus of the study. With the human proteins, however, this effect seems more prominent. This is possibly because overlaps are bigger, and so the buckling simply appears more pronounced, or there is a braking force, which prevents significant sliding, which is stronger in the Xenopus case.

The Bieling model of antiparallel overlap length control rests on the ability of Xl.KIF4a to stop MT growth all together to give a stable overlap length. To test whether KIF4a can stop microtubule growth on individual microtubules, it was necessary to move to MSB, as Bieling himself did, as KIF4a or Xl.KIF4a alone do not bind single MTs in HSB (see Fig 2.3). I performed experiments looking at 30 nM mBFP-KIF4a on single microtubules grown from GMPCPP stabilised seeds. Averaging over multiple plus-tips showed KIF4a accumulating at the very tip of the MT, as opposed to slightly behind it like the EB plus-end tracking proteins (Fig 2.8B). KIF4a had a clear negative effect on the MT growth rate (Fig 2.8A). KIF4a was capable of decreasing growth rate by a factor of 10, or stopping it entirely (Fig 2.8C).

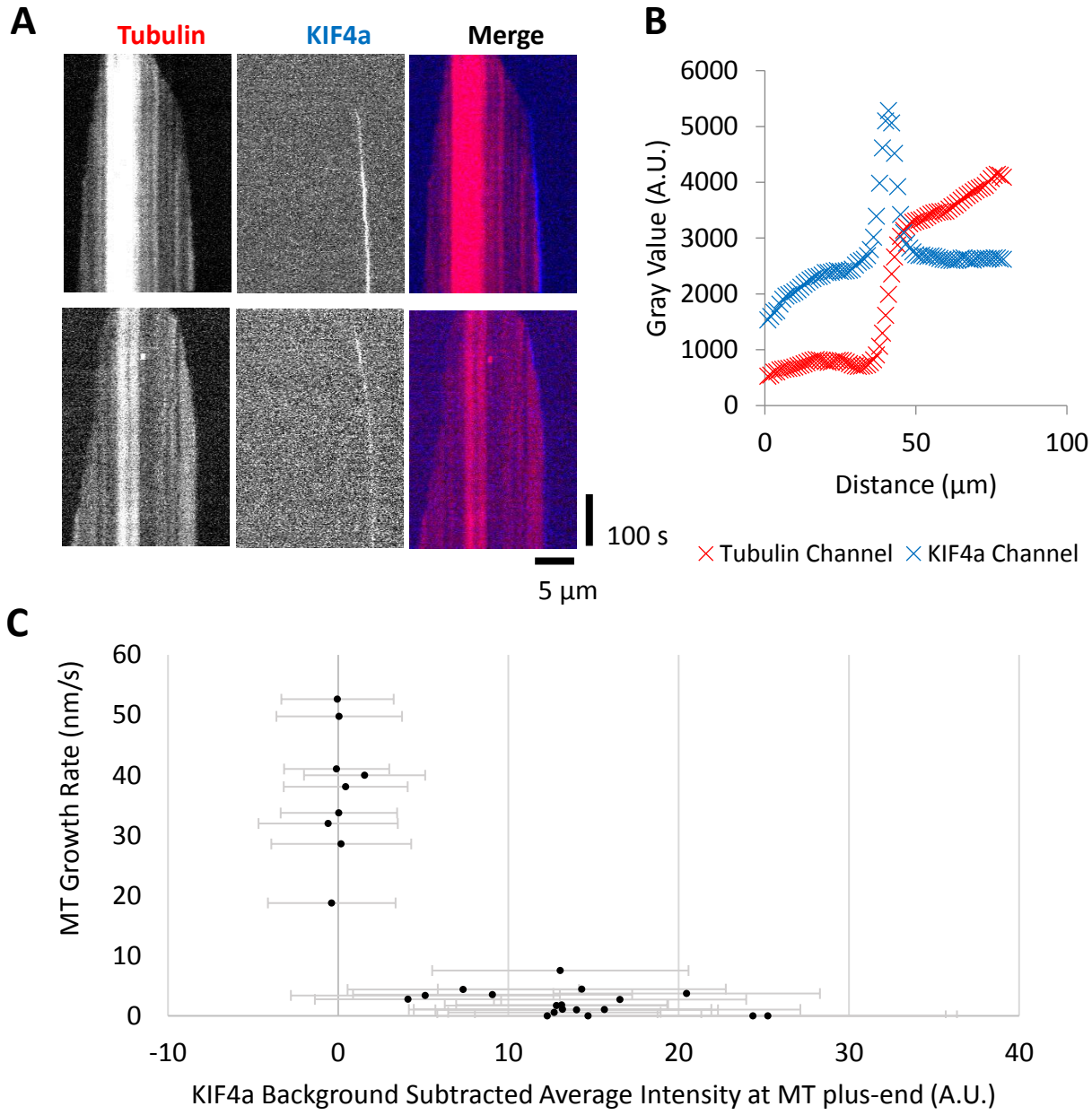

Figure 2.8: KIF4a suppresses MT dynamics in MSB
(A) MTs grown from GMPCPP stabilised seeds in the presence of free tubulin: Alexa647-Tubulin 12.5 µM, mGFP-KIF4a 30 nM. Kymograph demonstrating KIF4a suppressing MT dynamics in Mid Salt Buffer. (B) Graph uses an average over several MT plus tips to show KIF4a is positioned at the very end of the MT. (C) Graph showing the significant reduction of MT growth rate in the presence of KIF4a. Results were taken from 4 experiments performed on the same day with the same batch of proteins.

2.5 Discussion

In this chapter, I have shown how the salt concentration can affect the interactions of human PRC1 and KIF4a with microtubules. At high salt concentrations, there was no apparent binding of PRC1 and KIF4a to microtubules alone, whereas at low salt concentrations they do. Increasing the salt concentration can decrease the length of KIF4a/PRC1 end caps, which form on stabilised microtubule seeds. Salt concentration was also shown to affect KIF4a's ability to suppress microtubule dynamics. At high salt concentrations, KIF4a slowed, but could not stop microtubule polymerisation, whereas at lower salt concentrations it could. The inability of human KIF4a/PRC1 to stop growth at high salt concentration was also seen by Nunes Bastos et. al. They were able to correct this by AuroraB phosphorylation of KIF4a [131].

Though salt concentration has a major effect on PRC1/KIF4a behaviour, it can only partly account for the different behaviours reported in the literature for the Xenopus and human proteins. Unlike the Xenopus proteins, human PRC1 and KIF4a, when combined, could bind to single microtubules. In spite of this apparent higher affinity of the complex, human KIF4a could not prevent microtubule growth under the same conditions in which the Xenopus Xl.KIF4a could. The homology between Hs.PRC1 and Xl.PRC1 amino acid sequences is 63.0%. The major microtubule contacts, based on the work of Kellogg et. al., are conserved between the two species [98]. The homology between KIF4a and Xl.KIF4a amino acid sequences is 68.3%. The motor domain is more highly conserved, however, and the C terminal tail far less conserved. Differences between the Xenopus and human proteins may be due to the interactions between KIF4a, PRC1, and microtubules or differences in the structural mechanics of the proteins themselves.

Here, I have shown how a combination of salt and species can explain the different observations seen in the literature, and help incorporate previous findings into my own model of overlap length control and alignment, as it develops over the following chapters. The high salt conditions, HSB, prevent the formation of clear end caps on single microtubules, which have been seen *in vivo*, suggesting this condition may not be as physiologically relevant, despite the order of recruitment (PRC1 recruiting KIF4a) being supported by cellular studies. At low salt conditions, LSB, when protein concentrations were raised, aggregates began to appear (data not shown). To explore the parametric boundaries of my *in vitro* reconstitution, I intend to use an array of protein concentrations, and so I need a buffer in which I am confident proteins will remain soluble, and aggregation will not create artefacts in the results at higher concentrations. From now on, therefore, I will opt to use a salt condition in between the HSB and LSB conditions. Experiments in the following chapters will be performed in MSB, as proteins remained soluble across a wide range of concentrations, whilst maintaining all their apparent functionality.

Chapter 3: Self Organisation of Microtubule Bundles by KIF4a and PRC1

The previous chapter focussed primarily on single microtubules, or pairs of microtubules. Central spindles, however, are composed of many bundled microtubules. Studying microtubule bundles *in vitro* is challenging, because when you add a MT bundler you tend to get expansive 3D bundled networks of microtubules that spread out through the bulk solution. Though these are interesting systems in their own right [137], they are poor representations of a central spindle, which has an ordered axial symmetry and polarity. One potential solution is to use confinement to isolate single bundles, but the shape, size and chemical nature of any confinement is as much an additional component to a system as adding another protein, and examples can be found in the literature where central spindles form in the absence of any obvious confinement, suggesting it should be an unnecessary addition. The ability of KIF4a to suppress plus-end dynamics, however, may help to prevent the formation of bundled networks, and allow me to study the organisation of individual isolated bundles of microtubules.

3.1 Solution Nucleated MTs Are Organised Around MT Seeds in the Presence of KIF4a and PRC1 in Mid Salt Buffer

To try and look at isolated microtubule bundles organised by PRC1-Alexa546 (2.5 nM) and KIF4a (6 nM), I first attached microtubule seeds to surfaces, and added free tubulin (17.5 μM) to nucleate microtubules in solution, which could then land on the seeds. Immobilised seeds were used to bring the self-organised system into the TIRF field, and by fixing the bundle along a single line, the seed would also allow me to produce kymographs of the data, which makes it easier to visualise spatial changes, such as overlap length changes over time.

When I performed these experiments, solution nucleated microtubules did form antiparallel overlaps with seeds, though unlike what was seen in the High Salt Buffer

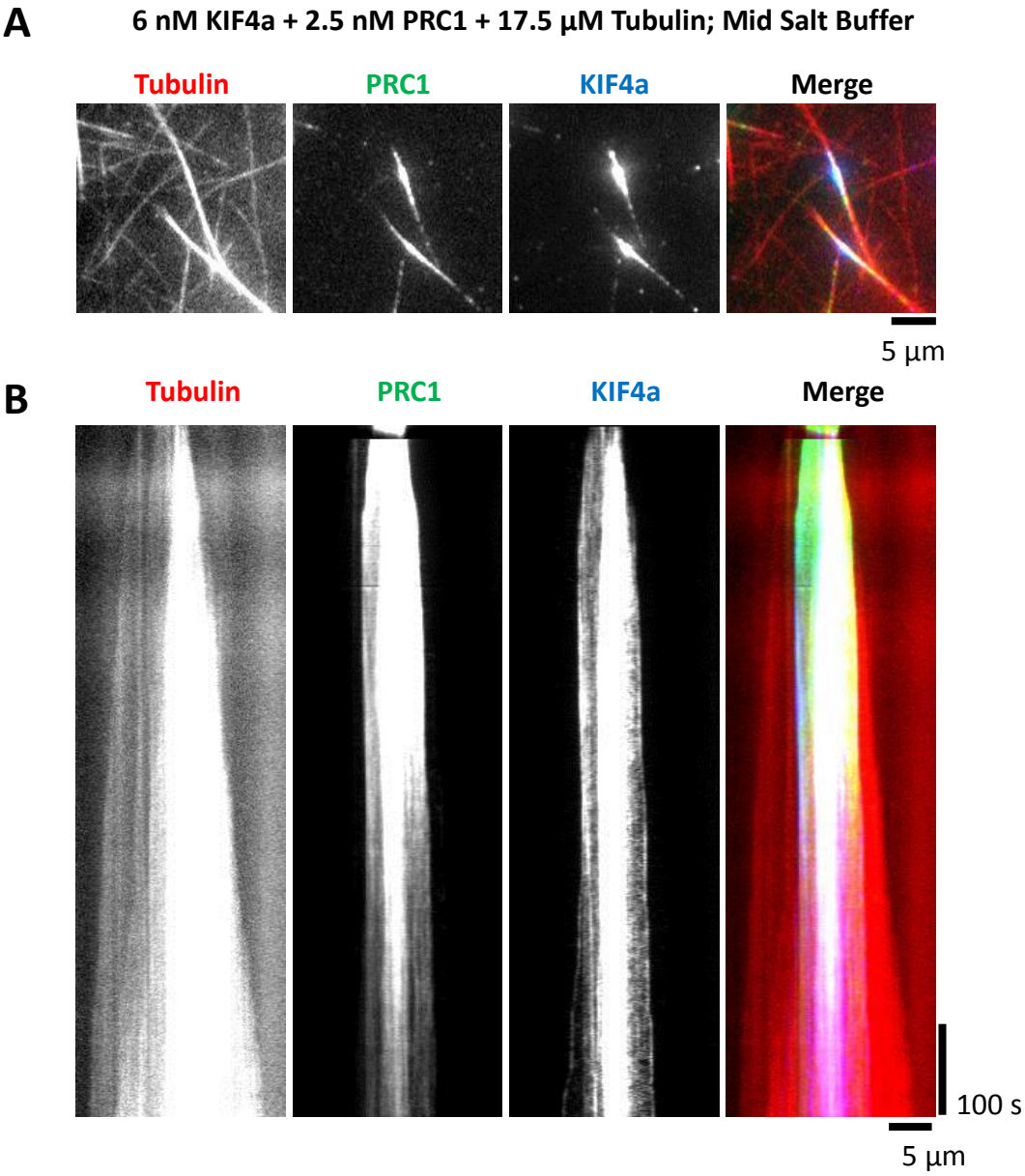

Figure 3.1: Solution-nucleated MTs self-organise overlaps around surface fixed GMPCPP seeds.
TIRF microscopy of MTs grown from GMPCPP stabilised seeds. 6 nM mGFP-KIF4a + 2.5 nM PRC1-Alexa546 + 17.5 µM Alexa647 Tubulin; Mid Salt Buffer (A) Still image taken at t = 12.5 min show typical structure of self-organised structure. (B) Kymograph demonstrating the behaviour over time. Data are representative, results were reproduced once for this protein concentration on the same day with the same batches of protein, but similar qualitative results were seen for similar protein concentrations across different days with the same batch of protein (Data not shown).

(Fig2.6) these overlaps did not grow continuously. There seemed to be an initial growth, followed by what seemed like focussing of the overlap zone, or at least of the PRC1 and KIF4a signals (Fig 3.1). Microtubules clearly grew out from either side of the overlap, but this growth was slow, characteristic of minus-end growth, as opposed to plus-end growth, and no KIF4a was detectable at these ends. It was also unclear where exactly the seed was, relative to the focussed KIF4a and PRC1 signals, because of solution-nucleated microtubules masking it.

To try to understand what I was seeing, I decided to use two differently labelled tubulins. I used Alexa647 labelled tubulin for the seed, and flowed in free Atto488 tubulin (12.5 μM). The SNAP tagged PRC1 (2.5 nM) was labelled with Alexa546, and the KIF4a (6 nM) was mBFP labelled. This allowed me to do 4-colour TIRF microscopy. When I repeated the experiments, reducing the tubulin concentration, so as to have less microtubule masking, it was clear that MTs nucleating in solution were being organised into antiparallel overlaps around what is assumed to be the plus-end of the MT seed, based on the known directionality of KIF4a. In all data presented in this report, KIf4a is represented as blue, PRC1 green and tubulin red. I have altered these colour representations for Fig 3.2, to highlight the difference between minus end growth of the seed, and overlapping microtubules from solution. It can be seen in Fig 3.2 that the seed has remained mostly bare. One end is free of any PRC1 or KIF4a, and free tubulin can be seen adding to this end without any overlap of the green and red signal. This is minus-end growth. At the other end, however, there is a yellow overlapping section, where small, solution-nucleated, green microtubules overlap with the red seed. If we overlay the PRC1 (blue) over this, we see that the PRC1 localises at this overlap.

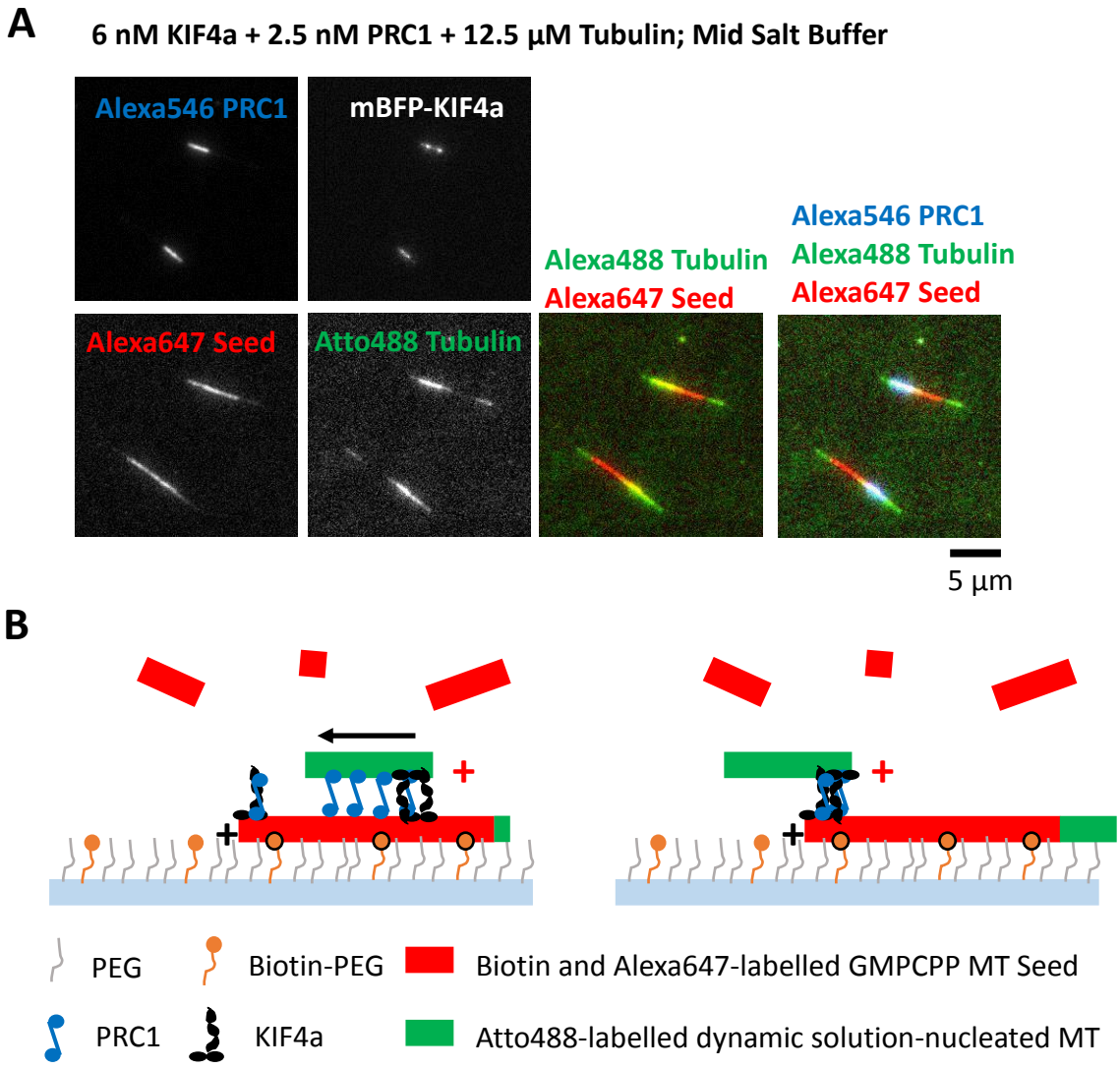

Figure 3.2: 4 colour TIRF microscopy of solution-nucleated MTs self-organising around surface fixed GMPCPP seeds.
TIRF microscopy of MTs grown from GMPCPP stabilised seeds. 6 nM mBFP-KIF4a + 2.5 nM Alexa546SNAP-PRC1 + 12.5 µM Atto488-Tubulin; Mid Salt Buffer (A) In Mid Salt Buffer, MTs nucleate in solution, and are organised by KIF4a and PRC1 around a surface bound GMPCPP MT seed to create stable overlaps. Data are representative, results were successfully reproduced 4 times over two days with the same protein batches, and similar qualitative results were seen for similar protein concentrations across different days with the same protein batches (Data not shown). (B) Schematic to illustrate the 4 colour microscopy experiment.

When we make kymographs of these we can clearly see small microtubules landing on the seed and being slid unidirectionally along the seed to form fixed overlaps at the end already containing KIF4a and PRC1 (Fig 3.3). KIF4a and PRC1 decorate the sliding microtubules, but KIF4a is distributed more heavily towards the MT plus-end. The overlaps are not slid apart in these experiments. Something causes the sliding to stop, giving fixed overlaps.

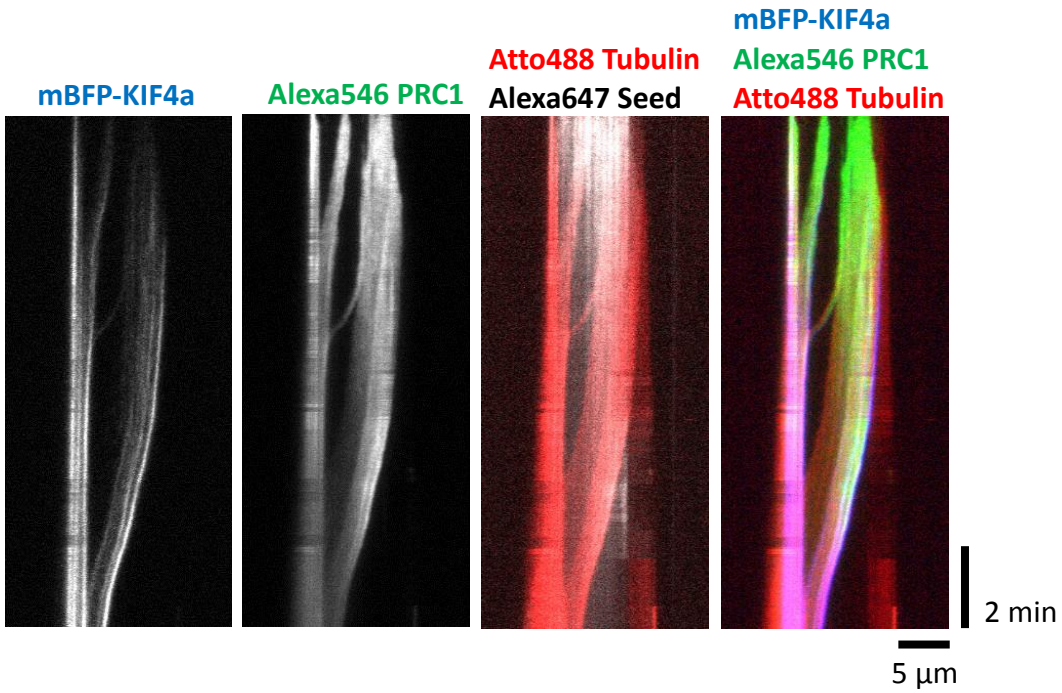

Figure 3.3: Solution-nucleated MTs land antiparallel on GMPCPP seeds, and are transported to plus ends by KIF4a and PRC1
TIRF microscopy of MTs grown from GMPCPP stabilised seeds. 6 nM mBFP-KIF4a + 2.5 nM Alexa546SNAP-PRC1 + 12.5 µM Tubulin; Mid Salt Buffer. Kymograph clearly demonstrating sliding of a MT, which has landed on the stabilised seed.

The ability of KIF4a to align multiple plus-ends by antiparallel sliding may answer more questions than that of overlap length control. It may also act as a way of aligning multiple overlaps when dealing with more than two microtubules, and keeping the central spindle aligned in cells undergoing dynamic changes, such as furrow ingression. Some

microtubules which nucleated in solution did not land on seeds, but they did appear on the coverslip, and diffused in two dimensions. This is most likely due to an entropic effect, aided by the presence of 0.15% methyl cellulose in the buffer. One microtubule can displace many methyl cellulose molecules ordered at the PEG surface, increasing the overall entropy of the system. The longer the microtubule, or the larger the bundle of microtubules, the larger the entropic gain. Once on the surface, bundles are within the reach of the TIRF field, meaning we can study them using TIRF microscopy with all its advantages. Once it was established that KIF4a and PRC1 could organise microtubule bundles to some degree, and that microtubules remained in the TIRF field without the need for surface immobilisation, it became tempting to think that the seed could be removed. Would PRC1 and KIF4a be able to organise free floating microtubules? Would the plus-ends of those microtubules be aligned? Would they alone be able to recreate a basic central spindle architecture?

3.2 Removing the Seed

When I performed experiments in MSB with KIF4a-mBFP (50 nM), PRC1-Atto488 (10 nM) and free Alexa647-tubulin (12.5 μM), in the absence of any surface-attached seed, they resulted in the formation of individual bundles, organised so as to have a narrow band of antiparallel overlaps in the middle, with minus ends emanating out from either side (Fig 3.4). This mirrors the fundamental organisation at the heart of the anaphase central spindle, and these will be referred to as anaphase mini spindles. It is important to stress that the microtubules in these experiments are nucleated de novo, are not surface attached, and are dynamic.

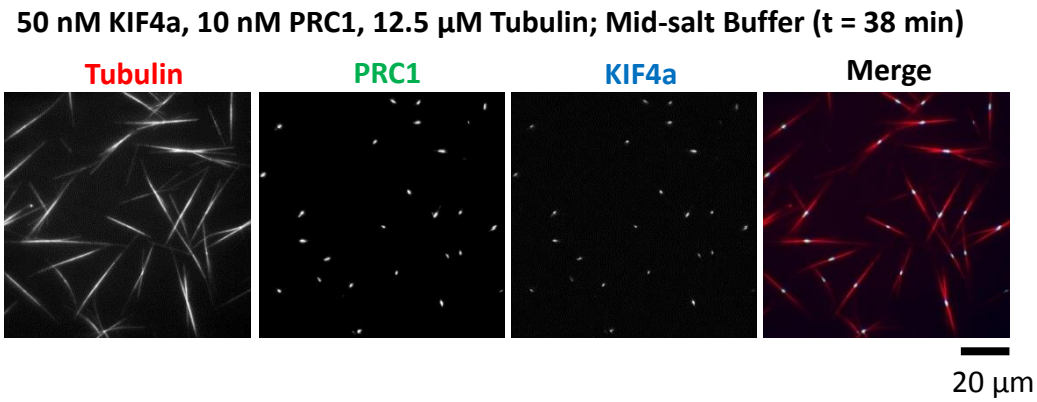

Figure 3.4: Characteristic end point of the KIF4a/PRC1 Self-Organisation Assay
Still image taken at t =38 min. TIRF microscopy of MTs grown de novo in solution and organised into aligned antiparallel overlaps by KIF4a and PRC1. Alexa647-Tubulin, PRC1-Atto488 and KIF4a-mBFP. Data are representative, qualitative results have been reproduced extensively over multiple days and with different batches of protein.

The progress of these experiments occurred with a reproducible pattern (Fig 3.5). Initially, little could be seen on the coverslip in TIRF microscopy. Then, within a matter of minutes, small microtubule bundles, less than 1 µm in size, began to nucleate in solution, and appear on the surface where they diffused randomly in two dimensions, sometimes disappearing and returning to the bulk solution. The microtubules in these small bundles began to grow, and the bundles themselves fused with other small bundles they came into contact with, either on the surface, or from other bundles/microtubules landing from solution. This resulted in a bundle growth phase where the tubulin, PRC1 and KIF4a signals appeared to co-localise. As the bundles grew, they diffused less, and began to settle on the coverslip. The KIF4a and PRC1 signals began to narrow into a central area within the bundle, as antiparallel sliding began to shrink the overlapping zone, and align the microtubule plus-ends. At some point, sliding stopped, and the overlap length appeared to stabilise. These spindles remained stable even after 1.5 hours. Now I had an assay that worked to organise microtubule bundles into a central-spindle-like architecture,

but it was unclear how robust the system was to changes in protein concentrations? Could protein concentrations be too high or too low?

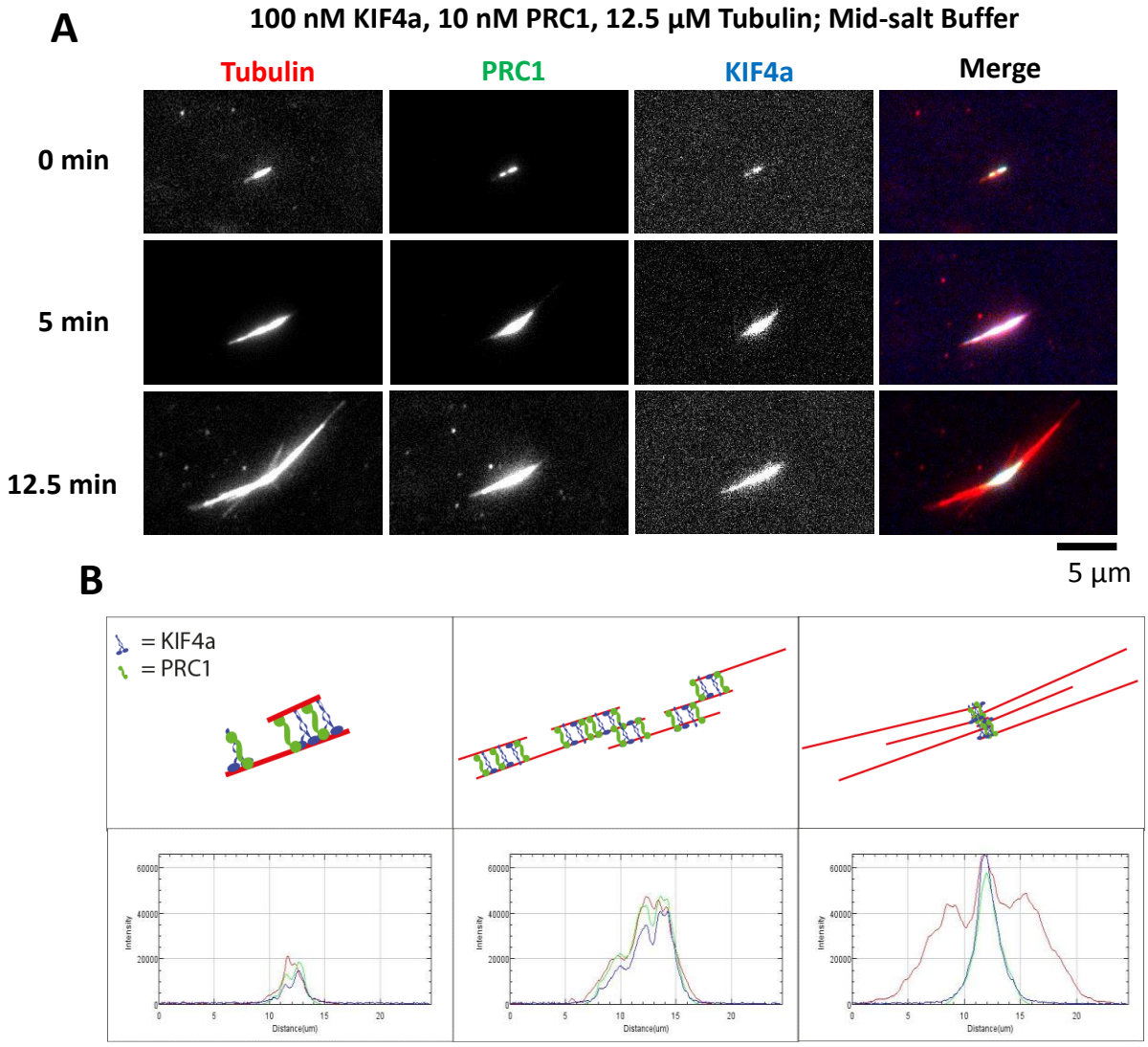

Figure 3.5: De novo, dynamic MTs self-organise into polar spindles in presence of PRC1 and KIF4a
TIRF microscopy of MTs grown de novo in solution. (A) Time course of a spindle, consisting of an initial bundle growth phase, followed by organisation of overlaps by KIF4a and PRC1. (B) Schematic of (A), as well as fluorescence intensity plots showing the development of a spindle. Intensities have been scaled separately for each channel to fit on a single plot, and are therefore not directly comparable.

3.3 Reducing KIF4a Concentration Prevents Sliding

I first began by keeping the PRC1 concentration at 5 nM, whilst reducing the KIF4a concentration from 5-1 nM (Fig 3.6). If KIF4a is responsible for sliding the microtubules, and reducing the growth rate of plus-ends, then reducing the concentration should eventually prevent the sliding, or increase the microtubule growth rate, or both. At 5 nM PRC1, and 5 nM KIF4a, the system was still able to organise itself into spindles. When I reduced the KIF4a concentration to 2 nM, however, the sliding was prevented. However,

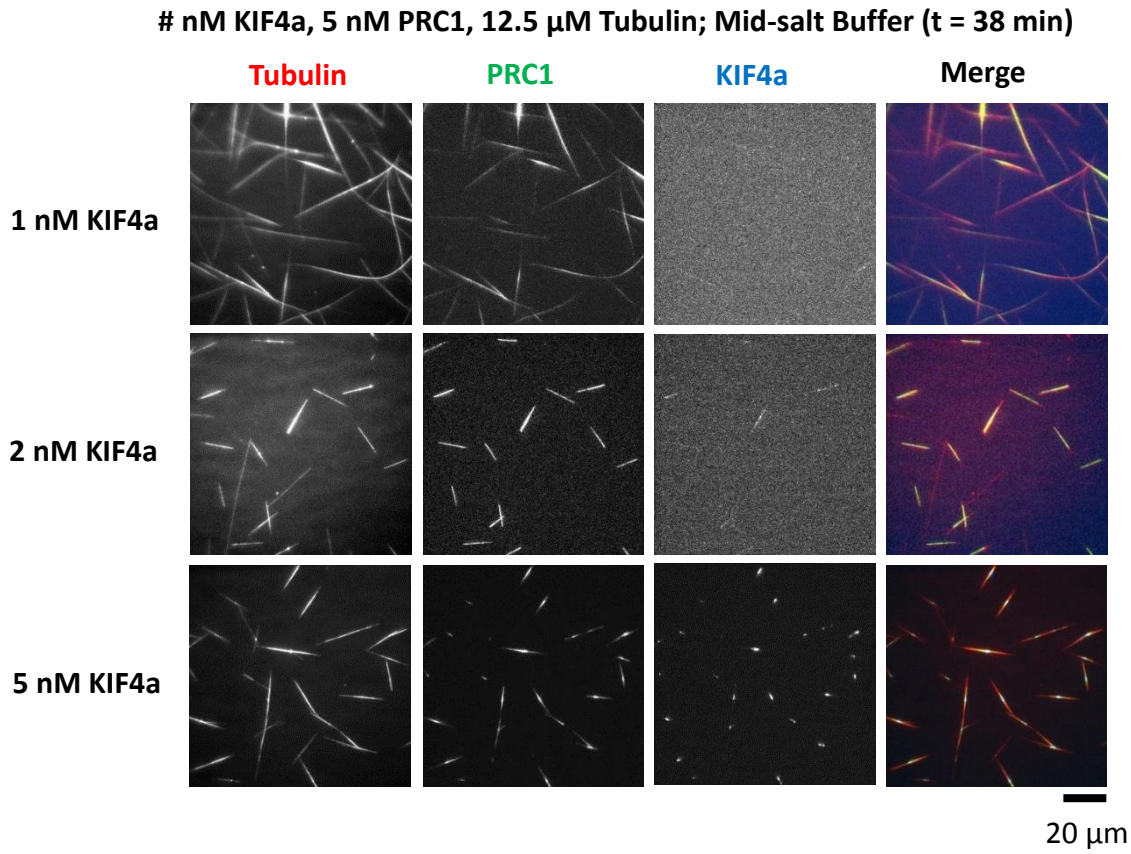

Figure 3.6: Reduction in KIF4a concentration leads to loss of dynamic suppression and sliding.
TIRF microscopy of self-organised MTs grown de novo. A series of different KIF4a concentrations, keeping PRC1 concentration at 5 nM. At 5 nM KIF4a both sliding and dynamic suppression evident. At 2 nM KIF4a, sliding is prevented, but dynamic suppression remains. At 1 nM KIF4a, neither sliding nor dynamic suppression function. Data are representative, results for all conditions have been reproduced two or more times on separate days with different protein batches.

the microtubule plus-end growth does appear to be suppressed in these experiments. This was made clearer when I reduced KIF4a concentration further, and found that overlaps simply kept on growing until an extensive bundle was formed.

If I was to understand the system, I needed a way of visualising how overlap length changed over time. As seen in the previous chapter, kymographs are a highly useful way of visualising the data to see how spatial characteristics change over time, be that protein distributions or overlap length measurements. Kymographs are essentially montages of 1 dimensional images. In previous examples we were looking at surface attached microtubules where change over time occurs only in 1 dimension. We now have non-surface-immobilised microtubules, which can diffuse in 2 dimensions. To extract 1 dimensional data from my new assay I needed a line that could move with, and track, the

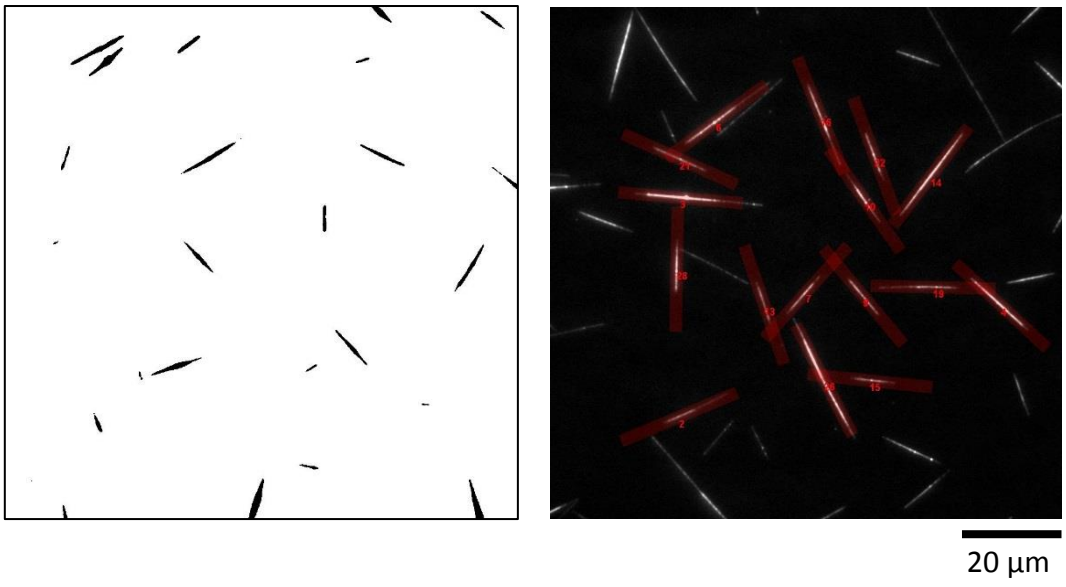

Figure 3.7: Kymograph tracking software produces kymographs from moving objects
Images produced in Fiji/ImageJ during the process of tracking spindles to produce kymographs. (Left) A threshold image used to determine the positions of spindles. Thresholds are altered manually at this stage to capture as much data and as little noise as possible. (Right) Tracking movie generated at the end of the process for linking numbered kymographs with spindles.

microtubules. To achieve this I used kymograph tracking software, developed by Dr. Nicholas Cade. This uses thresholding to identify the mini-spindles using the PRC1 channel (Fig 3.7). It then determines the orientation of the spindle from the orientation of the PRC1 channel, and extrapolates out a line from the centre. This works well across most time points, though faster diffusion at the beginning of the experiment, when bundles first appear on the surface, can make earlier time points more difficult to track.

When we observe the kymographs for the KIF4a reduction experiments, we can clearly see the presence or absence of sliding (Fig 3.8). The 5 nM case shows an initial growth, followed by narrowing of the overlap zone, just as was seen for the surface attached systems in (Fig 3.1). The left 2 nM case shows two microtubule bundles fusing together (~5 min from start of image capture), but there is no sliding, and so no further organisation. Minus-ends can still be seen growing out of these bundles. The 1 nM case

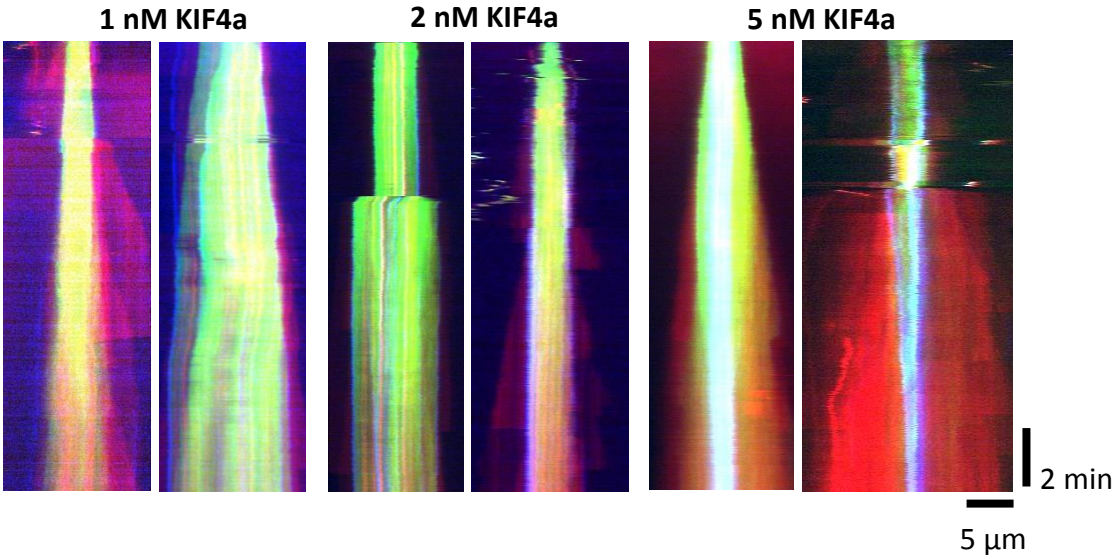

Figure 3.8: Kymographs of KIF4a reduction experiments
Kymographs of the conditions in (Fig 3.6) showing the presence or absence of sliding and plus-end growth suppression within microtubule bundles. (Red) Alexa647-Tubulin (Green) PRC1-Atto488 (Blue) KIF4a-mBFP. Start time represents the time at which the tracking software first detected the bundles. Tracking of the above cases all began within 2 minutes of the start of recording.

shows growing overlaps, even though there is evidence of KIF4a successfully accumulated at the plus-ends of some microtubules, and supressing their dynamics. It is as though there are too many plus-ends for the amount of KIF4a in the assay, meaning as some microtubules have their dynamics suppressed, others are freer to grow.

3.4 Increasing PRC1 Concentration Inhibits Sliding

In reducing the KIF4a concentration, I am changing more than just the level of one protein. I am also changing the ratio between the KIF4a and PRC1. Will increasing the PRC1 concentration have a similar effect to reducing the KIF4a concentration? I next kept the KIF4a constant at 5 nM, and raised the PRC1 concentration from 5-25 nM (Fig 3.9).

At 10 nM PRC1 and 5 nM KIF4a sliding still persisted. When I increased the concentration to 25 nM PRC1, though, the sliding stopped, and a phenotype reminiscent of that seen for 2 nM KIF4a and 5 nM PRC1 was seen. This posed the question: if raising PRC1 concentration prevents sliding, will reducing it rescue sliding? I therefore performed experiments at 2 nM KIF4a and 2 nM PRC1. In these experiments, sliding was, indeed, rescued.

It appeared that PRC1 was resisting the sliding, acting as a sort of brake, reminiscent of the work of Lansky et. al., which studied the yeast homologue of PRC1, Ase1. If this is the case then perhaps at high KIF4a concentrations, and low PRC1 concentrations, it would be possible to separate the overlap. When I performed experiments at 1 nM PRC1 and 100 nM KIF4a, spindles became hinged, as overlaps were slid apart to the extent where microtubules were simply tethered together at their plus-tips, meaning

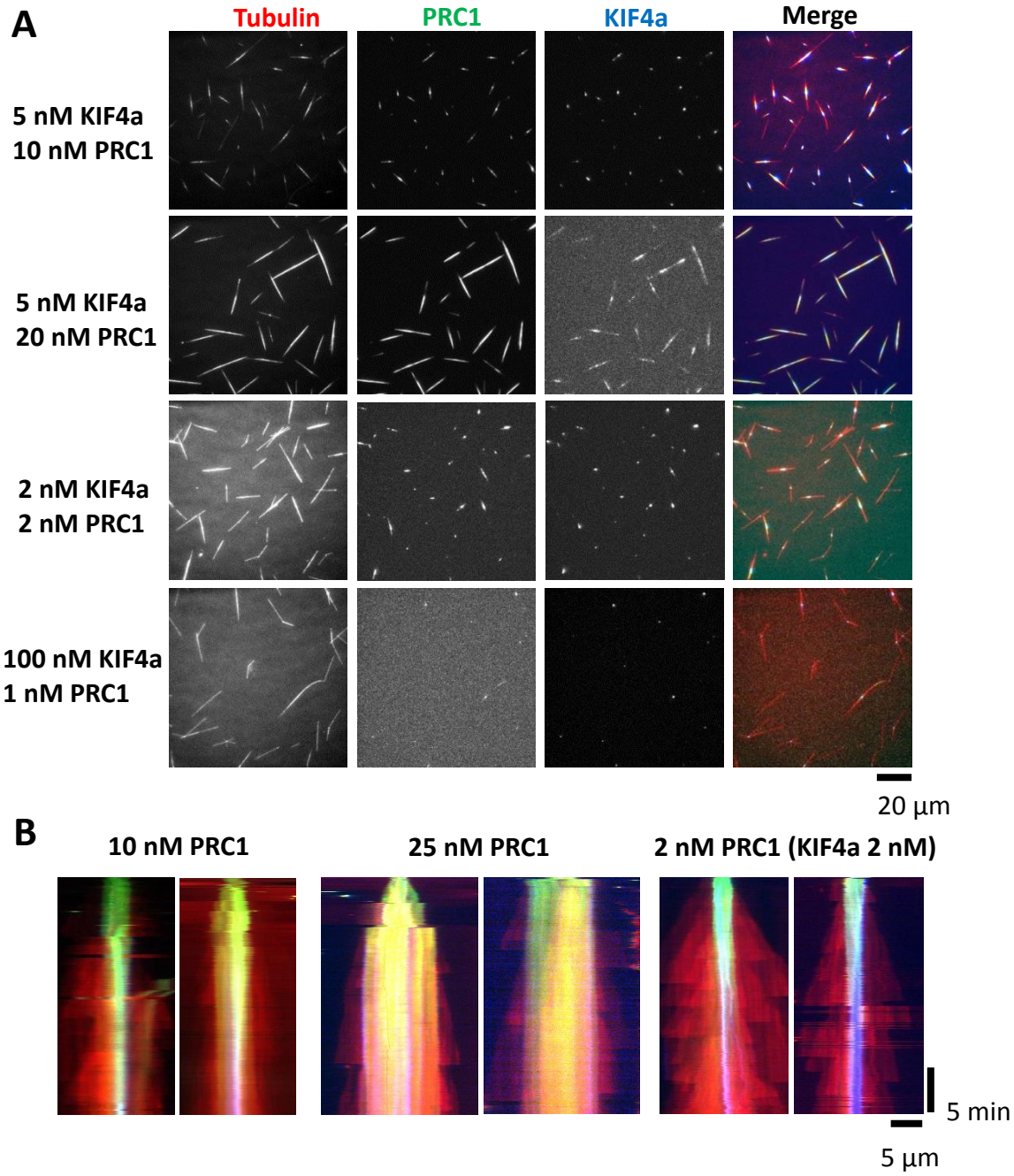

Figure 3.9: Increasing PRC1 concentration resists sliding, decreasing rescues it. TIRF microscopy of MTs grown de novo. (A) Series demonstrating how changing PRC1 concentration relative to KIF4a affects the system's ability to organise spindles. At 20 nM PRC1 and 5 nM KIF4a overlap focussing is highly limited (Middle-top). In the case of 2 nM KIF4a, reducing PRC1 concentration to 2 nM rescues sliding (Middle-bottom). At very low PRC1, overlaps can be effectively broken, leading to MT hinges, indicated by arrows (bottom). (B) Kymographs of the top 3 conditions in (A) taken from different experiments, channel colours as in (A). Tracking of the above cases all began within 2 minutes of the start of recording. Data are representative, results for all conditions have been reproduced two or more times on separate days with different protein batches, with the exception of 100 nM KIF4a and 1 nM PRC1 which has only been reproduced with the same batch of protein.

they were more characteristic of an aster-like organisation, rather than a central-spindle-like one (Fig 3.9A). Increasing the PRC1 concentration in solution or decreasing the KIF4a concentration in solution appears to increase the overlap length. However, these two proteins are known to interact with one another. Increasing the amount of PRC1 in overlaps, may simultaneously increase the amount of KIF4a, and vice versa. KIF4a may need PRC1 to crosslink microtubules. To better understand the contributions of each protein to the organisation of the system, I would need to perform control experiments where only one of either PRC1 or KIF4a were present.

3.5 KIF4a Requires PRC1 to Crosslink Microtubules

When I performed experiments with PRC1 alone (Fig 3.10), plus-ends were clearly able to grow uninhibited, and there was no evidence of any sliding. This resulted in cross-linked networks of microtubules, rather than the more isolated mini-spindles which form in the presence of KIF4a. PRC1's preference for antiparallel microtubule overlaps is also clear in these experiments. Higher concentrations of PRC1 led to denser bundles that covered a similar area of the field of view. This suggests there were more microtubules present in these experiments, which is to be expected, given the known propensity of PRC1 to act as a nucleating agent [99].

PRC1's selectivity for antiparallel overlaps can also be seen in these experiments. Initially short antiparallel bundles of microtubules form. Plus-ends grow out of these bundles, leading to parallel microtubule overlaps either side of the original bundle, where PRC1 does not bind. These plus ends can overlap with other microtubules in an antiparallel fashion. The example in Fig 3.11 shows how a free microtubule in solution can form antiparallel overlaps with the growing plus ends and recruit PRC1. This microtubule can

then grow towards the original bundle recruiting more PRC1, as more antiparallel overlap forms. When this microtubule grows through and out the other side of the original bundle, it overlaps with the microtubules growing out the other side, but no PRC1 is recruited, because it is now oriented parallel to these microtubules. A small amount of minus-end growth can also be seen in these experiments, which does extend the antiparallel overlap of the original bundle slightly. In the last 3 minutes of the timelapse in Fig 3.11 two higher density bundles become conjoined, but as can be seen, as with the free microtubule, there is no sliding bringing these two centres together. Having said that, there does form an antiparallel overlap bridge, and therefore PRC1 bridge, between the two.

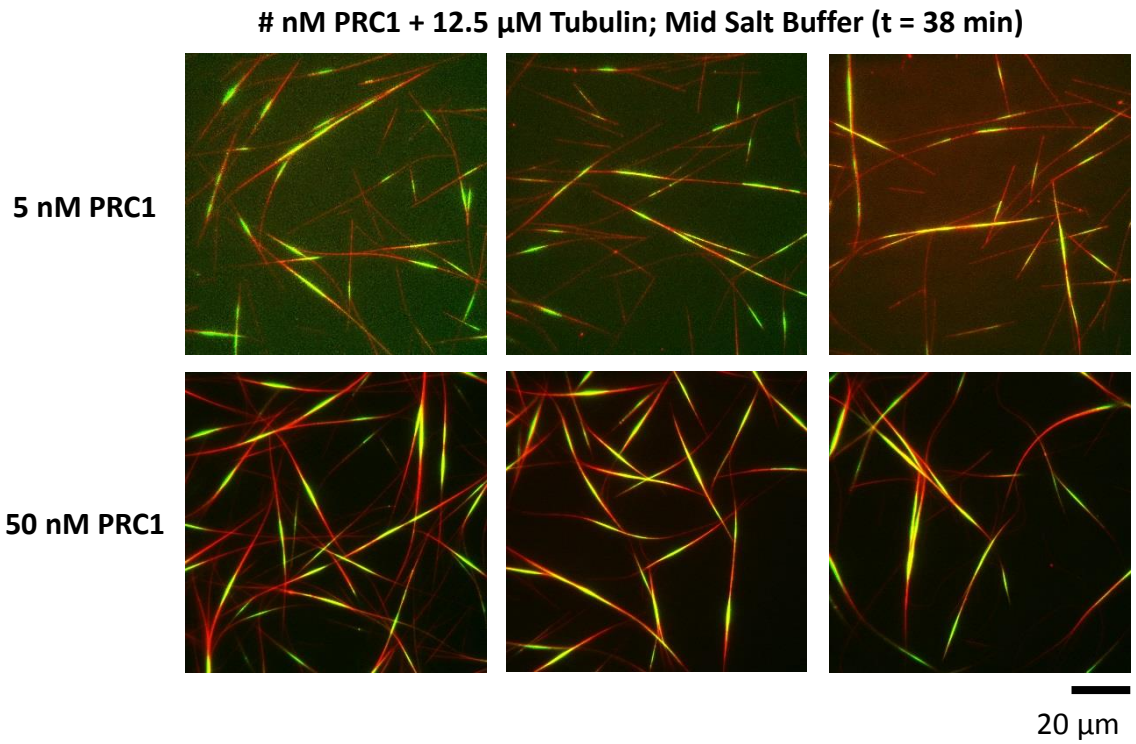

Figure 3.10: PRC1 is incapable of sliding, or controlling MT growth in the absence of KIF4a
TIRF microscopy of MTs grown de novo in solution. Experiments looking at PRC1 alone. MTs are clearly bundled, but there is no evidence of sliding or dynamic suppression. For each condition results were recorded from 3 separate experiments performed on the same day with the same protein batches.

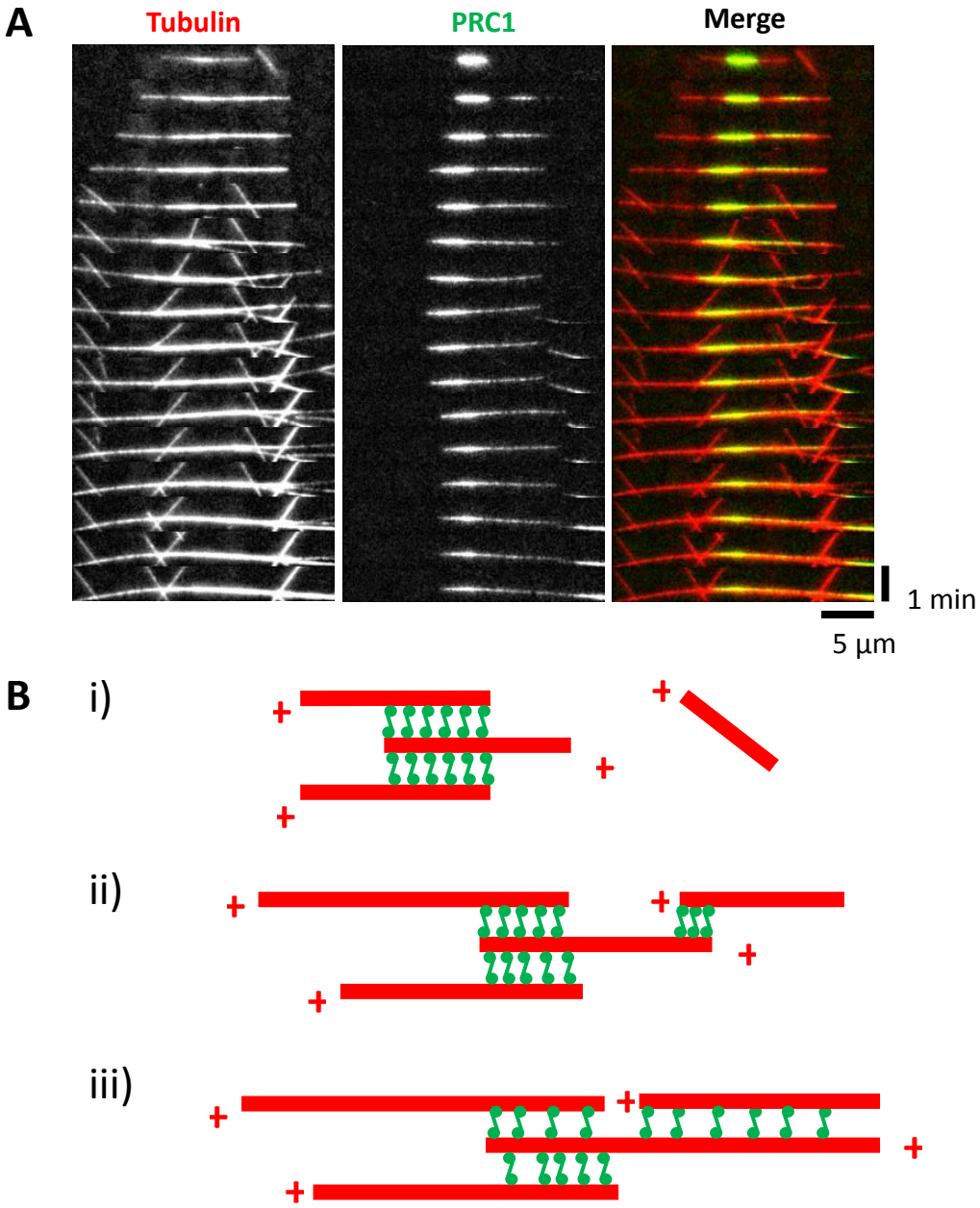

Figure 3.11: PRC1 selects for antiparallel overlaps
TIRF microscopy of MTs grown de novo in solution. (A) Timelapse showing MT antiparallel overlap formation, and Alexa546-PRC1 recruitment, between a free microtubule, and the microtubule plus-ends of an antiparallel bundle of microtubules. 5 nM PRC1 + 12.5 µM Tubulin; Mid Salt Buffer (B) Schematic demonstrating the initial stages of (A).

When I performed experiments with KIF4a alone (Fig 3.12), KIF4a could be seen at microtubule plus-tips of some of the microtubules, as was seen for the dynamic seed experiments in Fig 2.8. What was also clear was the lack of any microtubule crosslinking, and therefore the lack of any microtubule sliding. It follows that KIF4a alone can only bind single microtubules, but how then does it slide microtubules in the antiparallel overlap assay above? It is likely that KIF4a binds to PRC1, which can then bind to a second microtubule, allowing KIF4a to slide antiparallel microtubules over one another.

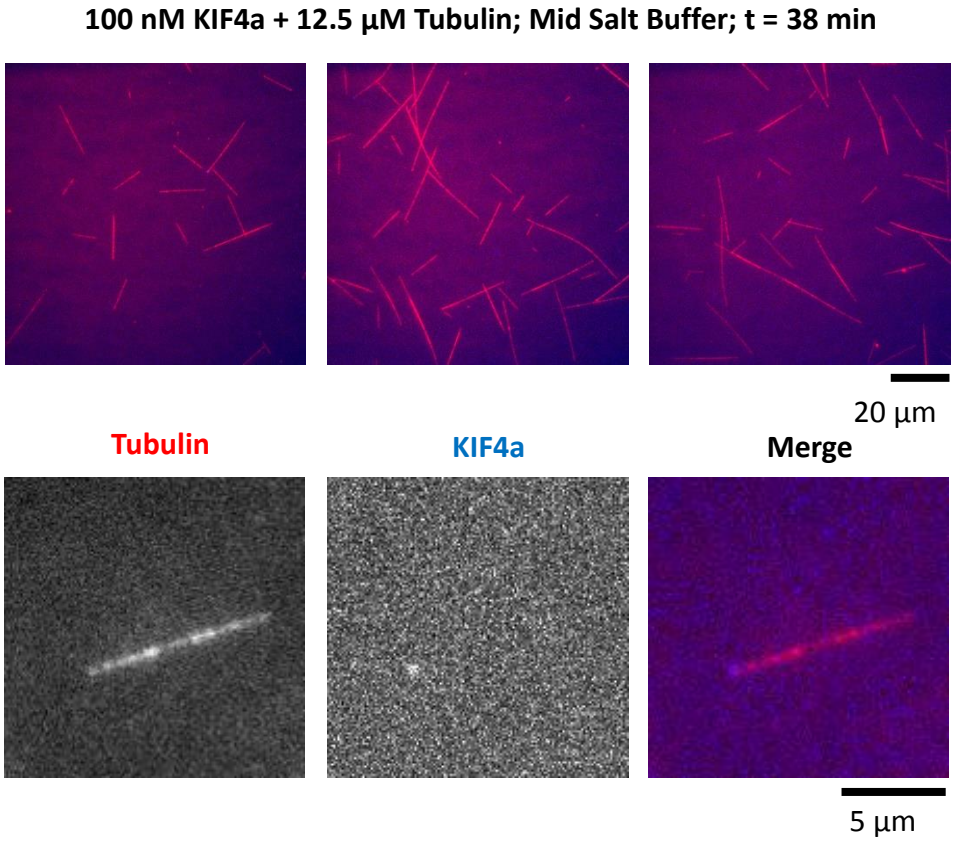

Figure 3.12: KIF4a alone is incapable of crosslinking microtubules.
TIRF microscopy images of dynamic microtubules grown *de novo* in the presence of mBFP-KIF4a. There is some degree of dynamic suppression, but microtubules are still able to grow. No evidence of MT crosslinking by KIF4a. MTs not bundled, though some do grow into one another. KIF4a visible on the plus-tips of some MTs. Results were recorded from 3 separate experiments performed on the same day with the same protein batches.

3.6 Spindle Growth Caused By Minus End Growth

Though KIF4a has been shown to suppress microtubule plus-end dynamics, it was not clear whether the growth of the spindle as a whole received any contribution from continued growth and sliding, similar to what has been seen for central spindles in cells [122]. Here the microtubules grow, and are slid apart, which results in stable overlap lengths. I added CAMSAP3ΔN, a minus-end capping protein that suppresses minus-end growth, to see the degree to which this would affect spindle length. In the presence of CAMSAP3ΔN, spindles appeared stunted, barely growing out beyond the overlap zone (Fig 3.13). This led to the conclusion that minus-end growth was the major contributor to overall spindle size.

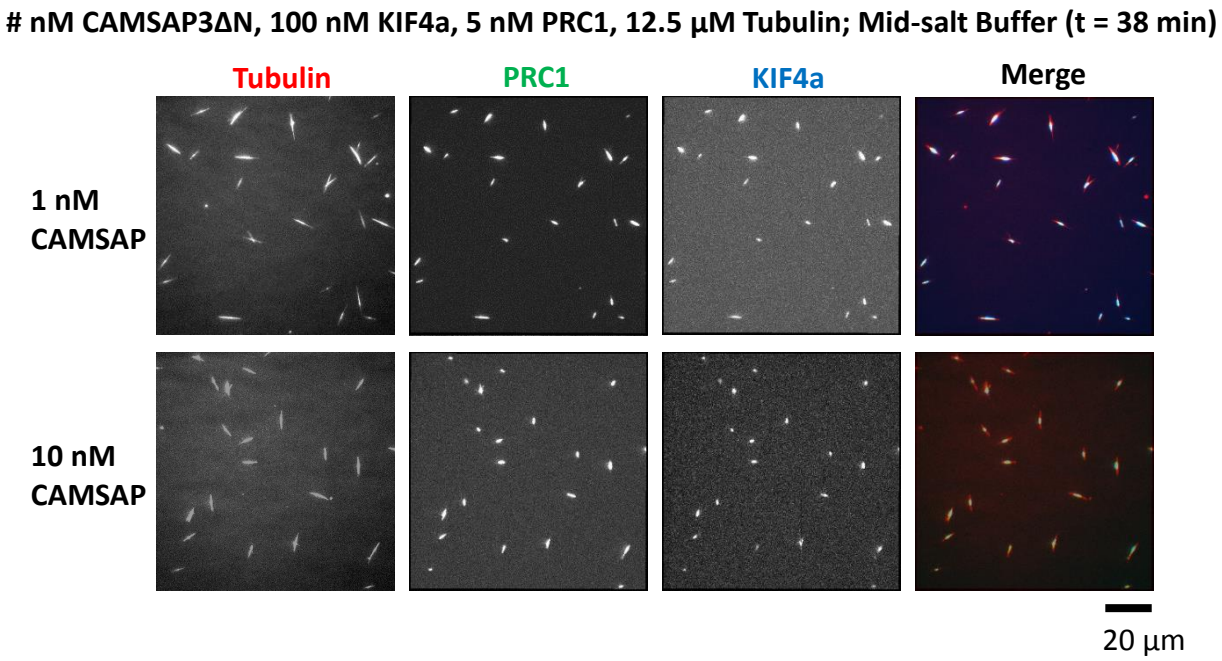

Figure 3.13: Addition of CAMSAP demonstrates the importance of minus-end growth in determining the length of mini-spindles
TIRF microscopy of MTs grown de novo. Experiments performed in presence of CAMSAP3ΔN, a minus-end capping protein, show very stunted spindles. Data are representative, results for each condition were reproduced twice on the same day with the same batch of proteins.

To test for the presence of any continued growth and sliding, I performed FRAP experiments in which I bleached a small section of microtubule adjacent to the overlap zone of already stable spindles (Fig 3.14). I then looked for any change in the distance between the overlap and the FRAP-site. If continued growth and sliding was occurring, one would expect to see the distance between the overlap zone and FRAP-site increase, as the FRAP-site was slid away. However, I observed no detectable change in the distance between the FRAP-site and the overlap zone, which led me to conclude that there was no flux occurring in the spindles, and that MT plus-ends are effectively non-dynamic in these overlaps.

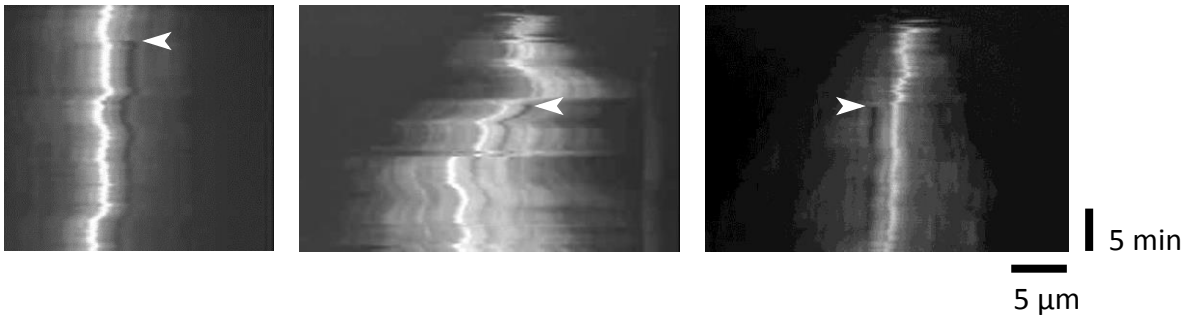

Figure 3.14: FRAP experiments demonstrate a lack of growth and sliding.
TIRF microscopy of MTs grown *de novo*. FRAP experiments of spindles confirm the absence of flux, and the primacy of minus-end growth for determining spindle length. Arrows indicate point of bleaching. Results are taken from two experiments performed on different days, but with the same batch of proteins.

3.7 Spindles Actively Fuse and Align With One Another

In cells, the overlaps of the central spindle are aligned neatly along the division plane. It is not obvious how overlaps are kept so well aligned. The ability of KIF4a to slide microtubules in the presence of PRC1 opens up the possibility that it could aid in the alignment of overlaps in the central spindle. As mentioned above, the anaphase mini-spindles diffused less as they grew, meaning that a lot of fusion events happened nearer

the start of the experiment during the small not-yet-polarised bundle phase (Fig 3.5 0-5 min), but fusion is still a common occurrence among more developed mini-spindles. When fusions occur, the PRC1/KIF4a dense overlapping region of spindle 1 comes into contact with the microtubules of another spindle, spindle 2. Initially, the microtubules of

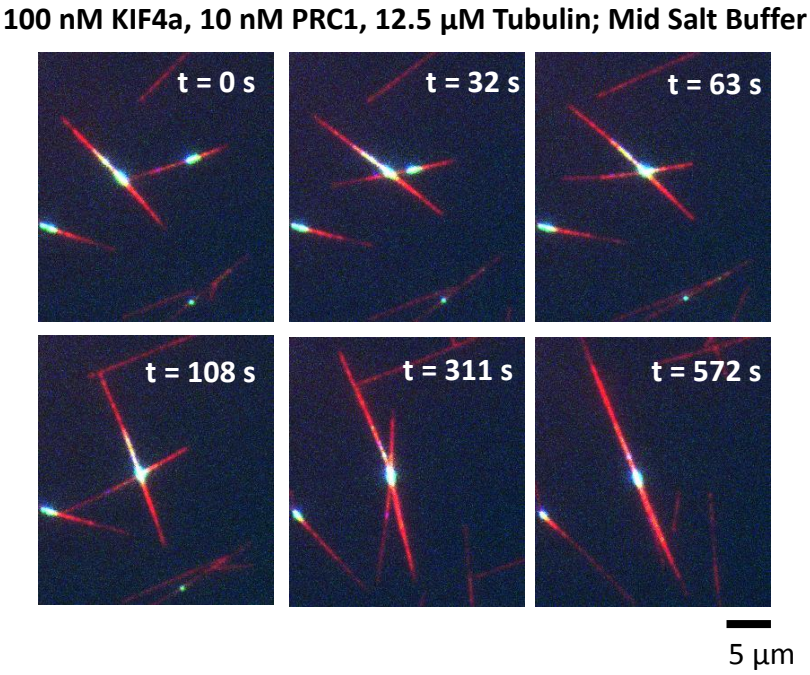

Figure 3.15: Overlaps move towards the plus-ends of naked MTs to find and align with others.
TIRF microscopy of MTs grown de novo. Time series showing the alignment of two spindles. An overlap comes into contact with a naked microtubule. This is followed by fusion and alignment. Data are representative. Fusion, alignment and buckling are common occurrences in this self-organisation assay across a broad range of protein concentrations, and as a result have been reproduced extensively.

the new spindle do not have to align at all with the microtubules of spindle 1, and even perpendicular angles of incidence are permitted (Fig 3.15). The overlapping region of spindle 1 walks towards the plus-end of spindle 2, hence finding and fusing with the overlap region of spindle 2.

Not only do overlaps come together, but the microtubules themselves then realign to give a spindle with a single axis. The ability of PRC1 to align microtubule axis in this way was

predicted from its structure [99]. Merging two microtubule bundles is not always sterically feasible. In these instances, microtubules buckle under the force, and this structural rearrangement can realign the spindles, allowing them to fuse. Fig 3.16 shows an example where buckling results in one spindles axis being flipped 180 degrees relative to the other before successfully fusing.

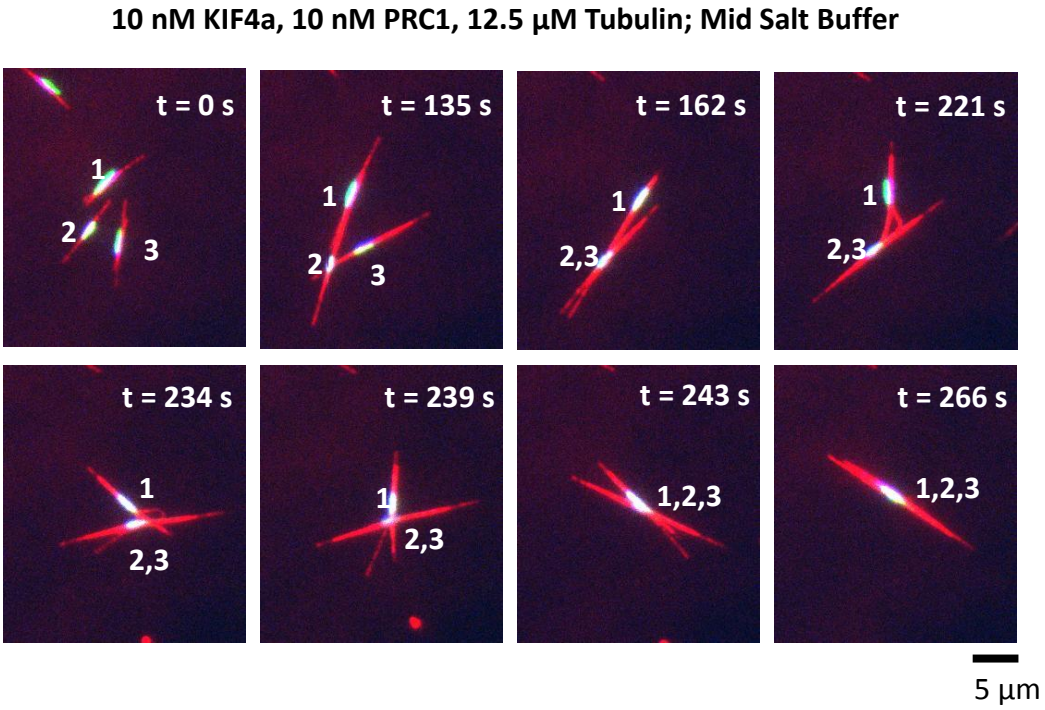

Figure 3.16: Steric hindrance leads to microtubule buckling in mini-spindle fusion events.
TIRF microscopy of MTs grown de novo. Fusion of 3 spindles, demonstrating buckling and flipping of one centre, as it struggles to combine the bundles of MTs. Data are representative. Fusion, alignment and buckling are common occurrences in this self-organisation assay across a broad range of protein concentrations, and as a result have been reproduced extensively.

The ability of overlap zones to walk directionally along the microtubules of other spindles, implies that KIF4a must be able to bind to the overlap region, while its motor can interact with a naked microtubule. As KIF4a has been shown not to crosslink

microtubules alone, it is most likely anchored to the overlap zone via its C-terminal interaction with PRC1, whilst its N-terminal motor heads interact with the second spindle.

3.8 Discussion

In this chapter I have established a novel assay which can be used to study the organisation of microtubule bundles *in vitro*. This goes beyond the previous *in vitro* work on several counts [76, 77, 120, 131]. I now look at bundles of microtubules, where only pairs were studied previously. The microtubules within these bundles are free to arrange in solution, rather than having their minus-ends surface immobilised. Both these advances combined allow for the study of bundle fusion and alignment. Additionally, microtubules are nucleated *de novo,* in solution, and are dynamic, with no small molecule synthetic stabilisers, such as paclitaxel or GMPCPP. Using this new assay I have shown that KIF4a and PRC1 alone can organise bundles into polarised spindles with a narrow band of overlapping MT plus-ends at the centre, and MT minus-ends emanating out on either side. This mirrors the underlying architecture and symmetry of the central spindle in cells. The ability of these spindles to align with one another, also points towards a mechanism by which central spindles in cells can remain aligned, especially during furrow ingression. Plus-ends appear to be non-dynamic in these spindles, with no evidence of flux, but plus-end dynamics are restored when KIF4a is removed. The absence of microtubule crosslinking in the absence of PRC1, suggests that KIF4a interacts with, and is therefore able to slide, a second microtubule via its interaction with PRC1. Despite KIF4a requiring PRC1 to crosslink and slide microtubules, too higher concentration of PRC1 relative to KIF4a prevents sliding.

In this chapter we have explored the boundaries of this novel system, where differences such as the presence and absence of sliding can be easily seen qualitatively. Between those boundaries, differences are far more nuanced. What controls the length of the overlap zone? PRC1 appears to act as a brake of some sort, but as already outlined above, KIF4a requires PRC1 to crosslink and slide microtubules, so increasing PRC1 concentration may simultaneously raise frictional resistance to sliding, and sliding activity of KIF4a. Likewise, PRC1 recruitment of KIF4a, and KIF4a recruitment of PRC1 are not mutually exclusive. Both these activities could operate in this system. To understand which factors are most important for determining overlap length, and to develop a working model for central spindle organisation, it is therefore necessary to perform quantitative analysis on the data.

Chapter 4: A Model of Self-Organising Microtubule Bundles

In this chapter I try to understand which parameters are important for determining the overlap length in the anaphase mini spindles described in the previous chapter. How do the solution concentrations of PRC1 and KIF4a affect overlap lengths? How do protein levels in the overlap change over time? After answering these questions, I will propose a model that can incorporate these results, and the results of the previous two chapters.

4.1 Collecting and Measuring Data

To gather data for quantitative analysis, I performed experiments as described in the previous chapter, by combining KIF4a-mBFP, Alexa546-PRC1 and Alexa-647 labelled tubulin in MSB buffer. The tubulin concentration was kept at 12.5 μM, and the PRC1 and KIF4a concentrations were varied to form a series. Data was collected during the progress of these experiments for 38 minutes, after which, still images were taken in various parts of the sample, giving two sets of data, a dynamic time course set of image stacks, and an end point set of individual stills. This time point was chosen, as overlap lengths appeared to have stabilised by this time over most conditions.

Fig 4.1 shows a selection of representative line plots demonstrating how overlap length changes over time. It can be seen that in most of the cases shown there is a period of growth, followed by shrinkage, and then stabilisation. Those that don't show a growth phase either begin at a later time point, or involve higher PRC1 concentration. The latter is due to PRC1 acting as a nucleating agent [99]. At low PRC1 concentrations, there is normally a lag time before microtubules begin to appear, meaning the imaging can begin

at the same time as the process. However, at higher PRC1 concentrations, the process begins much sooner, and so for technical reasons, the imaging generally starts slightly

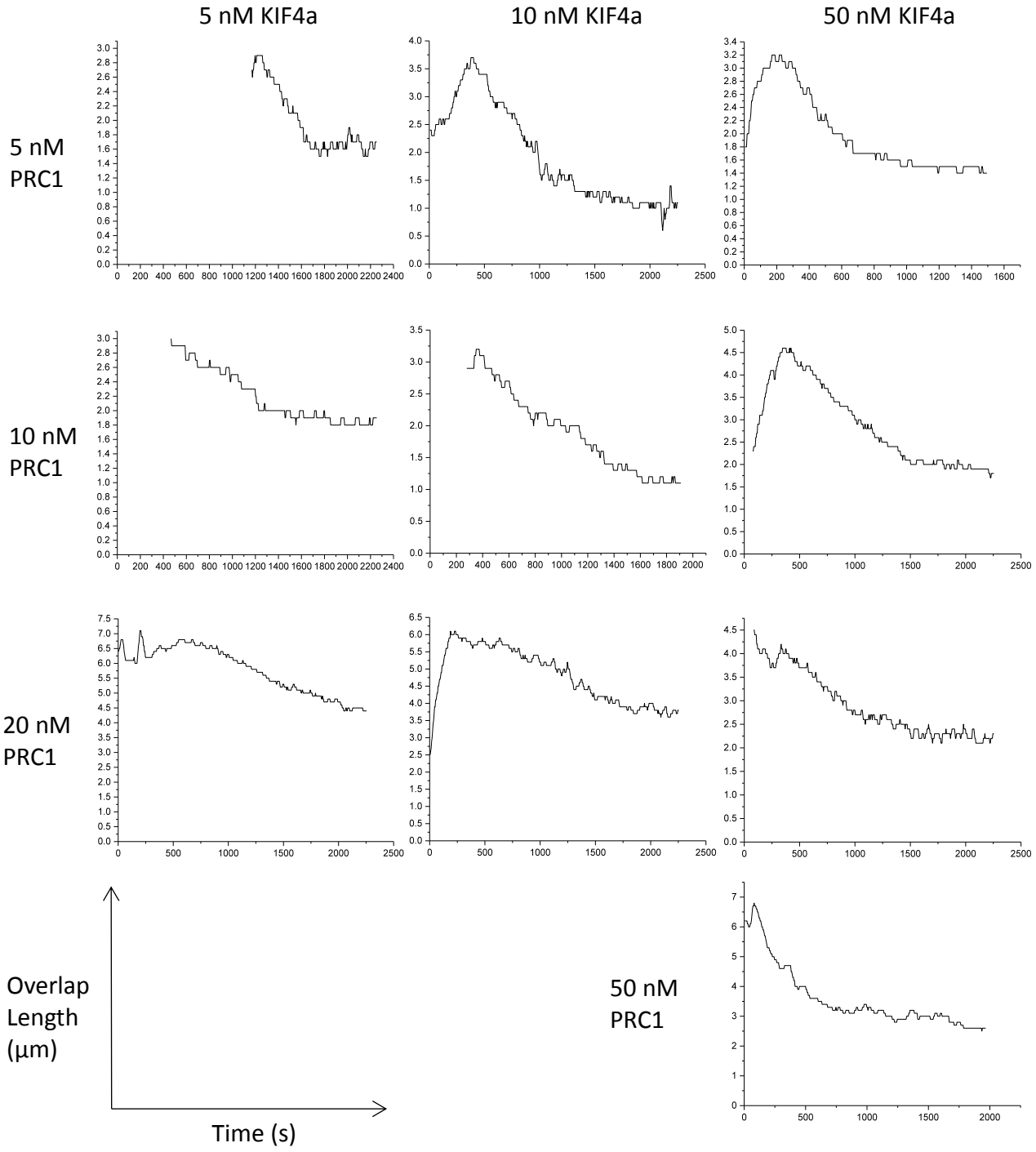

Figure 4.1: Overlaps have mostly stabilised by the time of end point analysis
Line plots showing how overlap length changes over time. An example is shown from each concentration condition. Time (s) is along the X axis, with overlap length (µm) along the Y axis. Most overlaps have stabilised by the time end point data was collected (38 min).

after the process. When observing the start of the experiment under the microscope, it appears as though the growth phase is primarily due to fusion with other early stage bundles, and incorporation of more microtubules. These step-wise processes are not perfectly coordinated in time, even within a concentration condition, and so trying to average over several of these tracks can be misleading, if one is trying to deduce a mechanism by assuming that the mean is a fair representation of a single event. I will, therefore, look at individual case studies for this data set. For the end point analysis, on the other hand, where overlaps are assumed to have stabilised, it becomes valid and useful to study the mean values.

For kymographs generated from image stacks, I measure the overlap length, and intensity profiles across all channels within the overlap, for every timepoint, using a semi-automated procedure (see chapter 5.7.1). A similar semi-automated procedure was used to make the same measurements of the single image end point data (see chapter 5.7.2). Overlaps were determined using the PRC1 channel. At least 93 individual bundles were measured for each concentration condition. These are taken from two independent experiments for each condition. For a breakdown of n numbers for each concentration condition see Table 5.1. Unlike previous chapters, all data in this chapter is taken from experiments performed using protein taken from a single purification. This is to avoid any error which may occur in the measurement of protein concentration, or the labelling ratio of proteins labelled with synthetic dyes, which may otherwise create unnecessary noise in the data when comparing conditions.

4.2 Increasing PRC1 concentration and reducing KIF4a concentration increases overlap length

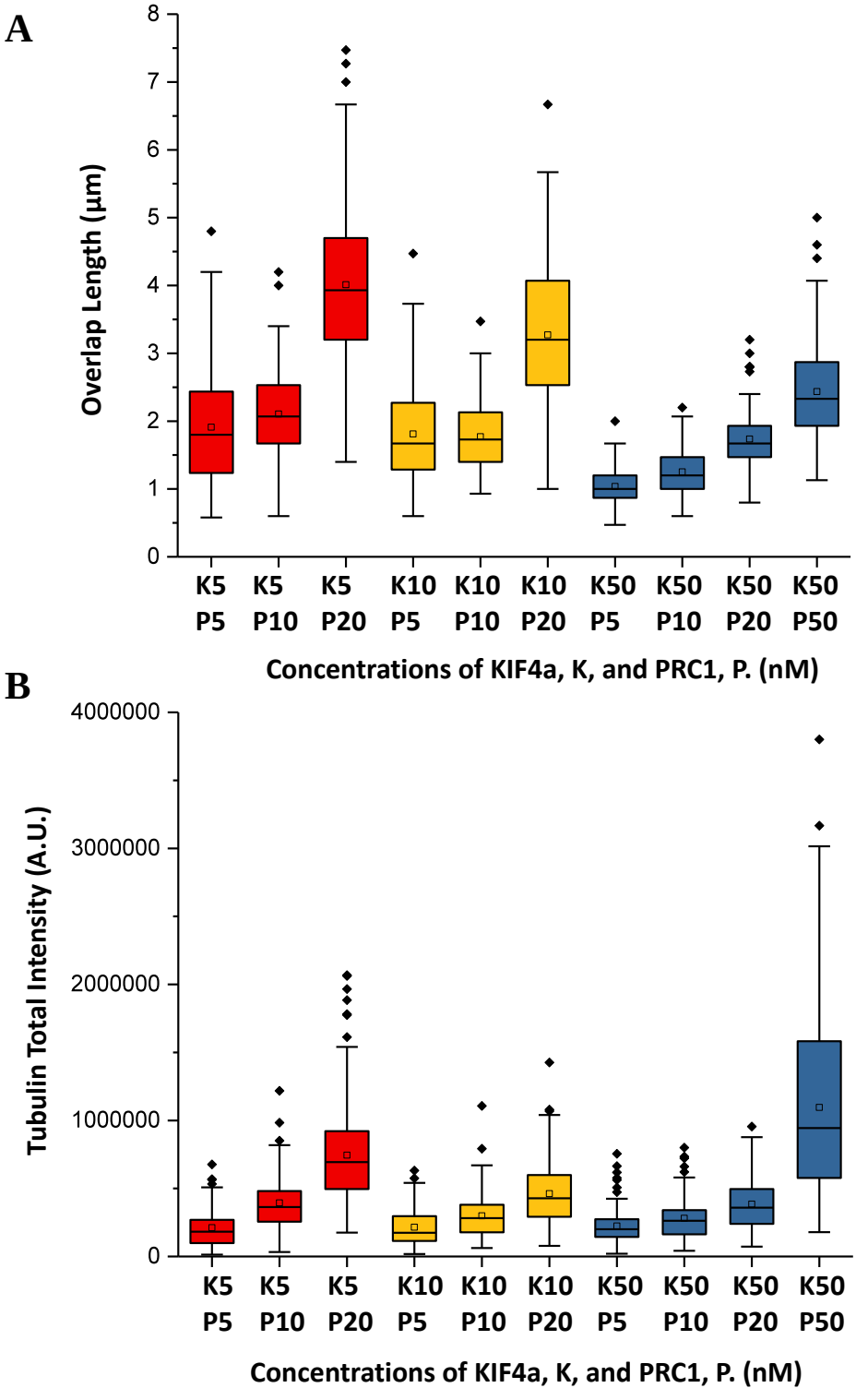

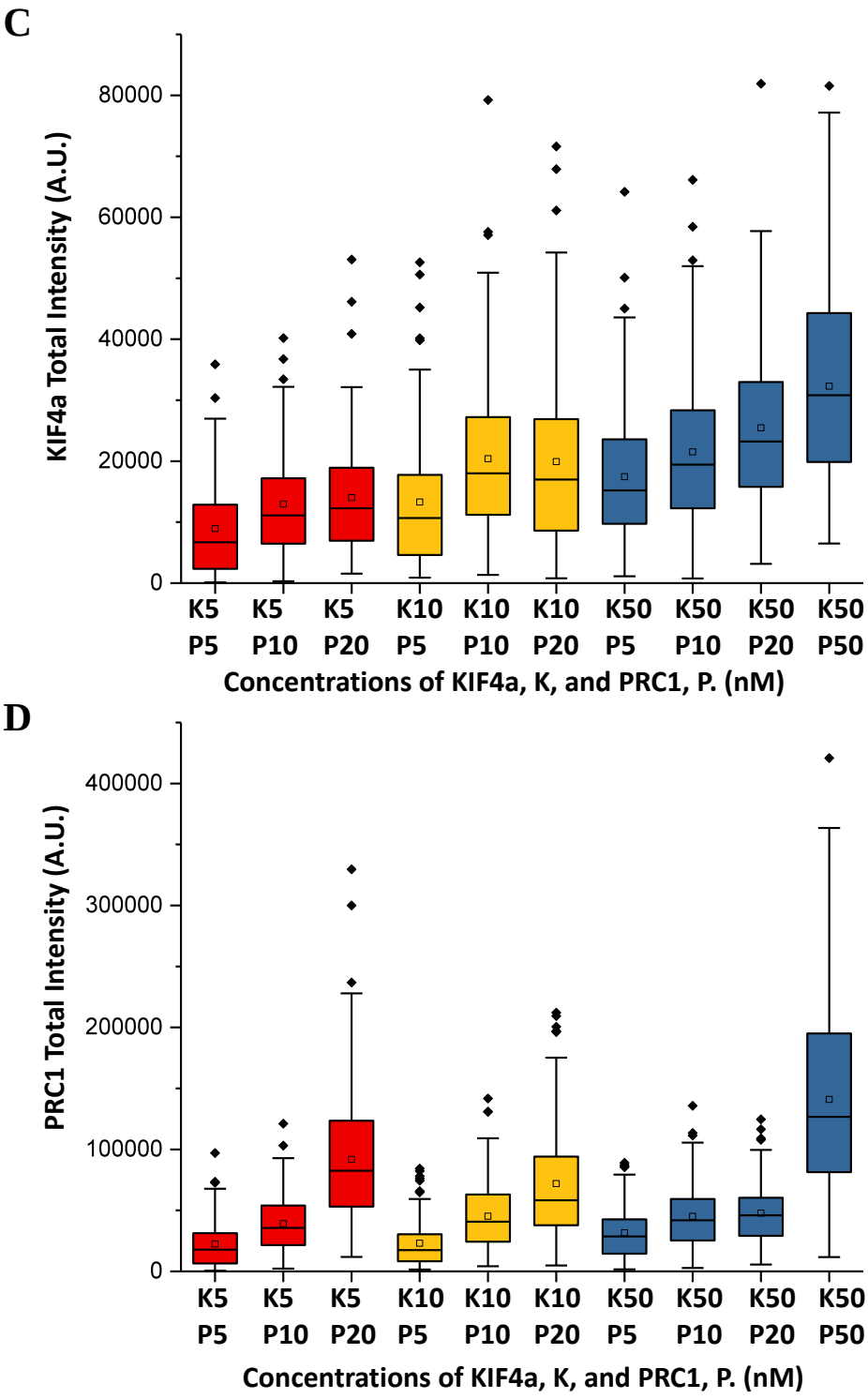

Figure 4.2: Box plots of overlap length and Tubulin, KIF4a and PRC1 Total intensities
Box plots showing distributions of directly measured variables for a given PRC1 and KIF4a concentration at t = 38 min: (A) overlap length; (B) Alexa647-tubulin total intensity; (C) KIF4a-mBFP total intensity; (D) Alexa546-PRC1 total intensity. (Red) 5 nM KIF4a, (Yellow) 10 nM KIF4a, (Blue) 50 nM KIF4a. Box represents IQR, whiskers represent range (-outliers), ♦ = outliers (>1.5*IQR) box line = median, □ = mean. See Table 5.1 for n numbers.

It can be seen from Fig 4.2A that increasing the PRC1 concentration in solution results in an increase in the mean overlap length at a given KIF4a concentration, and that increasing the KIF4a concentration in solution results in a decrease in the mean overlap length at a given PRC1 concentration. This is in keeping with the previous chapter, where a high PRC1 concentration relative to KIF4a concentration appeared to prevent overlap focussing, while a high KIF4a concentration relative to PRC1 concentration appeared to separate overlaps.

Fig 4.2B shows how the tubulin total intensity, Tub_{Int}, within the overlap changes for different KIF4a and PRC1 concentration conditions. Tub_{Int} is proportional to the total microtubule mass in the overlap, and so unsurprisingly, it shows a positive correlation when plotted against overlap length (Fig 4.4A). Tub_{Int} will also be affected by the number of microtubules in the bundle, however, and so should not be seen as directly proportional to overlap length. Measuring the exact number of microtubules in a bundle is technically difficult, and so I instead derive a proxy for this by dividing the Tub_{Int} by the overlap length to give a value approximately proportional to the number of microtubules, MT_n. MT_n showed no clear correlation with overlap length, and showed no clear trend across different concentration conditions, with the notable exception of the 50 nM PRC1 50 nM KIF4a condition, which resulted in much denser bundles. Microtubules appeared much faster in these experiments, and in greater number, suggesting that the denser bundles are the result of increased nucleation efficiency at 50 nM PRC1. It is also noted that all 50 nM KIF4a conditions show greater tubulin density. By limiting the length of microtubules, high KIF4a concentrations may indirectly result in increased nucleation events, as shorter bundles will contain less PRC1 and tubulin, increasing PRC1 and tubulin concentration in solution, leading to more microtubule nucleation events.

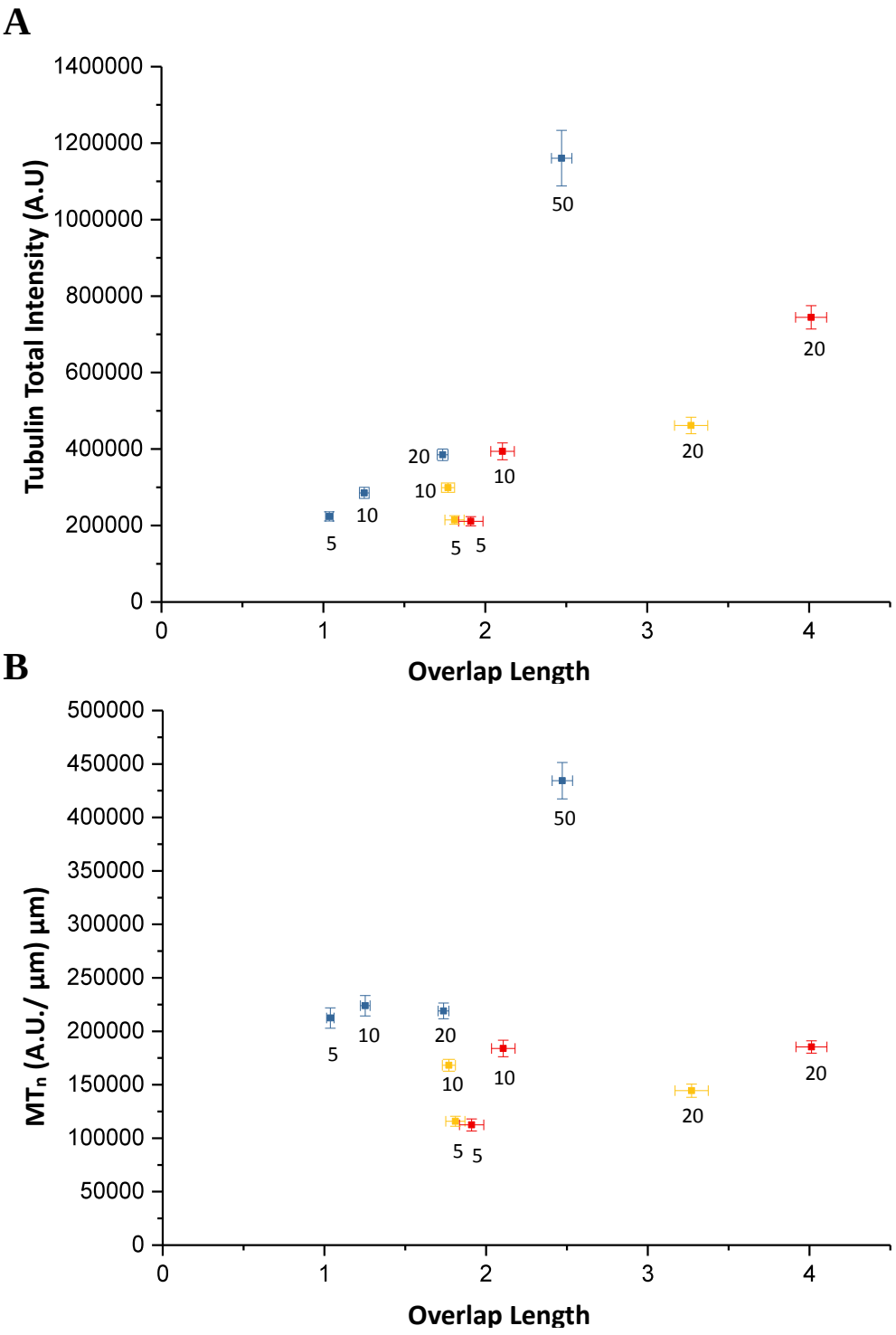

Figure 4.3: Scatter plots comparing overlap length with tubulin total intensity and density.
Scatter plots showing mean values of conditions in [Fig 4.2]. (A) Tubulin total intensity vs overlap length. (B) MT_n (tubulin total intensity divided by overlap length) vs overlap length. Error bars correspond to the standard error of the mean. Number labels correspond to PRC1 concentration in nM. Colour corresponds to KIF4a concentration: (Red) 5 nM KIF4a, (Yellow) 10 nM KIF4a, (Blue) 50 nM KIF4a. See Table 5.1 for n numbers.

Fig 4.2C/D shows how the PRC1 and KIF4a total intensities, $PRC1_{Int}$ and $KIF4a_{Int}$ respectively, change with changing protein concentrations. These values are proportional to the number of protein molecules within the overlap. $PRC1_{Int}$ follows a similar trend to overlap length, showing a positive trend with rising PRC1 concentration, though unlike overlap length, there is little evidence of a trend with regards to KIF4a concentration. $KIF4a_{Int}$, like $PRC1_{Int}$, shows a positive trend with rising PRC1 concentration, but it also shows a positive trend with rising KIF4a concentration. None of the directly measured intensity variables, nor the number of microtubules in a bundle, can explain the trends seen for overlap length alone. Work in the previous chapter suggested that KIF4a and PRC1 may act antagonistically with one another, and so it may be the ratio between the numbers of molecules of the two proteins, and so the ratio between $PRC1_{Int}$ and $KIF4a_{Int}$, that is important for deciding the overlap length.

4.3 PRC1/KIF4a ratio correlates with overlap length

When I plotted overlap length as a function of the ratio of PRC1/KIF4a concentration in solution, it appeared to show a non-linear correlation (Fig 4.4A). Ratios of concentration do not necessarily correspond to the actual ratio seen in the overlap, however, and so I plotted the overlap length as a function of the ratio of the total intensities measured in the overlap ($PRC1_{Int}$ /$KIF4a_{Int}$) (Fig 4.4B). This relationship appeared far more linear, and had a Pearson correlation coefficient of 0.92, higher than any other variable tested against overlap length, including PRC1 and KIF4a intensities (See Appendix 1 for correlation map). This suggests that the ratio between PRC1 and KIF4a in the overlap may be a factor in determining the overlap length.

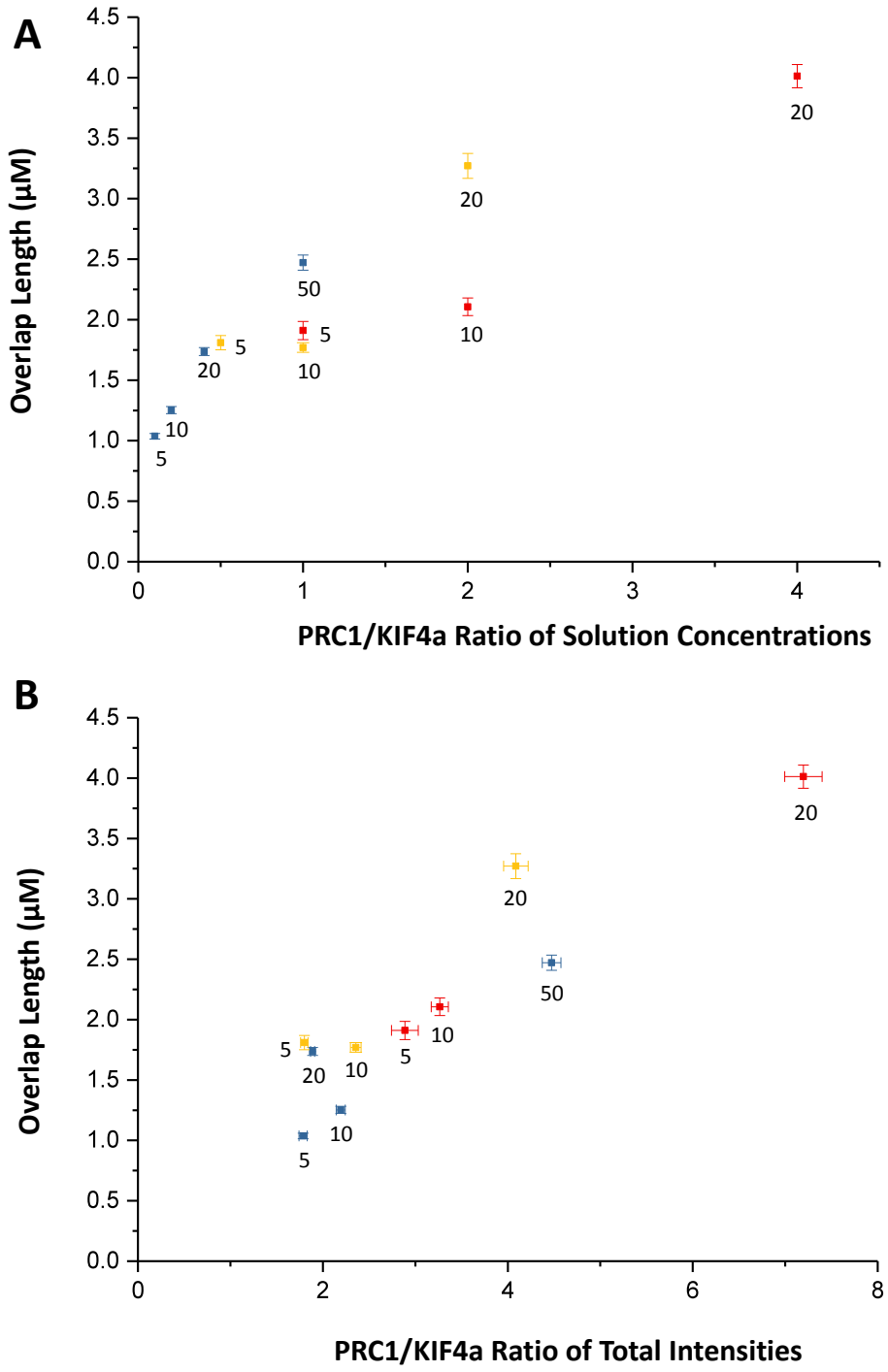

Figure 4.4: Scatter plots comparing overlap length with PRC1/KIF4a concentration and total intensity ratios.
Scatter plots showing mean values. Error bars correspond to the standard error of the mean. (A) Overlap length vs. (B) Tubulin density (tubulin total intensity divided by overlap length) vs overlap length. Number labels correspond to PRC1 concentration in nM. Colour corresponds to KIF4a concentration: (Red) 5 nM KIF4a, (Yellow) 10 nM KIF4a, (Blue) 50 nM KIF4a. See Table 5.1 for n numbers.

The ratio of $PRC1_{Int}$ /$KIF4a_{Int}$ in the overlaps was seen to correlate with overlap length, but what does this mean with regards to a model mechanism for determining spindle overlap length? A model for determining overlap lengths that relies solely on the formation of end caps, as seen in chapter 2, would predict similar ratios across all conditions, as it relies on KIF4a transporting PRC1 to plus ends in a ~1:1 stoichiometry [77]. The data does not support this hypothesis.

A model that relies on PRC1 acting as a brake, does allow for differing ratios at differing overlap lengths [120]. Increasing the PRC1 concentration would increase the fraction of microtubule sites occupied by PRC1 in the overlap, increasing the frictional resistance to KIF4a sliding, and resulting in longer overlaps at a greater $PRC1_{Int}$/$KIF4a_{Int}$ ratio. Increasing the KIF4a concentration would allow for greater compression of the overlap, resulting in shorter overlaps at a smaller $PRC1_{Int}$/$KIF4a_{Int}$ ratio. This version of the slide and brake model would predict that the fraction of microtubule sites occupied by PRC1 in the overlap would increase with increasing KIF4a concentration, due to increased compression. Tub_{Int} is proportional to the total microtubule mass. By dividing $PRC1_{Int}$ and $KIF4a_{Int}$ by Tub_{Int}, we get a value proportional to the fraction of microtubule sites occupied by PRC1 and KIF4a within the overlap. When observing the change in these new variables across different conditions, we see that the $PRC1_{Int}$ /Tub_{Int} does not show any clear trend, and remains similar across all conditions, especially when compared with how other variables change under different conditions (Fig 4.5B). The 50 nM KIF4a 5 nM PRC1 condition, for example, has almost the same mean and distribution as the 5 nM KIF4a 20 nM PRC1 condition, despite having the most divergent overlap lengths. This data does not uphold the predictions of the slide and brake model, as described above.

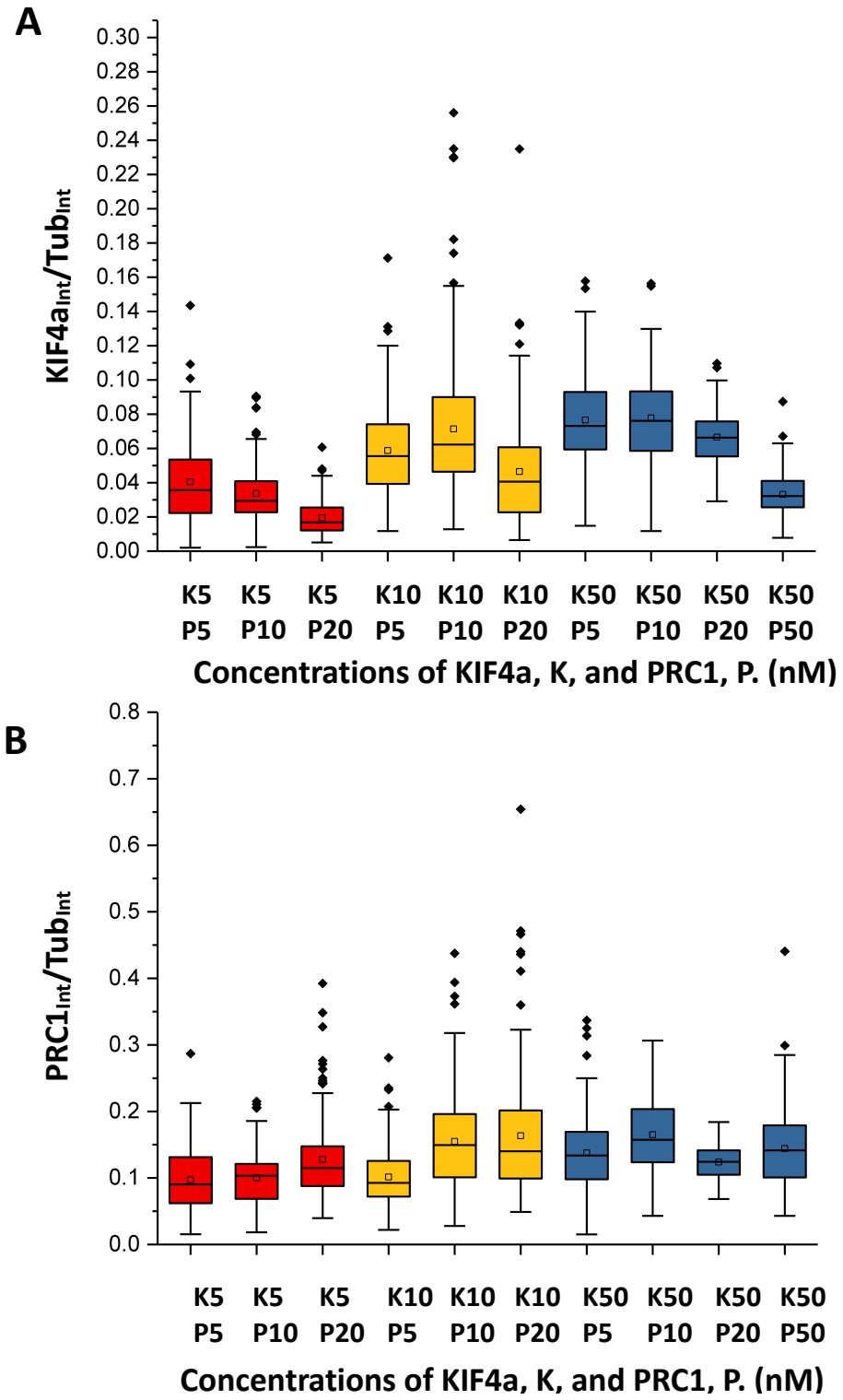

Figure 4.5: Box plots of PRC1 and KIF4a total intensities / total tubulin intensity
Box plots showing changes in directly measured variables: KIF4a/tubulin total intensities (top) and PRC1/ tubulin total intensity (Bottom). (Red) 5 nM KIF4a, (Yellow) 10 nM KIF4a, (Blue) 50 nM KIF4a. Box represents IQR, whiskers represent range (-outliers), ♦ = outliers (>1.5*IQR) box line = median, □ = mean. See Table 5.1 for n numbers.

When we observe how the $KIF4a_{Int}/Tub_{Int}$ changes across different conditions, it shows a general negative correlation with increasing PRC1 concentration, and a positive correlation with increasing KIF4a concentration, the opposite of the overlap length. The Pearson correlation coefficient of $KIF4a_{Int}/Tub_{Int}$ vs overlap length is -0.81. This negative correlation does not necessarily result from the amount of KIF4a in the overlaps decreasing. A given amount of KIF4a will take up a smaller fraction of a larger overlap, assuming the number of microtubules does not decrease. To test this hypothesis I looked at the amount of KIF4a per microtubule, $KIF4a_{Int}/MT_n$.

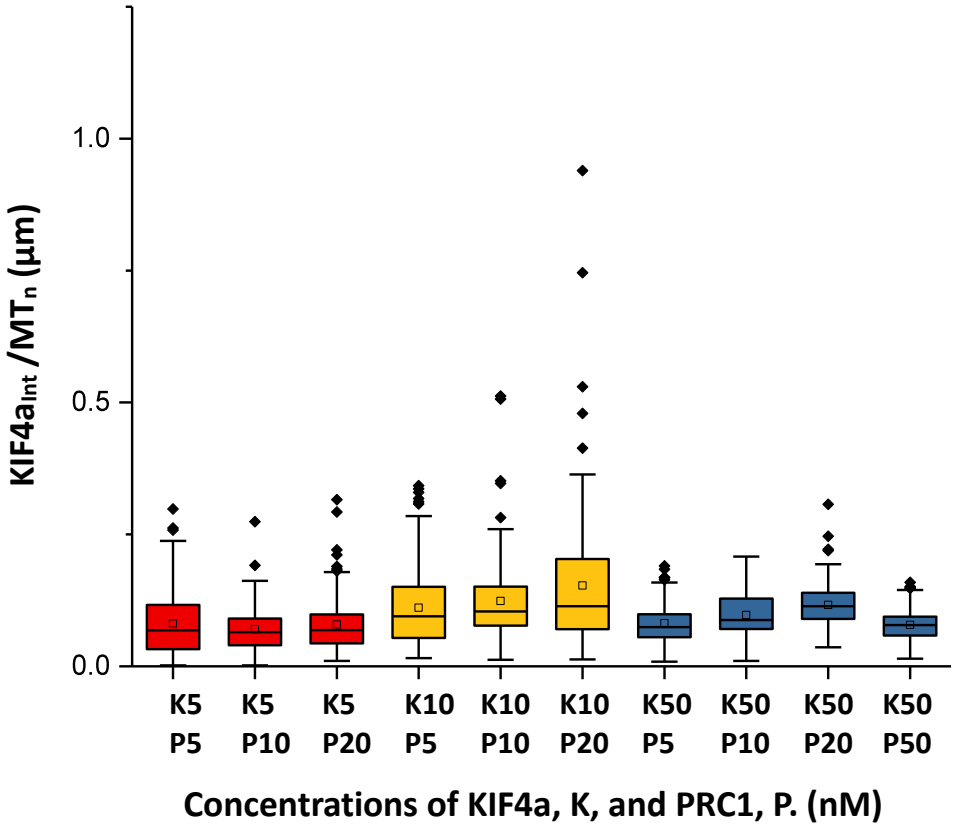

Figure 4.6: Box plot of KIF4a total intensity/ tubulin density
Box plots showing changes in directly measured variables: overlap length (top) and Alexa647-tubulin total intensity (Bottom). (Red) 5 nM KIF4a, (Yellow) 10 nM KIF4a, (Blue) 50 nM KIF4a. Box represents IQR, whiskers represent range (-outliers), ♦ = outliers (>1.5*IQR) box line = median, □ = mean. See Table 5.1 for n numbers.

When we observe the $KIF4a_{Int}/MT_n$ across different conditions, we again see little sign of a clear trend, and as with $PRC1_{Int}/Tub_{Int}$, the two most extreme conditions with regard to overlap length (5 nM KIF4a, 20 nM PRC1 and 50 nM KIF4a, 5 nM PRC1) appear remarkably similar. Based on this evidence, the strong correlation between overlap length and $PRC1_{Int}/KIF4a_{Int}$ is most likely a consequence of the amount of KIF4a per microtubule remaining the same, and the density of PRC1 in the overlap remaining the same. If these two variables remain similar across all conditions at the end of the experiment, how do they arrive at these values, and how then is the overlap length determined? To answer this question, we must study how these variables change over time.

4.4 KIF4a per microtubule tracks overlap length

By plotting variables derived from kymographs against time, we see that at the start of the experiment, $PRC1_{Int}/Tub_{Int}$ is always far higher than at the end (Fig 4.7). Most of the decline appears to happen early on in the experiment, and appears primarily due to the growth in tubulin intensity as bundles fuse and grow (see chapter 3.2). Some of this decline may be due to bleaching. Mean values at the end of the experiment, post-illumination, are approximately half those measured for the non-illuminated end point images in Fig 4.7 (see Appendix 2). However, the mean peak $PRC1_{Int}/Tub_{Int}$ is on average 3 x greater than the non-illuminated end point mean, and the fall in mean $PRC1_{Int}/Tub_{Int}$ is on average 4 x greater than the difference between the illuminated and non-illuminated end point means, so the magnitude of the change, outweighs any measurable effect of bleaching.

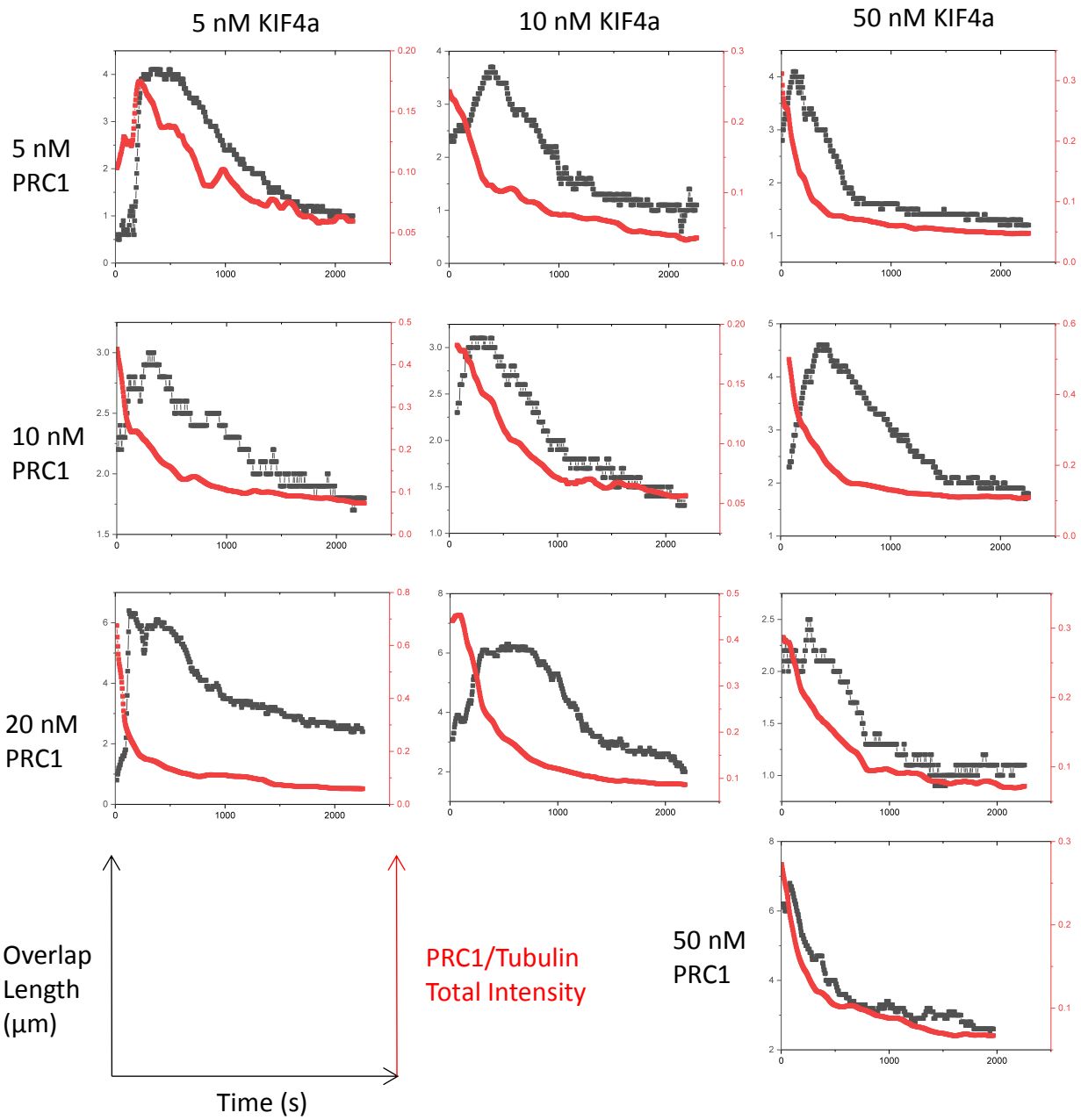

Figure 4.7: Line plots comparing overlap length and PRC1/Tubulin ratio over time
Line plots showing how overlap length and PRC1/Tubulin ratio changes over time. An example is shown from each concentration condition. Time (s) is along the X axis, with overlap length (µm) along the black Y axis, and PRC1/Tubulin ratio along the red Y axis. Axis have been auto scaled in OriginPro2017 for comparison between overlap length and PRC1/Tubulin.

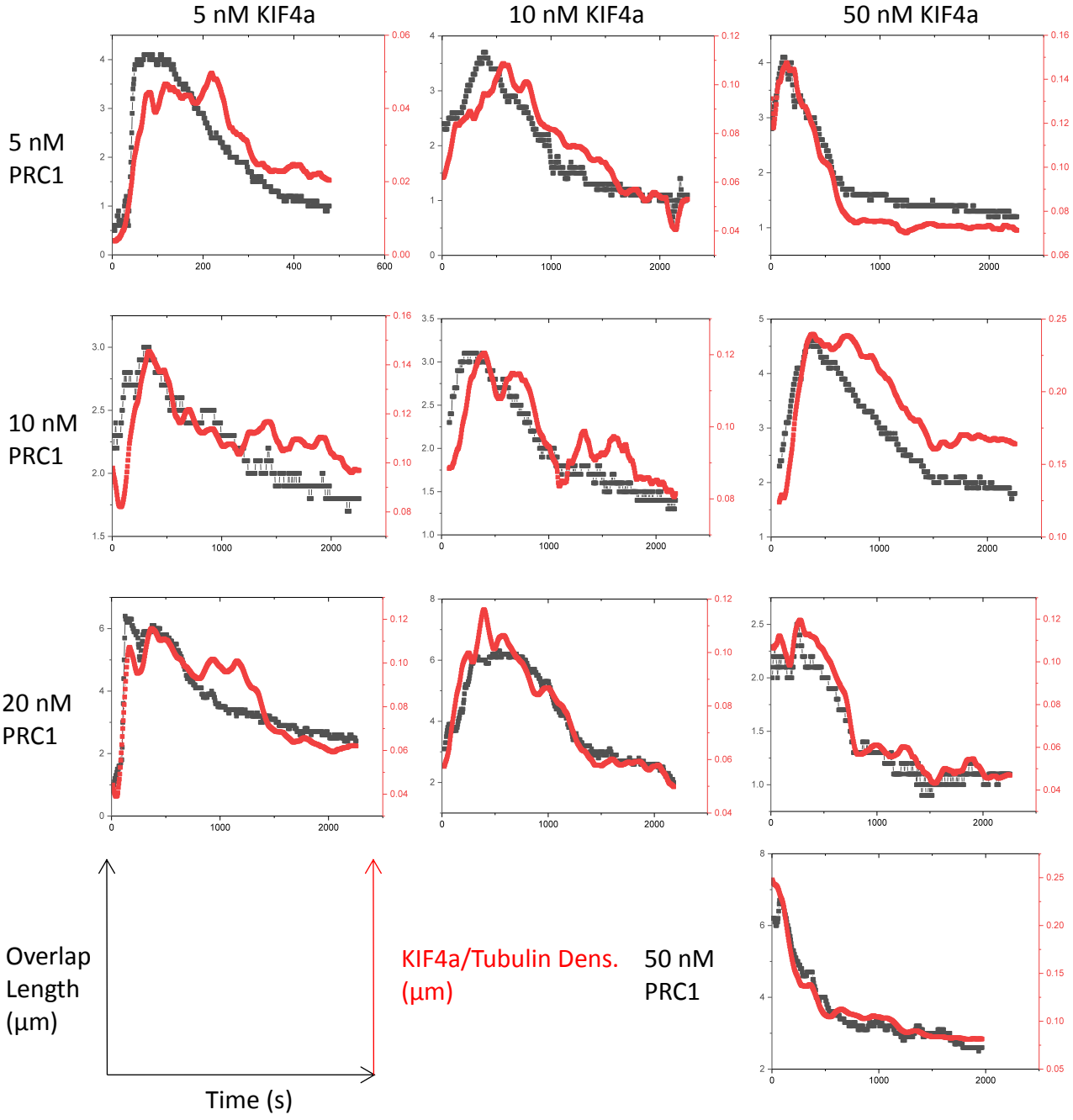

Figure 4.8: Line plots comparing overlap length and KIF4a/Tubulin density over time
Line plots showing how overlap length and KIF4a/Tubulin density changes over time. An example is shown from each concentration condition. Time (s) is along the X axis, with overlap length (µm) along the black Y axis, and KIF4a/Tubulin density (µm) along the red Y axis. Axis have been auto scaled in OriginPro2017 for comparison between overlap length and KIF4a/Tubulin density.

The evidence suggests that PRC1 is diluted by the increase in microtubule overlap at the start of the experiment, as existing microtubules grow, and more microtubules are nucleated. As already mentioned above, higher KIF4a concentrations, which reduce growth early on, could allow for more PRC1 in solution, which would result in more nucleation. Hence, there will always be a similar ratio between PRC1 and tubulin in the overlap, regardless of how the PRC1 and KIF4a concentrations are changed.

Unlike $PRC1_{Int}/Tub_{Int}$, $KIF4a_{Int}/MT_n$ tends to follow the overlap length over time (Fig 4.8). In some of the examples in Fig 4.8 it can be seen that there is a slight lag, where the peak KIF4a/MT follows slightly after the peak overlap length, all of which suggests that the overlap length has an effect on the $KIF4a_{Int}/MT_n$. $PRC1_{Int}/Tub_{Int}$ shows no correlation with overlap length during the time course of the experiment, which given that there is no correlation at the end, is not surprising. $KIF4a_{Int}/MT_n$ does, so why is there no correlation at the end of the experiment?

4.5 Discussion

A picture is beginning to emerge from the data, as to the mechanism of self-organisation in this system. The most intuitive explanation from looking at the qualitative data in the previous chapter is that there is a slide and brake mechanism, where KIF4a slides the overlaps apart, which compresses the PRC1 molecules, increasing frictional force. However, when we analyse the data more closely, we find that increasing KIF4a concentrations shrinks overlaps, but without increasing the density of PRC1 on the microtubules. In addition, when we analyse case studies across all conditions, the density of PRC1 on the microtubule begins much higher than at the end of the experiment, after antiparallel sliding has taken place; the opposite of what one might expect if a

compression mechanism were at work. On the contrary, the system appears, if anything, to relax towards the end point, as PRC1 overlap density and KIF4a/MT both decrease from their peak value in the experiment.

Based on the above evidence, I propose the following model for the self-organisation of anaphase mini spindles. Overlap lengths are set by having enough KIF4a at microtubule ends to stop the growth, but not enough to slide (Fig 4.9). The first part of this mechanism is the same as that proposed by Bieling et. al. for microtubule pairs. Short overlaps with less PRC1 will recruit less KIF4a, meaning the microtubule plus-ends are able to grow. As the overlap gets bigger, it is able to recruit more KIF4a to the point where microtubule plus-ends stop growing, giving a stable overlap. Increasing the KIF4a concentration in solution will increase the binding frequency for a given overlap length, and PRC1 density, meaning overlaps will stop growing faster. In addition to this, I propose that if overlaps

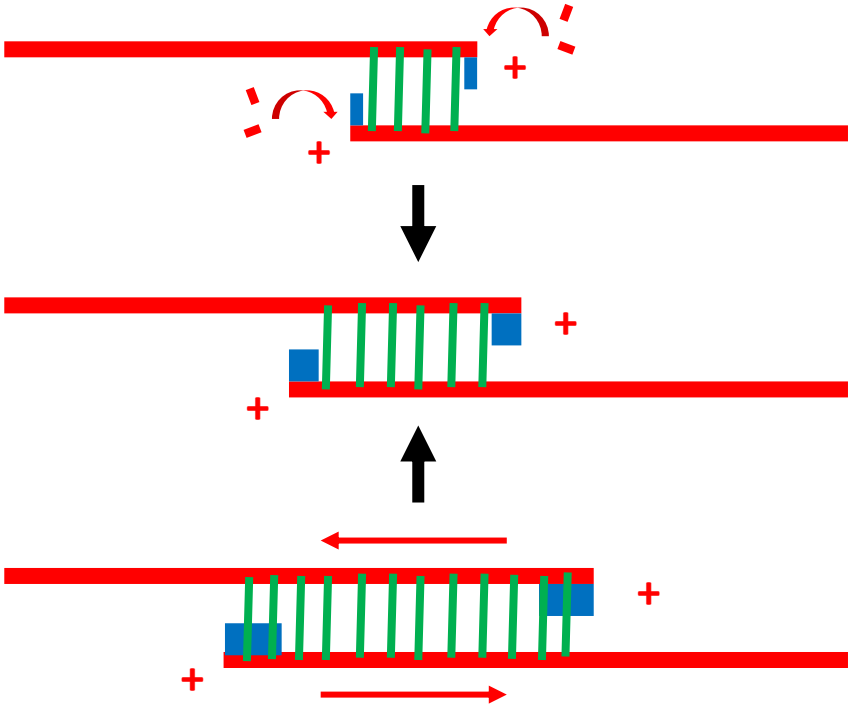

Figure 4.9: Schematic demonstrating the KIF4a steady state end caps mechanism
Short overlaps do not recruit enough KIF4a to microtubule growth, leading to overlap growth. Long overlaps recruit too much KIF4a leading to sliding and overlap shrinkage. (Red) microtubules; (Green) PRC1; (Blue) KIF4a

are too long, the KIF4a end cap will grow into the overlap, where enough KIF4a will interact with PRC1 for sliding to ensue (Fig 4.9).

In this model it is clear how increasing the KIF4a concentration would lead to smaller overlaps, but surely increasing the PRC1 concentration would increase the density of PRC1, increasing the recruitment of KIF4a, causing smaller overlaps, or overlaps of the same size, but with differing PRC1 densities. As mentioned above, however, because PRC1 is also a microtubule nucleating agent, rather than increasing PRC1 density in the overlap, you instead increase the number of microtubules, and hence overlaps. As the amount per microtubule is what is important for KIF4a's effect on overlap control, increasing the number of microtubules will effectively dilute the concentration of KIF4a in solution, leading to larger overlap lengths.

These experiments show that the mechanism of KIF4a steady state end caps can not only prevent microtubules growing too long, but can also rein in overgrown overlaps. Under the conditions of these experiments, where multiple fusion events cause overlaps to grow rapidly at the start of the experiment, the major contribution of the end caps mechanism is to shrink overgrown overlaps. This novel assay has also shown how this mechanism can work to organise bundles of microtubules, aligning their plus ends to form anaphase mini spindles, which reflect the basic structure of the central spindle in cells. In the overlaps, where the KIF4a and PRC1 are concentrated, it seems reasonable to think that some KIF4a molecules remain bound via PRC1 alone to the overlap, leaving their motor heads free to interact with microtubules from another mini-spindle. The plus end directed motion of KIF4a will naturally bring overlapping regions together, and these will be aligned by PRC1 crosslinking antiparallel overlaps together.

Recent and past works in cells have demonstrated the presence of a sliding force in the central spindle, but as yet, the candidate is unknown [122, 128]. This thesis clearly demonstrates that human KIF4a can function as an antiparallel sliding motor in the presence of PRC1. It seems reasonable to suggest that KIF4a should be considered as a potential provider of the mysterious sliding force observed in cells. Little attention has been given to the ability of central spindle overlaps to remain so aligned down the centre of the cell in wild type cells, even when being compressed by the ingressing furrow. This thesis shows how KIF4a and PRC1 can align overlaps, by a combination of sliding and cross-linking, and how this can adjust overlaps that are too long or too short. The absence of centralspindlin, or any other central spindle associated proteins, demonstrates that they are not essential to creating a central spindle-like architecture, despite being needed in cells to resist antagonistic forces [42, 116].

Chapter 5: Materials and Methods

5.1 Gel Electrophoresis

Gel electrophoresis was performed using NuPAGE 4-12% gradient gels (Invitrogen). Proteins were dissolved in NuPAGE LDS Sample Buffer (Invitrogen) diluted to 1x with MilliQ water, and heated at 97°C for 5 minutes. For protein test expressions, 1 mL of Insect cells were spun down at 650 x g for 10 minutes. After which they were lysed and resuspended by pipetting up and down in NuPAGE LDS Sample Buffer diluted to 1x concentration in PBS, and heated at 97°C for 5 minutes. Proteins were loaded onto gels alongside a Precision plus Protein Standards ladder (BioRad, 161-0377) for molecular weight comparisons. Gels were run in NuPAGE 1x MOPS SDS Running Buffer (Invitrogen). Gel staining for protein visualisation was performed by soaking gels in the following solutions:

1. Fixing Buffer: 40% Methanol (v/v), 10% Acetic Acid (v/v) in MilliQ water. Time: 1 h
2. Coomassie Stain: Bio-Safe Coomassie G-250 Stain (BioRad, 161-0786). Time: 1 h
3. Destain: MilliQ water. Time: 2 h

5.2 Protein Expression

The human KIF4a, PRC1 and CAMSAP3 used in this thesis were made recombinantly using insect SF21 cells as the expression system. I received 2nd generation baculoviruses containing the relevant expression sequence for the following proteins: full length KIF4a-mGFP-TEV-His, KIF4a-mBFP-TEV-His and His-TEV-PRC1-SNAP were received from

Dr. Franck Fourniol, and Strep-TEV-mCherry-CAMSAP3ΔN, a truncated construct consisting of amino acids 757-1276, was received from Dr. Johanna Roostalu.

40 mL of SF21 cells (0.6 x 10^6 cells/mL) were infected with 5 µL of 2nd generation baculovirus in Sf-900 III Serum Free Medium (Gibco). Cells were split down every 24 h. 3rd generation virus was collected 48 h after cells had stopped dividing by spinning the culture down at 650 x g for 10 minutes, and filter sterilising the supernatant using a 0.22 µm Stericup Filter (Merck). Small scale test expressions were performed using 3rd generation virus to determine optimum expression conditions. Typical final expression conditions were 1.5-2.5% virus (v/v), expressed from 48-72h. Conditions were selected for high multiplicity of infection, high protein expression and absence of protein degradation. Final expressions were always performed for 600 mL cell culture at 0.6 x 10^6 cells/mL. Cell pellets were spun down at 650 x g at 4 °C for 20 minutes, and after discarding the supernatant, frozen in liquid N_2. Frozen cell pellets were stored at -80 °C.

5.3 Protein Purification and Labelling

5.3.1 Purification of KIF4a-mGFP and KIF4a-mBFP

KIF4a constructs were expressed in the form KIF4a-Fluor-TEV-His. The following buffers were used in their purification:

Wash Buffer: 50 mM NaPi, 350 mM KCl, 2 mM imidazole, 1 mM $MgCl_2$, 1 mM EDTA, 10 mM β-mercaptoethanol, 0.2 mM ATP, 50 mM glutamate, 50 mM arginine, pH 7.5.

Elution Buffer: 50 mM NaPi, 350 mM KCl, 300 mM imidazole, 1 mM $MgCl_2$, 1 mM EDTA, 10 mM β-mercaptoethanol, 0.2 mM ATP, 50 mM glutamate, 50 mM arginine, pH 7.5.

Gel Filtration Buffer: 50 mM NaPi, 350 mM KCl, 1 mM $MgCl_2$, 1 mM EDTA, 2 mM DTT, 0.2 mM ATP, 50 mM glutamate, 50 mM arginine, pH 7.5.

Cell pellets were lysed on ice by dounce homogenisation in 50 mL Wash Buffer supplemented with 2 x cOmplete EDTA-free protease inhibitor tablets (Roche). Cell lysate was then span down at 50,000 rpm for 30 minutes at 4 °C in a Ti70 rotor (BeckmanCoulter). Lysate supernatant was incubated for 2 h on a spinning wheel at 4 °C with 1.5 g Ni-TED resin, which had been washed 3 x with wash buffer prior to addition of the supernatant. Resin was loaded into a 4 mL gravity column, and washed with 80 mL wash buffer at 0.5 mL/min. Bound His-tagged protein was eluted into 0.5 mL fractions by flowing through elution buffer (0.5 mL/min). Protein containing fractions were determined by eye for GFP labelled KIF4a, or Bradford assay for BFP labelled KIF4a. Fractions were pooled and desalted using PD-10 columns (GE Healthcare) into Gel Filtration Buffer. The His tag was cleaved overnight in Gel Filtration Buffer at 4 °C by adding TEV protease (1 mg TEV/ 30 mg His-tagged protein). Protein cleavage mixture was flown over Ni-TED resin, and the protein containing fractions of the flow through were concentrated using a Vivaspin concentrator (Sartorius; VS15RH21) until the volume was 500 μL or the protein concentration reached 5 mg/mL. Concentrated solution was spun down at 80,000 rpm for 15 min in a TLA-120 rotor (BeckmanCoulter) and gel filtered using a superose 6 10/30 column (GE Healthcare) equilibrated with gel filtration buffer (Fig 5.1A and 5.1C). Peak protein fractions were pooled, and concentrated to a concentration >1.25 mg/mL, as measured using a NanoDrop ND-1000

Spectrophotometer. Glycerol was added to a final concentration of 20% (v/v), and the final mix was spun down at 80,000 rpm for 15 min in a TLA-120 rotor (BeckmanCoulter). Supernatant was aliquoted into 5 μL aliquots and frozen in liquid N_2. Protein was stored

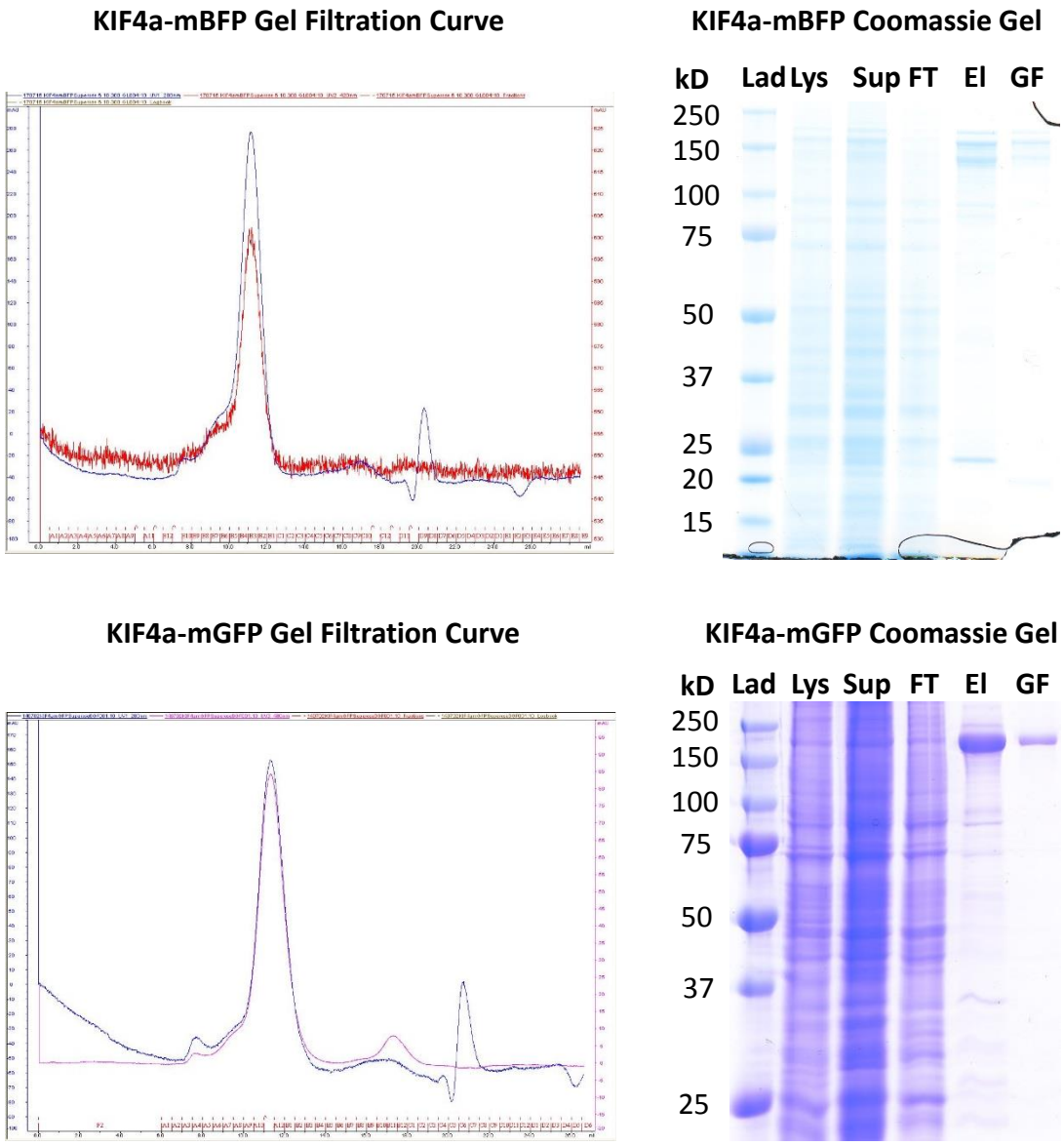

Figure 5.1: Analysis of the purification of KIF4amBFP and KIF4amGFP
(A) Gel filtration curve of KIF4a-mBFP, showing absorbance at 280 nm (blue) and 420 nm (red). (B) Coomassie gel recording the purification of KIF4a-mBFP showing protein standard (Lad), cell lysate (Lys), supernatant post first centrifugation (Sup), flow through i.e. the solution discarded after binding to Ni-TED resin (FT), pooled fractions eluted from Ni-TED resin and a sample taken post gel filtration (GF). (C) Gel filtration curve of KIF4a-mBFP, showing absorbance at 280 nm (blue) and 480 nm (pink). (D) As (B), but for KIF4a-mGFP.

in liquid N_2. Purity was assessed by gel electrophoresis (Fig 5.1B, Fig5.1D and Fig 2.2). Yields were ~1.5 mg of protein from a 600 mL insect cell pellet.

5.3.2 Purification of PRC1-SNAP

PRC1 was expressed in the form His-TEV-PRC1-SNAP. The following buffers were used in its purification:

Wash Buffer: 50 mM NaPi, 500 mM KCl, 2 mM imidazole, 3 mM EDTA, 10 mM β-mercaptoethanol, pH 7.5.

Elution Buffer: 50 mM NaPi, 500 mM KCl, 400 mM imidazole, 3 mM EDTA, 10 mM β-mercaptoethanol, pH 7.5.

Gel Filtration Buffer: 50 mM NaPi, 500 mM KCl, 3 mM EDTA, 2 mM DTT, pH 7.5.

Cell pellets were lysed on ice by dounce homogenisation in 50 mL Wash Buffer supplemented with 2 x cOmplete EDTA-free protease inhibitor tablets (Roche). Cell lysate was then spun down at 50,000 rpm for 30 minutes at 4 °C in a Ti70 rotor (BeckmanCoulter). Lysate supernatant was incubated for 2 h on a spinning wheel at 4 °C with 1.25 g Ni-TED resin, which had been washed 3 x with wash buffer prior to addition of the supernatant. Resin was loaded into a 4 mL gravity column, and washed with 80 mL wash buffer at 0.5 mL/min. Bound His-tagged protein was eluted into 0.5 mL fractions by flowing through elution buffer (0.5 mL/min). Protein containing fractions were determined by Bradford assay. Fractions were pooled and desalted using PD-10 columns (GE Healthcare) into Gel Filtration Buffer. His tag cleavage and SNAP tag labelling were performed simultaneously, overnight at 4 °C in Gel Filtration Buffer. The His tag was cleaved by adding TEV protease (1 mg TEV/ 30 mg His-tagged protein). SNAP tag

labelling was achieved by adding SNAP-Surface Alexa Fluor- 546 or SNAP-Surface Atto Fluor- 488 (NEB) dissolved in DMSO, so as to have a 2:1 ratio of Label:PRC1-SNAP. Protein cleavage mixture was flown over Ni-TED resin, and the protein containing fractions of the flow through were concentrated using a Vivaspin concentrator (Sartorius; VS15RH21) until the volume was 500 µL. Concentrated solution was spun down at 80,000 rpm for 15 min in a TLA-120 rotor (BeckmanCoulter) and gel filtered using a superose 6 10/30 column (GE Healthcare) equilibrated with gel filtration buffer (Fig 5.2A). Peak protein fractions were pooled, and concentrated to a concentration of ~1 mg/mL, as measured using a NanoDrop ND-1000 Spectrophotometer. The final mix was spun down at 80,000 rpm for 15 min in a TLA-120 rotor (BeckmanCoulter). Supernatant was aliquoted into 5 µL aliquots and frozen in liquid N_2. Protein was stored in liquid N_2.

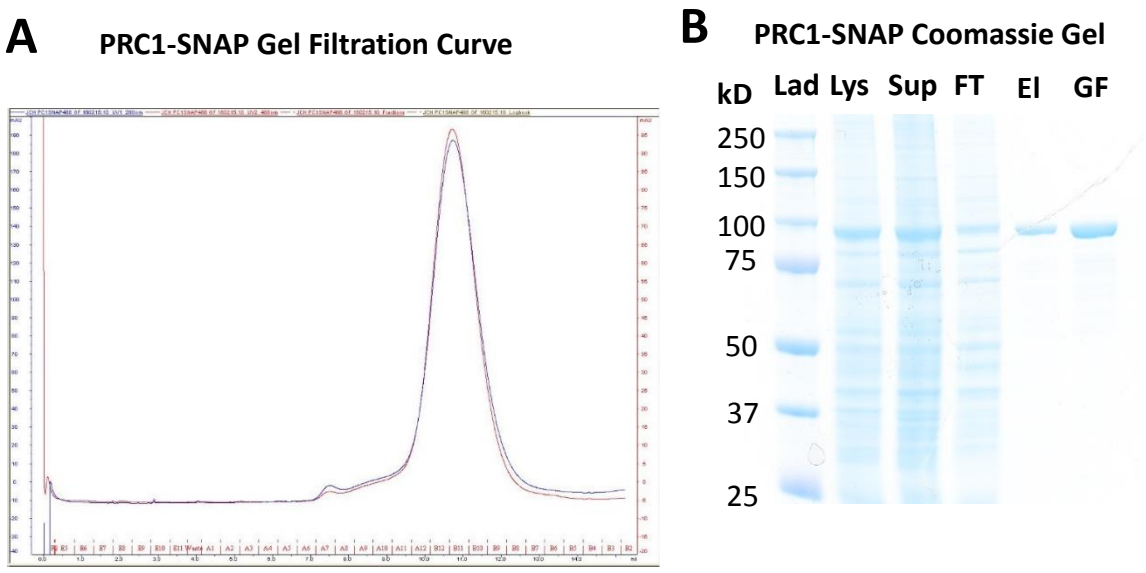

Fig 5.2: Analysis of the purification of PRC1-SNAP
(A) Gel filtration curve of PRC1-SNAP-Atto488, showing absorbance at 280 nm (blue) and 480 nm (red). (B) Coomassie gel recording the purification of PRC1-SNAP showing protein standard (Lad), cell lysate (Lys), supernatant post first centrifugation (Sup), flow through i.e. the solution discarded after binding to Ni-TED resin (FT) and pooled fractions eluted from Ni-TED resin.

Purity was assessed by gel electrophoresis (Fig 5.2B and Fig 2.2). Yields were ~1.5 mg of protein from a 600 mL insect cell pellet.

5.3.3 Purification of mCherry-CAMSAP3ΔN

mCherry-CAMSAP3ΔN (amino acids 757-1276 of full length CAMSAP3) was expressed in the form Strep-TEV-mCherry-CAMSAP3ΔN. The following buffers were used in its purification:

Wash Buffer: 50 mM HEPES, 300 mM KCl, 5 mM $MgCl_2$, 1 mM EDTA, 5 mM β-mercaptoethanol, pH 8.

Elution Buffer: 50 mM HEPES, 300 mM KCl, 2 mM $MgCl_2$, 1 mM EDTA, 5 mM β-mercaptoethanol, 2.5 mM D-desthiobiotin, 50 mM glutamate, 50 mM arginine, pH 7.5.

Gel Filtration Buffer: 50 mM HEPES, 300 mM KCl, 2 mM $MgCl_2$, 1 mM EDTA, 5 mM β-mercaptoethanol, 50 mM glutamate, 50 mM arginine, 250 mM sucrose, pH 7.5.

Cell pellets were lysed on ice by dounce homogenisation in 40 mL Wash Buffer supplemented with 2 x cOmplete EDTA-free protease inhibitor tablets (Roche), 5 mg DnaseI and 10 mg avidin. Cell lysate was then spun down at 50,000 rpm for 45 minutes at 4 °C in a Ti70 rotor (BeckmanCoulter). Lysate supernatant was run over a 5 mL StreptActin resin column (HP), which had been equilibrated with wash buffer. Column was washed with 10 mL of Wash Buffer. Bound Strep-tagged protein was eluted into 0.5 mL fractions by flowing through elution buffer (0.5 mL/min). Protein containing fractions were determined by Bradford assay and pooled. The Strep tag was cleaved overnight in Gel Filtration Buffer at 4 °C by adding TEV protease (1 mg TEV/ 30 mg Strep-tagged protein). Elution Buffer was exchanged for Gel Filtration buffer using 2 x HiPrep 26/10

Desalting columns (GE Healthcare). Protein containing fractions were pooled and flown over StreptActin resin column, and the protein containing fractions of the flow through were concentrated using a Vivaspin concentrator (Sartorius; VS15RH21) until the volume was 500 µL. Concentrated solution was spun down at 80,000 rpm for 15 min in a TLA-120 rotor (BeckmanCoulter), and gel filtered using a superose 6 10/30 column (GE Healthcare) equilibrated with gel filtration buffer (Fig 5.3A). Peak protein fractions were pooled, and concentrated to a concentration of ~1 mg/mL, as measured using a NanoDrop ND-1000 Spectrophotometer. The final mix was spun down at 80,000 rpm for 15 min in a TLA-120 rotor (BeckmanCoulter). Supernatant was aliquoted into 5 µL aliquots and frozen in liquid N_2. Protein was stored in liquid N_2. Purity was assessed by gel

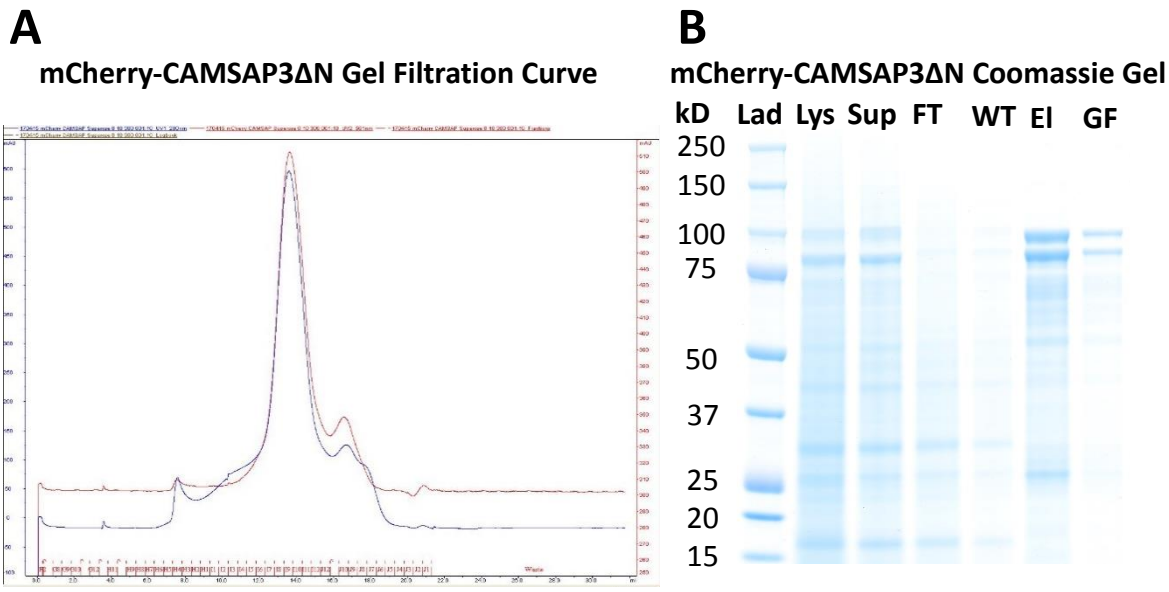

Figure 5.3: Analysis of the purification of mCherry-CAMSAP3ΔN
(A) Gel filtration curve of mCherry-CAMSAP3ΔN, showing absorbance at 280 nm (blue) and 480 nm (red). (B) Coomassie gel recording the purification of PRC1-SNAP showing protein standard (Lad), cell lysate (Lys), supernatant post first centrifugation (Sup), flow through i.e. the solution discarded after binding to Ni-TED resin (FT), wash through i.e. wash buffer, which has passed through the protein loaded column (WT), pooled fractions eluted from StrepActin resin (El) and a sample taken post gel filtration (GF).

electrophoresis (Fig 5.3B and Fig 2.2). Yields were ~1.5 mg of protein from a 600 mL insect cell pellet.

5.3.4 Tubulin Purification and Labelling

Pig brain tubulin was purified as described by Castoldi et. al. [138]. Covalent labelling of tubulin with NHS-Atto488 (Sigma Aldrich), NHS-Alexa647N (Sigma Aldrich) and NHS-biotin (Pierce) was performed as described by Hyman et. al. [139].

5.4 Slide Preparation and Surface Chemistry

5.4.1 Covalent Passivation of Coverslips with PEG and Biotin-PEG

22 x 22 mm Coverslips (#1.5) are marked to decipher one side from another. Coverslips are then loaded in porcelain racks and sonicated in 3 M NaOH for 30 min. Coverslips are rinsed with MilliQ water and placed in an empty 1 L beaker. Piranha solution (180 mL 95-97% H_2SO_4 + 120 mL 30% H_2O_2) is poured over them, followed by sonication for 45 min. Coverslips are washed by submerging in 4 x 1 L MilliQ water and spin dried. Half of the coverslips are placed marked side up in large, clean, dry petri dishes, and 2-3 drops of GOPTS (Sigma Aldrich:440167) are added. The rest of the coverslips are placed marked side down on top to create a GOPTS sandwich, before they are placed in an oven at 75 °C for 30 min. Coverslips are taken out and left to cool for 15 min before being separated and placed in porcelain racks in acetone. After 15 min these are transferred into a second acetone beaker. During that 15 min 0.1 g biotin-CONH-PEG-NH_2 (Rapp Polymere:133000-25-20) and 1 g HO-PEG-NH_2 (Rapp Polymere:10300-20) are combined at room temperature, and left rotating on rollers. Slides are spin dried and placed between lens cleaning tissue. Half of the coverslips are placed marked side up in large, clean, dry petri dishes, and ~50 mg of PEG mix is added on top. The rest of the

coverslips are placed marked side down on top to create a PEG sandwich, before they are placed in an oven at 75 °C. Once the PEG has melted, bubbles are removed by gently pressing down on the sandwiches with forceps. Sandwiches are incubated overnight at 75 °C. Coverslips are peeled apart with a pair of razor blades on a magnetic hot plate and tossed in MilliQ water, after which they are sonicated for 30 min. Coverslips are continuously washed with MilliQ water until there ceases to be foam. Slides are spin dried and stored between lens cleaning tissue at 4 °C for a maximum of 2 months.

5.4.2 Preparation of Flow Cells

Slides are sonicated first in 3 M NaOH for 30 min, followed by sonication in MilliQ water for 30 min. Slides are dried with N_2 and placed between lens cleaning tissue. Two strips of double-sided tape (~2 cm) are placed ~5 mm apart parallel to one another on each coverslip, so as to create an open channel. 10 μL of 2 mg/mL PLL-PEG is added in between each pair of strips, and spread using a pipette tip so it covers the entire channel, as well as the area around the entry and exit points. Slides are left for 20 minutes, or until the PLL-PEG has dried. Coverslips, as prepared in 5.4.1, are cut into quarters using a glass cutter. Open channels on the slides are rinsed with MilliQ water and dried with N_2. Backs are peeled off the double sided tapes, and coverslip quarters are placed functional side down, creating a closed channel. Channels are sealed by gently pressing down on the edges of the coverslip with forceps to complete the flow cell. Flow cells are stored at 4°C and used within 48 h.

5.5 Preparation of GMPCPP Seeds

For the preparation of short GMPCPP seeds (Figs 2.3, 2.4, 2.5, 2.7 and 2.8) 60 µL of the following solution was prepared in BRB80 (80 mM PIPES, 1 mM $MgCl_2$, 1 mM EGTA, pH 6.8) on ice:

12 µM Alexa647-Tubulin (Labelling ratio = 0.25), 6 µM Biotin-Tubulin, 0.5 µM GMPCPP.

Once mixed, the solution was kept wrapped in foil on ice for 5 min before being transferred to a preheated water bath at 37 °C for 1 h. 400 µL BRB80, prewarmed to 37 °C, was added to the solution, and the reaction spun down at 13,000 rpm for 5 min. The supernatant was discarded, and 510 µL fresh, prewarmed BRB80 was added, and the reaction spun down again at 13,000 rpm for 5 min. Supernatant was discarded, and pellet was resuspended in 50 µL prewarmed BRB80 using a cut-off pipette tip. Seed solution was kept wrapped in foil at room temperature. Seeds were used on day of production.

For the preparation of long GMPCPP seeds (Fig 2.6) 300 µL of the following solution was prepared in BRB80 (80 mM PIPES, 1 mM $MgCl_2$, 1 mM EGTA, pH 6.8) on ice:

1.8 µM Alexa647-Tubulin (Labelling ratio = 0.1), 0.5 µM Biotin-Tubulin, 0.5 µM GMPCPP.

Once mixed, the solution was kept wrapped in foil on ice for 5 min before being transferred to a preheated water bath at 37 °C for 2 h. 400 µL BRB80, prewarmed to 37 °C, was added to the solution, and the reaction spun down at 13,000 rpm for 10 min. The supernatant was discarded, and the pellet was resuspended in 30 µL prewarmed BRB80 using a cut-off pipette tip. Seed solution was kept wrapped in foil at room

temperature, and left overnight to encourage microtubules to fuse. Seeds were used the next day.

5.6 *In vitro* Microscopy: Buffers

Pre-buffer = buffer made prior to experiment.

Final = final buffer used in the experiments. References to buffers in the results part of this thesis refer exclusively to the final buffer.

High Salt Buffer (HSB):

80 mM PIPES, 85 mM KCl, 85 mM KOAc, 4.5 mM $MgCl_2$, 1 mM EGTA, 0.005% Brij-35, 10 mM β-mercaptoethanol, 33 mM glucose, pH 6.8. (Pre-buffer)

+ 1 mg/mL glucose oxidase, 0.5 mg/mL catalase, 2 mM ATP, 1 mM GTP (Final)

Mid Salt Buffer (MSB):

80 mM PIPES, 85 mM KOAc, 4.5 mM $MgCl_2$, 1 mM EGTA, 0.005% Brij-35, 10 mM β-mercaptoethanol, 33 mM glucose, pH 6.8. (Pre-buffer)

+ 1 mg/mL glucose oxidase, 0.5 mg/mL catalase, 2 mM ATP, 1 mM GTP (Final)

Low Salt Buffer (LSB):

80 mM PIPES, 4.5 mM $MgCl_2$, 1 mM EGTA, 71.5 mM β-mercaptoethanol, 33 mM glucose, 5% sucrose (w/v), pH 6.8. (Pre-buffer)

+ 1 mg/mL glucose oxidase, 0.5 mg/mL catalase, 2 mM ATP, 1 mM GTP (Final)

5.7 *In vitro* Microscopy: Assays

All TIRF microscopy experiments were performed on a custom TIRFM microscope (Cairn Research, Faversham, UK) based on a Nikon Ti-E frame with a 100x 1.49 N.A. objective lens. The sample was excited using a 360°TIRF illumination. Images were acquired with an Andor iXon Ultra 888 EMCCD camera. All experiments presented in this thesis have been duplicated reproducibly.

5.7.1 Dynamic Seed Assays (Fig 2.7 and 2.8)

50 μL 5% Pluronic was flown through the flow cell, and left for 10 min at room temperature. 2 x 50 μL Pre-buffer (see above) supplemented with 0.2 mg/mL κ-casein was flown through the flow cell at room temperature. The slide was transferred onto ice, and 50 μL Pre-buffer supplemented with 0.2 mg/mL κ-casein and Neutravidin 0.05 mg/mL was flown through the flow cell, and left for 3 min on ice. 1 μL short GMPCPP seed solution was diluted in 100 μL room temperature Pre-buffer, and wrapped in foil at room temperature. 2 x 50 μL Pre-buffer was flown through the flow cell at room temperature, followed by 50 μL diluted seed solution. Flow cell was left at room temperature for 3 min. Final buffer was mixed on ice by combining 50 μL 2 x Pre-buffer with BRB80, ATP, GTP, oxygen scavengers and proteins to give 100 μL final buffer + protein (PRC1, KIF4a and tubulin). The same volume of protein was added each time. Protein concentrations were altered by predilution in the appropriate storage (i.e. gel filtration) buffer (see above). Final labelling ratio for tubulin was always 0.1. After seeds had been left to fix for 3 min at room temperature, 2 x 50 μL Pre-buffer was flown through the flow cell at room temperature, followed by the final reaction mix, and the flow cell was sealed with nail varnish (Barry M). Imaging began ~2 min after slide was loaded

onto the TIRF microscope. The microscope chamber was kept at 30 °C. Images were captured every 4.5 s for a total time of 38 minutes.

5.7.2 Non-Dynamic Seed Assay (Fig 2.3, 2.4 and 2.5)

Non-dynamic seed assays were performed as for dynamic seed assays, with the exception that no tubulin was added to the final reaction mix, and imaging was conducted as reported in Subramanian et. al., beginning imaging after 10 min at 30 °C in the dark.

5.7.3 Single Molecule Assay

Single molecule assays were performed as for dynamic seed assays, with the exception that no tubulin was added to the final reaction mix, and long, as opposed to short, GMPCPP seeds were used. Images were captured every 100 ms for (Fig 2.6A) and every 200 ms for (Fig 2.6B) for a total time of 1.67 min.

5.7.4 Self-Organisation Assay (Figures from chapter 3 onwards)

50 μL 5% Pluronic was flown through the flow cell, and left for 10 min at room temperature. 2 x 50 μL Pre-buffer (see above) supplemented with 0.2 mg/mL κ-casein was flown through the flow cell, and the flow cell was transferred onto ice for 3 min. Final buffer was mixed on ice by combining 50 μL 2 x Pre-buffer with BRB80, ATP, GTP, oxygen scavengers and proteins to give 100 μL final buffer + protein (PRC1, KIF4a and tubulin). The same volume of protein was added each time. Protein concentrations were altered by predilution in the appropriate storage (i.e. gel filtration) buffer (see above). Final labelling ratio for tubulin was always 0.1. After 3 min on ice, 2 x 50 μL Pre-buffer was flown through the flow cell at room temperature, followed by the final reaction mix, and the flow cell was sealed with nail varnish (Barry M). Imaging began ~2 min

after slide was loaded onto the TIRF microscope, or until an object appeared in the TIRF field that could be focussed upon. The microscope chamber was kept at 30 °C. Images were captured every 4.5 s for a total time of 38 minutes.

5.7.5 FRAP Experiments

FRAP experiments were performed on a 3i Marianas spinning disk confocal microscope comprising a Yokogawa CSU M1 spinning disk on a Zeiss Axio Observer Z1 with automated FRAP unit. The microscope chamber was kept at 30 °C. Images were captured using a 100x oil objective. Samples were prepared as for the self-organisation assays above. Frames were recorded every 4.5 s for 38 min. Bleach sites were created in the tubulin channel 25 min after the start of imaging.

5.8 Kymograph Tracking

Kymograph generation from the tracking of moving mini-spindles was done using an imageJ macro developed by Dr. Nicholas Cade: 'JH Tracking Kymo'. The macro follows the following series:

1) Movies are loaded or selected from open files. The user specifies the line length for the kymograph (250 μm as standard), line width to average over (25 μm as standard), and minimum number of frames in kymograph that particle is tracked over (100 frames, so 450 s, as standard).

2) MT background can be subtracted if required: 250 pixel rolling ball: https://imagej.net/Rolling_Ball_Background_Subtraction

Background was always subtracted at this stage.

3) The channel to track is chosen. This was always the PRC1 channel.

The tracking channel is duplicated, a 1 pixel Gaussian blur is applied (to reduce effects of noise), and the user manually adjusts the intensity threshold to identify overlap regions.

4) The 'Analyse Particles' plugin runs to identify particles (overlap region) in each frame.

5) The 'DropletTracker2' plugin links particles in between each frame, and the centre co-ordinates and orientation of major axis are saved.

6) The particle is rejected if it is tracked for fewer than the specified number of frames (100 frames as standard) or it is too close to edge of the image.

7) For each remaining particle, co-ordinates and orientations are used to obtain line profiles for each frame, and for each fluorescence channel. A composite kymograph is generated.

8) An overview movie showing tracked particles can be saved, along with the generated kymographs.

5.9 Data Analysis

5.9.1 Kymograph Analysis

Kymograph analysis to acquire overlap intensity profiles for each timepoint was done using an imageJ macro developed by Dr. Nicholas Cade: 'Kymo profile plot'. The macro follows the following series:

1) The user selects an open kymograph image to analyse.

2) The user selects a rectangular background region. For each channel, the mean values of the pixel intensities in the rectangle are used as the background and subtracted.

3) Overlap width analysis (Fig 5.4A):

The user specifies the maximum extent of the area of the kymograph to be analysed. This is to allow for the exclusion of events at the edge of the kymograph image, which may

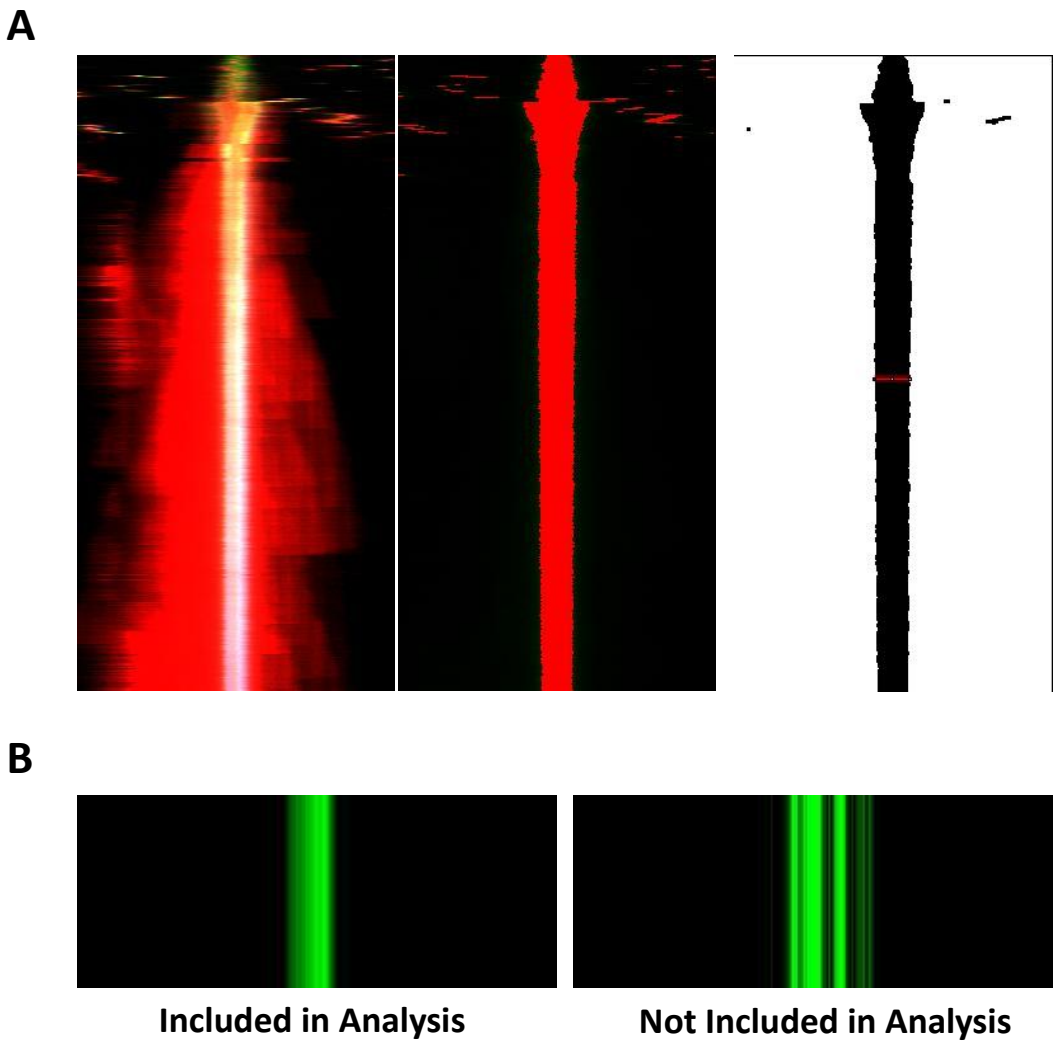

Figure 5.4: Example images taken from data measurement process
(A) Images of a kymograph being measured to give quantities for protein intensities and overlap length. Left shows the raw data, middle the threshold, and right the scanning. (B) Two examples of faux kymographs generated from end point data. The right example is not included in the data analysis, as it shows multiple unfused overlaps.

confuse the software. For each channel, a threshold, described in imageJ as ‘Minimum’, is automatically calculated. Minimum gives a threshold roughly corresponding to a median ‘half’ width of the overlap intensity peak. The user can tweak thresholds as necessary. A binary mask image is then created and despeckled. The ‘EdgeFitter’ plugin runs to determine the x-axis width of the threshold region (i.e. length of overlap). The total pixel intensity along that length is measured for all channels.

5.9.2 End Point Analysis

A modified version of JH Tracking Kymo was used to analyse end point data. This macro produced faux kymographs made of repeats of the one timepoint (Fig 5.4B). For each channel, a threshold, described in imageJ as ‘Moments’, is automatically calculated. For details of Moments thresholding see reference [140]. Lines were drawn manually on these thresholded images to determine the position of the overlap. ~20% of overlaps measured showed more than one clear overlapping zone, and these were not included in the analysis. It is expected that some overlaps will fail to fuse due to steric effects, which were made evident in chapter 3, as microtubule buckling was seen to occur in some instances. In all cases, overlaps were determined using the PRC1 channel.

Each condition was repeated twice for end point analysis. [Table 5.1] lists the number of events included in the end point analysis for each condition.

Table 5.1: Table presenting the number of events included in end point analysis for each concentration condition.

KIF4a Conc./ nM	PRC1 Conc./ nM	N
5	5	124
5	10	93
5	20	152
10	5	144
10	10	157
10	20	120
50	5	115
50	10	124
50	20	145
50	50	143

Variables derived from directly measured variables, such as intensity ratios, were calculated for each overlap individually, and the mean value was calculated as a mean of these individual values. Correlation coefficients were calculated using the built in function in OriginPro2017.

5.9.3 Measuring Microtubule Growth Rates and KIF4a Run Velocities

Microtubule growth rates and KIF4a run velocities were measured directly from kymographs generated using the built in Reslice function in ImageJ. Lines were drawn manually along growing plus ends for microtubule growth rates, and along tracks for KIF4a run velocities. Values were calculated from the slope of the line.

5.8 General Computer Software

Image processing and analysis was performed in ImageJ (Fiji). Quantitative analysis and graph production was performed using a combination of OriginPro2017, and Microsoft Excel. SlideBook and Metamorph were used as microscope control software for confocal and TIRF microscopes respectively. Word processing was performed using Microsoft Word. Figures were created and arranged using Adobe Illustrator, Adobe Photoshop and Microsoft PowerPoint.

Chapter 6: Future Directions

Now I have a reconstituted central spindle, what questions remain unanswered? The minus-ends in my system are untethered, and unaligned. This makes it easier in theory for the plus-ends to align, as microtubules can be slid freely and independently over one another. This is arguably also true of the central spindle in late anaphase/telophase cells [114]. Early anaphase cells, however, have at least some microtubules tethered to poles, or to other microtubules via the augmin complex [104]. It is not clear how my *in vitro* system would respond to organised minus-ends. To explore this further, one could add artificial centrosomes to the system [141], or a kinesin-14 capable of forming asters with radial plus-ends [74, 109]. Kinesin-14, and the organisation of minus-ends, has been linked to the structural integrity of the central spindle in cells [142]. It is clear from Fig 3.16 that KIF4a and PRC1 can buckle microtubules, and so one might expect a change in the geometry of the spindle when minus-ends are focussed.

Evidence presented in this thesis suggests that KIF4a requires PRC1 to crosslink and slide microtubules. Evidence from the literature suggests that the C-terminal, PRC1-binding, domain of KIF4a is not necessary for suppressing microtubule dynamics [58, 79]. Together these suggest that we may be able to decouple the sliding from the plus-end dynamic suppression functionalities. My *in vitro* reconstitution could act as a testing ground for KIF4a truncations and mutations, which could lead to a better understanding of how KIF4a structure translates into function.

Now I have a minimal system, I can begin adding components to see what will result. My proposed model suggests that, as seen in the literature, human PRC1 does not act as a significant brake against antiparallel sliding [99]. If PRC1 does not act like a brake under

my conditions, then addition of a kinesin-5, such as EG5, should slide apart the spindles, and try to form asters. Will it succeed, or will the end-caps mechanism, which relies on KIF4a transporting PRC1 to plus-end, keep PRC1 at plus-ends even in the absence of overlaps, and therefore distort the asters?

The interaction between the human centralspindlin and PRC1 has not been as well studied as that of the *C. elegans* proteins [42, 116, 117]. Addition of human centralspindlin to my system may result in a decrease in sliding velocity, owing to its reputation as a sliding brake. Will the nature of centralspindlin bundling look different to PRC1 bundling? Will having both antiparallel bundlers present affect the size or structure of mini-spindles?

An alternative addition to the assay would be a confinement. HeLa cells are ~20 μm in diameter, similar to the size of the mini-spindles in these experiments, but many mini-spindles still grow larger than this. Will mini-spindles be able to form in an artificial droplet, and what effect will confinement have on their organisation? Aster formation has been seen to be limited by confinements much larger than HeLa cells, suggesting the cell must have mechanisms in place that allow for asters to form in such small confinements [109, 110]. Will the same be true for mini-spindles?

These are just some of the directions in which one could go with this novel *in vitro* system. It is this author's hope that others will be able to use the evidence presented in this thesis to expand further our knowledge of the molecular mechanisms essential to life.

Appendix 1

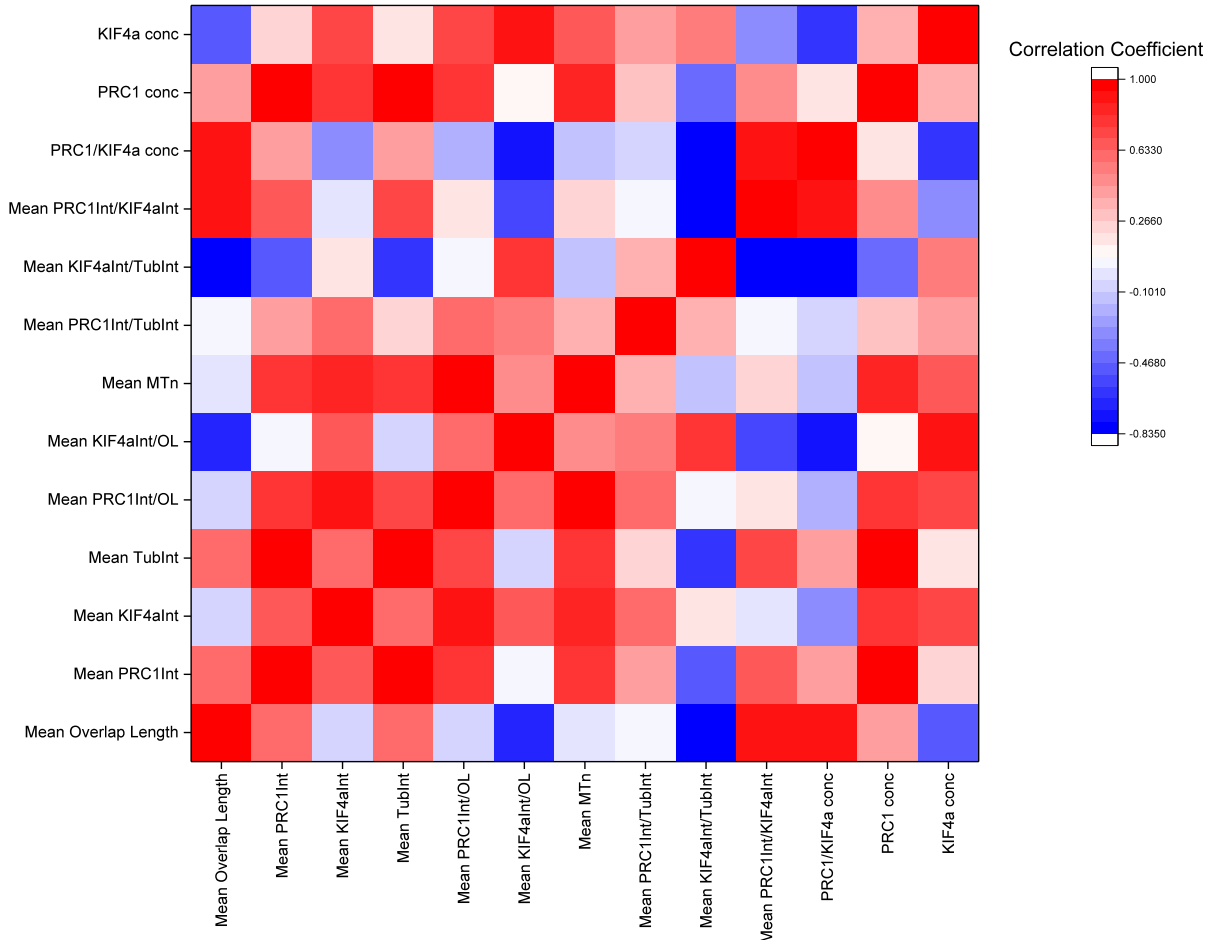

Figure A1: Heatmap of correlation coefficients comparing different variables

Appendix 2

Table A2.1: Table presenting mean values for different protein concentration conditions comparing maximum and end point (EP) values of $PRC1_{Int}/Tub_{Int}$ taken from kymograph data with non-illuminated end point values.

Concentration Condition	Mean $PRC1_{Int}/Tub_{Int}$ Non -Illuminated EP	Mean $PRC1_{Int}/Tub_{Int}$ Illuminated EP	Max $PRC1_{Int}/Tub_{Int}$ Illuminated
K5 P5	0.098	0.053	0.333
K5 P10	0.100	0.083	0.406
K5 P20	0.128	0.066	0.487
K10 P5	0.102	0.062	0.386
K10 P10	0.155	0.052	0.359
K10 P20	0.164	0.082	0.642
K50 P5	0.138	0.050	0.372
K50 P10	0.165	0.073	0.210
K50 P20	0.124	0.082	0.327
K50 P50	0.144	0.063	0.281

Table A2.2: Table presenting mean values for different protein concentration conditions comparing maximum and end point (EP) values of $PRC1_{Int}$ taken from kymograph data with non-illuminated end point values.

Concentration Condition	Mean $PRC1_{Int}$ Non - Illuminated EP	Mean $PRC1_{Int}$ Illuminated EP	Max $PRC1_{Int}$ Illuminated
K5 P5	22454	14494	54947
K5 P10	39045	23243	54561
K5 P20	91838	31438	151945
K10 P5	23011	6735	37275
K10 P10	45148	18133	66632
K10 P20	72003	34578	122034
K50 P5	31641	13729	49556
K50 P10	45905	19370	62295
K50 P20	47687	22304	93438
K50 P50	143524	63460	222916

Reference List

1. Mickolajczyk, K.J. & Hancock, W.O. Kinesin Processivity Is Determined by a Kinetic Race from a Vulnerable One-Head-Bound State. *Biophys J* **112**, 2615-2623 (2017).

2. Roostalu, J. & Surrey, T. Microtubule nucleation: beyond the template. *Nat Rev Mol Cell Biol* (2017).

3. Uehara, R., Tsukada, Y., Kamasaki, T., Poser, I., Yoda, K., Gerlich, D.W. & Goshima, G. Aurora B and Kif2A control microtubule length for assembly of a functional central spindle during anaphase. *J Cell Biol* **202**, 623-636 (2013).

4. Alberts, B., Johnson, A., Lewis, J., Raff, M., Roberts, K. & Walter, P. *Molecular Biology of the Cell* Edn. 4th. (Garland Science, 2002).

5. Paz, J. & Luders, J. Microtubule-Organizing Centers: Towards a Minimal Parts List. *Trends Cell Biol* (2017).

6. Tanenbaum, M.E. & Medema, R.H. Mechanisms of centrosome separation and bipolar spindle assembly. *Dev Cell* **19**, 797-806 (2010).

7. Kollman, J.M., Merdes, A., Mourey, L. & Agard, D.A. Microtubule nucleation by gamma-tubulin complexes. *Nat Rev Mol Cell Biol* **12**, 709-721 (2011).

8. Ohkura, H. Meiosis: an overview of key differences from mitosis. *Cold Spring Harb Perspect Biol* **7** (2015).

9. Malumbres, M. & Barbacid, M. Cell cycle, CDKs and cancer: a changing paradigm. *Nat Rev Cancer* **9**, 153-166 (2009).

10. Malumbres, M. Cyclin-dependent kinases. *Genome Biol* **15** (2014).

11. McIntosh, J.R. Mitosis. *Cold Spring Harb Perspect Biol* **8** (2016).

12. Jeppsson, K., Kanno, T., Shirahige, K. & Sjogren, C. The maintenance of chromosome structure: positioning and functioning of SMC complexes. *Nat Rev Mol Cell Biol* **15**, 601-614 (2014).

13. Uhlmann, F. SMC complexes: from DNA to chromosomes. *Nat Rev Mol Cell Biol* **17**, 399-412 (2016).

14. Antonin, W. & Neumann, H. Chromosome condensation and decondensation during mitosis. *Curr Opin Cell Biol* **40**, 15-22 (2016).

15. Ungricht, R. & Kutay, U. Mechanisms and functions of nuclear envelope remodelling. *Nat Rev Mol Cell Biol* **18**, 229-245 (2017).

16. Gascoigne, K.E. & Cheeseman, I.M. Kinetochore assembly: if you build it, they will come. *Curr Opin Cell Biol* **23**, 102-108 (2011).

17. Musacchio, A. & Desai, A. A Molecular View of Kinetochore Assembly and Function. *Biology (Basel)* **6** (2017).

18. Joglekar, A.P. & Kukreja, A.A. How Kinetochore Architecture Shapes the Mechanisms of Its Function. *Curr Biol* **27**, R816-R824 (2017).

19. Fukagawa, T. & Earnshaw, W.C. The centromere: chromatin foundation for the kinetochore machinery. *Dev Cell* **30**, 496-508 (2014).

20. Wandke, C., Barisic, M., Sigl, R., Rauch, V., Wolf, F., Amaro, A.C., Tan, C.H., Pereira, A.J., Kutay, U., Maiato, H., Meraldi, P. & Geley, S. Human chromokinesins promote chromosome congression and spindle microtubule dynamics during mitosis. *J Cell Biol* **198**, 847-863 (2012).

21. Auckland, P. & McAinsh, A.D. Building an integrated model of chromosome congression. *J Cell Sci* **128**, 3363-3374 (2015).

22. Musacchio, A. The Molecular Biology of Spindle Assembly Checkpoint Signaling Dynamics. *Curr Biol* **25**, R1002-1018 (2015).

23. Manic, G., Corradi, F., Sistigu, A., Siteni, S. & Vitale, I. Molecular Regulation of the Spindle Assembly Checkpoint by Kinases and Phosphatases. *Int Rev Cell Mol Biol* **328**, 105-161 (2017).

24. Scholey, J.M., Civelekoglu-Scholey, G. & Brust-Mascher, I. Anaphase B. *Biology (Basel)* **5** (2016).

25. Asbury, C.L. Anaphase A: Disassembling Microtubules Move Chromosomes toward Spindle Poles. *Biology (Basel)* **6** (2017).

26. Hu, C.K., Coughlin, M. & Mitchison, T.J. Midbody assembly and its regulation during cytokinesis. *Mol Biol Cell* **23**, 1024-1034 (2012).

27. Dionne, L.K., Wang, X.J. & Prekeris, R. Midbody: from cellular junk to regulator of cell polarity and cell fate. *Curr Opin Cell Biol* **35**, 51-58 (2015).

28. Barr, F.A. & Gruneberg, U. Cytokinesis: placing and making the final cut. *Cell* **131**, 847-860 (2007).

29. D'Avino, P.P., Giansanti, M.G. & Petronczki, M. Cytokinesis in animal cells. *Cold Spring Harb Perspect Biol* **7**, a015834 (2015).

30. Glotzer, M. The 3Ms of central spindle assembly: microtubules, motors and MAPs. *Nat Rev Mol Cell Biol* **10**, 9-20 (2009).

31. Douglas, M.E. & Mishima, M. Still entangled: assembly of the central spindle by multiple microtubule modulators. *Semin Cell Dev Biol* **21**, 899-908 (2010).

32. Lee, K.Y., Davies, T. & Mishima, M. Cytokinesis microtubule organisers at a glance. *J Cell Sci* **125**, 3495-3500 (2012).

33. Lacroix, B. & Maddox, A.S. Cytokinesis, ploidy and aneuploidy. *J Pathol* **226**, 338-351 (2012).

34. Sivakumar, S. & Gorbsky, G.J. Spatiotemporal regulation of the anaphase-promoting complex in mitosis. *Nat Rev Mol Cell Biol* **16**, 82-94 (2015).

35. Singh, S.A., Winter, D., Kirchner, M., Chauhan, R., Ahmed, S., Ozlu, N., Tzur, A., Steen, J.A. & Steen, H. Co-regulation proteomics reveals substrates and mechanisms of APC/C-dependent degradation. *EMBO J* **33**, 385-399 (2014).

36. Cahu, J., Olichon, A., Hentrich, C., Schek, H., Drinjakovic, J., Zhang, C., Doherty-Kirby, A., Lajoie, G. & Surrey, T. Phosphorylation by Cdk1 increases the binding of Eg5 to microtubules in vitro and in Xenopus egg extract spindles. *PLoS One* **3**, e3936 (2008).

37. Espeut, J., Gaussen, A., Bieling, P., Morin, V., Prieto, S., Fesquet, D., Surrey, T. & Abrieu, A. Phosphorylation relieves autoinhibition of the kinetochore motor Cenp-E. *Mol Cell* **29**, 637-643 (2008).

38. Mollinari, C., Kleman, J.P., Jiang, W., Schoehn, G., Hunter, T. & Margolis, R.L. PRC1 is a microtubule binding and bundling protein essential to maintain the mitotic spindle midzone. *J Cell Biol* **157**, 1175-1186 (2002).

39. Hummer, S. & Mayer, T.U. Cdk1 negatively regulates midzone localization of the mitotic kinesin Mklp2 and the chromosomal passenger complex. *Curr Biol* **19**, 607-612 (2009).

40. Mishima, M., Visnja, P., Gruneberg, U., Nigg, E.A. & Glotzer, M. Cell cycle regulation of central spindle assembly. *Nature* **430**, 908-913 (2004).

41. Voets, E., Marsman, J., Demmers, J., Beijersbergen, R. & Wolthuis, R. The lethal response to Cdk1 inhibition depends on sister chromatid alignment errors generated by KIF4 and isoform 1 of PRC1. *Sci Rep* **5**, 14798 (2015).

42. Lee, K.Y., Esmaeili, B., Zealley, B. & Mishima, M. Direct interaction between centralspindlin and PRC1 reinforces mechanical resilience of the central spindle. *Nat Commun* **6**, 7290 (2015).

43. Franker, M.A. & Hoogenraad, C.C. Microtubule-based transport - basic mechanisms, traffic rules and role in neurological pathogenesis. *J Cell Sci* **126**, 2319-2329 (2013).

44. Lin, S., Liu, M., Mozgova, O.I., Yu, W. & Baas, P.W. Mitotic motors coregulate microtubule patterns in axons and dendrites. *J Neurosci* **32**, 14033-14049 (2012).

45. Reiter, J.F. & Leroux, M.R. Genes and molecular pathways underpinning ciliopathies. *Nat Rev Mol Cell Biol* **18**, 533-547 (2017).

46. Amos, L.A. & Klug, A. Arrangement of Subunits in Flagellar Microtubules. *J Cell Sci* **14**, 523-549 (1974).

47. Nogales, E. An electron microscopy journey in the study of microtubule structure and dynamics. *Protein Sci* **24**, 1912-1919 (2015).

48. Kikkawa, M., Ishikawa, T., Nakata, T., Wakabayashi, T. & Hirokawa, N. Direct visualization of the microtubule lattice seam both in vitro and in vivo. *J Cell Biol* **127**, 1965-1971 (1994).

49. Desai, A. & Mitchison, T.J. Microtubule polymerization dynamics. *Annu Rev Cell Dev Biol* **13**, 83-117 (1997).

50. Mitchison, T.J. & Kirchner, M. Dynamic instability of microtubule growth. *Nature* **312**, 237-242 (1984).

51. Stewart, R.J., Farrell, K.W. & Wilson, L. Role of GTP hydrolysis in microtubule polymerization: evidence for a coupled hydrolysis mechanism. *Biochemistry* **29**, 6489-6498 (1990).

52. Brouhard, G.J. Dynamic instability 30 years later: complexities in microtubule growth and catastrophe. *Mol Biol Cell* **26**, 1207-1210 (2015).

53. Nogales, E. A structural view of microtubule dynamics. *Cell Mol Life Sci* **56**, 133-142 (1999).

54. Akhmanova, A. & Steinmetz, M.O. Control of microtubule organization and dynamics: two ends in the limelight. *Nat Rev Mol Cell Biol* **16**, 711-726 (2015).

55. Al-Bassam, J. & Chang, F. Regulation of microtubule dynamics by TOG-domain proteins XMAP215/Dis1 and CLASP. *Trends Cell Biol* **21**, 604-614 (2011).

56. Howard, J. & Hyman, A.A. Growth, fluctuation and switching at microtubule plus ends. *Nat Rev Mol Cell Biol* **10**, 569-574 (2009).

57. Atherton, J., Jiang, K., Stangier, M.M., Luo, Y., Hua, S., Houben, K., van Hooff, J.J.E., Joseph, A.P., Scarabelli, G., Grant, B.J., Roberts, A.J., Topf, M., Steinmetz, M.O., Baldus, M., Moores, C.A. & Akhmanova, A. A structural model for microtubule minus-end recognition and protection by CAMSAP proteins. *Nat Struct Mol Biol* (2017).

58. Bringmann, H., Skiniotis, G., Spilker, A., Kandels-Lewis, S., Vernos, I. & Surrey, T. A kinesin-like motor inhibits microtubule dynamic instability. *Science* **303**, 1519-1522 (2004).

59. Niwa, S. Kinesin superfamily proteins and the regulation of microtubule dynamics in morphogenesis. *Anat Sci Int* **90**, 1-6 (2015).

60. Voter, W.A. & Erickson, H.P. The kinetics of microtubule assembly. Evidence for a two-stage nucleation mechanism. *J Biol Chem* **259**, 10430-10438 (1984).

61. Wade, R. Characterization of Microtubule Protofilament Numbers. *J Mol Biol* **212**, 775-786 (1990).

62. Hyman, A., Salser, S., Drechsel, D., Unwin, N. & Mitchison, T.J. Role of GTP HYdrolysis in Microtubule Dynamics: Information from a Slowly Hydrolyzable Analogue, GMPCPP. *Mol Biol Cell* **3**, 1155-1167 (1992).

63. Erickson, H.P. & Pantaloni, D. The Role of Subunit Entropy in Cooperative Assembly. *Biophys J* **34**, 293-309 (1981).

64. Brust-Mascher, I. & Scholey, J.M. Mitotic motors and chromosome segregation: the mechanism of anaphase B. *Biochem Soc Trans* **39**, 1149-1153 (2011).

65. Lawrence, C.J., Dawe, R.K., Christie, K.R., Cleveland, D.W., Dawson, S.C., Endow, S.A., Goldstein, L.S., Goodson, H.V., Hirokawa, N., Howard, J., Malmberg, R.L., McIntosh, J.R., Miki, H., Mitchison, T.J., Okada, Y., Reddy, A.S., Saxton, W.M., Schliwa, M., Scholey, J.M., Vale, R.D., Walczak, C.E. & Wordeman, L. A standardized kinesin nomenclature. *J Cell Biol* **167**, 19-22 (2004).

66. Hirokawa, N., Noda, Y., Tanaka, Y. & Niwa, S. Kinesin superfamily motor proteins and intracellular transport. *Nat Rev Mol Cell Biol* **10**, 682-696 (2009).

67. Cross, R.A. & McAinsh, A. Prime movers: the mechanochemistry of mitotic kinesins. *Nat Rev Mol Cell Biol* **15**, 257-271 (2014).

68. She, Z.Y. & Yang, W.X. Molecular mechanisms of kinesin-14 motors in spindle assembly and chromosome segregation. *J Cell Sci* **130**, 2097-2110 (2017).

69. Jha, R. & Surrey, T. Regulation of processive motion and microtubule localization of cytoplasmic dynein. *Biochem Soc Trans* **43**, 48-57 (2015).

70. Cianfrocco, M.A., DeSantis, M.E., Leschziner, A.E. & Reck-Peterson, S.L. Mechanism and regulation of cytoplasmic dynein. *Annu Rev Cell Dev Biol* **31**, 83-108 (2015).

71. Hizlan, D., Mishima, M., Tittmann, P., Gross, H., Glotzer, M. & Hoenger, A. Structural analysis of the ZEN-4/CeMKLP1 motor domain and its interaction with microtubules. *J Struct Biol* **153**, 73-84 (2006).

72. van Riel, W.E., Rai, A., Bianchi, S., Katrukha, E.A., Liu, Q., Heck, A.J., Hoogenraad, C.C., Steinmetz, M.O., Kapitein, L.C. & Akhmanova, A. Kinesin-4 KIF21B is a potent microtubule pausing factor. *Elife* **6** (2017).

73. Gigant, B., Wang, W., Dreier, B., Jiang, Q., Pecqueur, L., Pluckthun, A., Wang, C. & Knossow, M. Structure of a kinesin-tubulin complex and implications for kinesin motility. *Nat Struct Mol Biol* **20**, 1001-1007 (2013).

74. Hentrich, C. & Surrey, T. Microtubule organization by the antagonistic mitotic motors kinesin-5 and kinesin-14. *J Cell Biol* **189**, 465-480 (2010).

75. Ems-McClung, S.C. & Walczak, C.E. Kinesin-13s in mitosis: Key players in the spatial and temporal organization of spindle microtubules. *Semin Cell Dev Biol* **21**, 276-282 (2010).

76. Bieling, P., Telley, I.A. & Surrey, T. A minimal midzone protein module controls formation and length of antiparallel microtubule overlaps. *Cell* **142**, 420-432 (2010).

77. Subramanian, R., Ti, S.C., Tan, L., Darst, S.A. & Kapoor, T.M. Marking and measuring single microtubules by PRC1 and kinesin-4. *Cell* **154**, 377-390 (2013).

78. Kurasawa, Y., Earnshaw, W.C., Mochizuki, Y., Dohmae, N. & Todokoro, K. Essential roles of KIF4 and its binding partner PRC1 in organized central spindle midzone formation. *EMBO J* **23**, 3237-3248 (2004).

79. Hu, C.K., Coughlin, M., Field, C.M. & Mitchison, T.J. KIF4 regulates midzone length during cytokinesis. *Curr Biol* **21**, 815-824 (2011).

80. Du, Y., English, C.A. & Ohi, R. The kinesin-8 Kif18A dampens microtubule plus-end dynamics. *Curr Biol* **20**, 374-380 (2010).

81. Stumpff, J., Wagenbach, M., Franck, A., Asbury, C.L. & Wordeman, L. Kif18A and chromokinesins confine centromere movements via microtubule growth suppression and spatial control of kinetochore tension. *Dev Cell* **22**, 1017-1029 (2012).

82. Mayr, M.I., Hummer, S., Bormann, J., Gruner, T., Adio, S., Woehlke, G. & Mayer, T.U. The human kinesin Kif18A is a motile microtubule depolymerase essential for chromosome congression. *Curr Biol* **17**, 488-498 (2007).

83. Varga, V., Helenius, J., Tanaka, K., Hyman, A.A., Tanaka, T.U. & Howard, J. Yeast kinesin-8 depolymerizes microtubules in a length-dependent manner. *Nat Cell Biol* **8**, 957-962 (2006).

84. White, E.A. & Glotzer, M. Centralspindlin: at the heart of cytokinesis. *Cytoskeleton (Hoboken)* **69**, 882-892 (2012).

85. Mishima, M., Kaitna, S. & Glotzer, M. Central spindle assembly and cytokinesis require a kinesin-like protein/RhoGAP complex with microtubule bundling activity. *Dev Cell* **2**, 41-54 (2002).

86. White, E.A., Raghuraman, H., Perozo, E. & Glotzer, M. Binding of the CYK-4 subunit of the centralspindlin complex induces a large scale conformational change in the kinesin subunit. *J Biol Chem* **288**, 19785-19795 (2013).

87. Davies, T., Kodera, N., Kaminski Schierle, G.S., Rees, E., Erdelyi, M., Kaminski, C.F., Ando, T. & Mishima, M. CYK4 promotes antiparallel microtubule bundling by optimizing MKLP1 neck conformation. *PLoS Biol* **13**, e1002121 (2015).

88. Matuliene, J., Kuriyama, R. & Pollard, T.D. Kinesin-like Protein CHO1 Is Required for the Formation of Midbody Matrix and the Completion of Cytokinesis in Mammalian Cells. *Molecular Biology of the Cell* **13**, 1832-1845 (2002).

89. Zhao, W.M. & Fang, G. MgcRacGAP controls the assembly of the contractile ring and the initiation of cytokinesis. *Proc Natl Acad Sci U S A* **102**, 13158-13163 (2005).

90. Lekomtsev, S., Su, K.C., Pye, V.E., Blight, K., Sundaramoorthy, S., Takaki, T., Collinson, L.M., Cherepanov, P., Divecha, N. & Petronczki, M. Centralspindlin links the mitotic spindle to the plasma membrane during cytokinesis. *Nature* **492**, 276-279 (2012).

91. Hutterer, A., Glotzer, M. & Mishima, M. Clustering of centralspindlin is essential for its accumulation to the central spindle and the midbody. *Curr Biol* **19**, 2043-2049 (2009).

92. Douglas, M.E., Davies, T., Joseph, N. & Mishima, M. Aurora B and 14-3-3 coordinately regulate clustering of centralspindlin during cytokinesis. *Curr Biol* **20**, 927-933 (2010).

93. Gruneberg, U., Neef, R., Honda, R., Nigg, E.A. & Barr, F.A. Relocation of Aurora B from centromeres to the central spindle at the metaphase to anaphase transition requires MKlp2. *J Cell Biol* **166**, 167-172 (2004).

94. Kitagawa, M., Fung, S.Y., Onishi, N., Saya, H. & Lee, S.H. Targeting Aurora B to the equatorial cortex by MKlp2 is required for cytokinesis. *PLoS One* **8**, e64826 (2013).

95. Afonso, O., Figueiredo, A.C. & Maiato, H. Late mitotic functions of Aurora kinases. *Chromosoma* **126**, 93-103 (2017).

96. Duellberg, C., Fourniol, F.J., Maurer, S.P., Roostalu, J. & Surrey, T. End-binding proteins and Ase1/PRC1 define local functionality of structurally distinct parts of the microtubule cytoskeleton. *Trends Cell Biol* **23**, 54-63 (2013).

97. Jiang, W., Jimenez, G., Wells, N.J., Hope, T.J., Wahl, G.M., Hunter, T. & Fukunaga, R. PRC1: a human mitotic spindle-associated CDK substrate protein required for cytokinesis. *Mol Cell* **2**, 877-885 (1998).

98. Kellogg, E.H., Howes, S., Ti, S.C., Ramirez-Aportela, E., Kapoor, T.M., Chacon, P. & Nogales, E. Near-atomic cryo-EM structure of PRC1 bound to the microtubule. *PNAS* **113**, 9430-9439 (2016).

99. Subramanian, R., Wilson-Kubalek, E.M., Arthur, C.P., Bick, M.J., Campbell, E.A., Darst, S.A., Milligan, R.A. & Kapoor, T.M. Insights into antiparallel microtubule crosslinking by PRC1, a conserved nonmotor microtubule binding protein. *Cell* **142**, 433-443 (2010).

100. Liu, J., Wang, Z., Jiang, K., Zhang, L., Zhao, L., Hua, S., Yan, F., Yang, Y., Wang, D., Fu, C., Ding, X., Guo, Z. & Yao, X. PRC1 cooperates with CLASP1 to organize central spindle plasticity in mitosis. *J Biol Chem* **284**, 23059-23071 (2009).

101. Gruneberg, U., Neef, R., Li, X., Chan, E.H., Chalamalasetty, R.B., Nigg, E.A. & Barr, F.A. KIF14 and citron kinase act together to promote efficient cytokinesis. *J Cell Biol* **172**, 363-372 (2006).

102. Inoue, Y.H., Savoian, M.S., Suzuki, T., Mathe, E., Yamamoto, M.T. & Glover, D.M. Mutations in orbit/mast reveal that the central spindle is comprised of two microtubule populations, those that initiate cleavage and those that propagate furrow ingression. *J Cell Biol* **166**, 49-60 (2004).

103. Uehara, R. & Goshima, G. Functional central spindle assembly requires de novo microtubule generation in the interchromosomal region during anaphase. *J Cell Biol* **191**, 259-267 (2010).

104. Uehara, R., Kamasaki, T., Hiruma, S., Poser, I., Yoda, K., Yajima, J., Gerlich, D.W. & Goshima, G. Augmin shapes the anaphase spindle for efficient cytokinetic furrow ingression and abscission. *Molecular Biology of the Cell* **27**, 812-827 (2016).

105. Hsia, K.C., Wilson-Kubalek, E.M., Dottore, A., Hao, Q., Tsai, K.L., Forth, S., Shimamoto, Y., Milligan, R.A. & Kapoor, T.M. Reconstitution of the augmin complex provides insights into its architecture and function. *Nat Cell Biol* **16**, 852-863 (2014).

106. Petry, S., Groen, A.C., Ishihara, K., Mitchison, T.J. & Vale, R.D. Branching microtubule nucleation in Xenopus egg extracts mediated by augmin and TPX2. *Cell* **152**, 768-777 (2013).

107. Canman, J.C., Hoffman, D.B. & Salmon, E.D. The role of pre- and post-anaphase microtubules in the cytokinesis phase of the cell cycle. *Current Biology* **10**, 611-614 (2000).

108. Nguyen, P.A., Groen, A.C., Loose, M., Ishihara, K., Wühr, M., Field, C.M. & Mitchison, T.J. Spatial organization of cytokinesis signaling reconstituted in a cell-free system. *Science* **346**, 244-247 (2014).

109. Baumann, H. & Surrey, T. Motor-mediated cortical versus astral microtubule organization in lipid-monolayered droplets. *J Biol Chem* **289**, 22524-22535 (2014).

110. Loughlin, R., Wilbur, J.D., McNally, F.J., Nedelec, F.J. & Heald, R. Katanin contributes to interspecies spindle length scaling in Xenopus. *Cell* **147**, 1397-1407 (2011).

111. Sharp, D.J., McDonald, K.L., Brown, H.M., Matthies, H.J., Walczak, C., Vale, R.D., Mitchison, T.J. & Scholey, J.M. The Bipolar Kinesin, KLP61F, Cross-links Microtubules within Interpolar Microtubule Bundles of Drosophila Embryonic Mitotic Spindles. *J. Cell Biol.* **144**, 125-138 (1999).

112. Wang, H., Brust-Mascher, I., Civelekoglu-Scholey, G. & Scholey, J.M. Patronin mediates a switch from kinesin-13-dependent poleward flux to anaphase B spindle elongation. *J Cell Biol* **203**, 35-46 (2013).

113. Laan, L., Pavin, N., Husson, J., Romet-Lemonne, G., van Duijn, M., Lopez, M.P., Vale, R.D., Julicher, F., Reck-Peterson, S.L. & Dogterom, M. Cortical dynein controls microtubule dynamics to generate pulling forces that position microtubule asters. *Cell* **148**, 502-514 (2012).

114. Mastronarde, D.N., McDonald, K.L., Ding, R. & McIntosh, J.R. Interpolar spindle microtubules in PTK cells. *J Cell Biol* **123**, 1475-1489 (1993).

115. Nahaboo, W., Zouak, M., Askjaer, P. & Delattre, M. Chromatids segregate without centrosomes during Caenorhabditis elegans mitosis in a Ran- and CLASP-dependent manner. *Mol Biol Cell* **26**, 2020-2029 (2015).

116. Maton, G., Edwards, F., Lacroix, B., Stefanutti, M., Laband, K., Lieury, T., Kim, T., Espeut, J., Canman, J.C. & Dumont, J. Kinetochore components are required for central spindle assembly. *Nat Cell Biol* **17**, 697-705 (2015).

117. Ban, R., Irino, Y., Fukami, K. & Tanaka, H. Human mitotic spindle-associated protein PRC1 inhibits MgcRacGAP activity toward Cdc42 during the metaphase. *J Biol Chem* **279**, 16394-16402 (2004).

118. Kim, H., Guo, F., Brahma, S., Xing, Y. & Burkard, M.E. Centralspindlin assembly and 2 phosphorylations on MgcRacGAP by Polo-like kinase 1 initiate Ect2 binding in early cytokinesis. *Cell Cycle* **13**, 2952-2961 (2014).

119. Yuce, O., Piekny, A. & Glotzer, M. An ECT2-centralspindlin complex regulates the localization and function of RhoA. *J Cell Biol* **170**, 571-582 (2005).

120. Braun, M., Lansky, Z., Fink, G., Ruhnow, F., Diez, S. & Janson, M.E. Adaptive braking by Ase1 prevents overlapping microtubules from sliding completely apart. *Nat Cell Biol* **13**, 1259-1264 (2011).

121. Lansky, Z., Braun, M., Ludecke, A., Schlierf, M., ten Wolde, P.R., Janson, M.E. & Diez, S. Diffusible crosslinkers generate directed forces in microtubule networks. *Cell* **160**, 1159-1168 (2015).

122. Saxton, W.M. & McIntosh, J.R. Interzone microtubule behavior in late anaphase and telophase spindles. *J Cell Biol* **105**, 875-886 (1987).

123. Aist, J.R., Liang, H. & Berns, M.W. Astral and spindle forces in PtK2 cells during anaphase B: a laser microbeam study. *J Cell Sci* **104**, 1207-1216 (1993).

124. Collins, E., Mann, B.J. & Wadsworth, P. Eg5 restricts anaphase B spindle elongation in mammalian cells. *Cytoskeleton (Hoboken)* **71**, 136-144 (2014).

125. Shimamoto, Y., Forth, S. & Kapoor, T.M. Measuring Pushing and Braking Forces Generated by Ensembles of Kinesin-5 Crosslinking Two Microtubules. *Dev Cell* **34**, 669-681 (2015).

126. Liu, Y., Zhang, Z., Liang, H., Zhao, X., Liang, L., Wang, G., Yang, J., Jin, Y., McNutt, M.A. & Yin, Y. Protein Phosphatase 2A (PP2A) Regulates EG5 to Control Mitotic Progression. *Sci Rep* **7**, 1630 (2017).

127. Kajtez, J., Solomatina, A., Novak, M., Polak, B., Vukusic, K., Rudiger, J., Cojoc, G., Milas, A., Sumanovac Sestak, I., Risteski, P., Tavano, F., Klemm, A.H., Roscioli, E., Welburn, J., Cimini, D., Gluncic, M., Pavin, N. & Tolic, I.M. Overlap microtubules link sister k-fibres and balance the forces on bi-oriented kinetochores. *Nat Commun* **7**, 10298 (2016).

128. Vukusic, K., Buda, R., Bosilj, A., Milas, A., Pavin, N. & Tolic, I.M. Microtubule Sliding within the Bridging Fiber Pushes Kinetochore Fibers Apart to Segregate Chromosomes. *Dev Cell* **43**, 11-23 e16 (2017).

129. Lee, Y.M., Lee, S., Lee, E., Shin, H., Hahn, H., Choi, W. & Wankee, K. Human kinesin superfamily member 4 is dominantly localized in the nuclear matrix and is associated with chromosomes during mitosis. *Biochem J* **360**, 549-556 (2001).

130. Tipton, A.R., Wren, J.D., Daum, J.R., Siefert, J.C. & Gorbsky, G.J. GTSE1 regulates spindle microtubule dynamics to control Aurora B kinase and Kif4A chromokinesin on chromosome arms. *J Cell Biol* **216**, 3117-3132 (2017).

131. Nunes Bastos, R., Gandhi, S.R., Baron, R.D., Gruneberg, U., Nigg, E.A. & Barr, F.A. Aurora B suppresses microtubule dynamics and limits central spindle size by locally activating KIF4A. *J Cell Biol* **202**, 605-621 (2013).

132. Li, Q.-R., Yan, X.-M., Guo, L., Li, J. & Zang, Y. AMPK regulates anaphase central spindle length by phosphorylation of KIF4A. *Journal of Molecular Cell Biology*, 1-16 (2017).

133. Zhu, C. & Jiang, W. Cell cycle-dependent translocation of PRC1 on the spindle by Kif4 is essential for midzone formation and cytokinesis. *Proc Natl Acad Sci U S A* **102**, 343-348 (2005).

134. Shrestha, S., Wilmeth, L.J., Eyer, J. & Shuster, C.B. PRC1 controls spindle polarization and recruitment of cytokinetic factors during monopolar cytokinesis. *Mol Biol Cell* **23**, 1196-1207 (2012).

135. Shannon, K.B., Canman, J.C., Moree, C.B., Tirnauer, J.S. & Salmon, E.D. Taxol-stabilized Microtubules Can Position the Cytokinetic Furrow in Mammalian Cells. *Mol Biol Cell* **16**, 4423-4436 (2005).

136. Axelrod, D., Thompson, N.L. & Bughardt, P. Total Internal FLuorescent Microscopy. *J Microscopy* **129**, 19-28 (1982).

137. Sanchez, T., Chen, D.T., DeCamp, S.J., Heymann, M. & Dogic, Z. Spontaneous motion in hierarchically assembled active matter. *Nature* **491**, 431-434 (2012).

138. Castoldi, M. & Popov, A.V. Purification of brain tubulin through two cycles of polymerization–depolymerization in a high-molarity buffer. *Protein Expression and Purification* **32**, 83-88 (2003).

139. Hyman, A., Drechsel, D., Kellogg, D., Salser, S., Sawin, K., Steffen, P., Wordeman, L. & Mitchison, T.J. Preparation of modified tubulins. *Methods Enzymol* **196**, 478-485 (1991).

140. Chen, I.P., Lai, M.-Y. & Wang, L.-L. An improvement in the moment-preserving thresholding method. *International Journal of Imaging Systems and Technology* **18**, 365-370 (2008).

141. Faivre-Moskalenko, C. & Dogterom, M. Dynamics of microtubule asters in microfabricated chambers: the role of catastrophes. *Proc Natl Acad Sci U S A* **99**, 16788-16793 (2002).

142. Cai, S., Weaver, L.N., Ems-McClung, S.C. & Walczak, C.E. Proper organization of microtubule minus ends is needed for midzone stability and cytokinesis. *Curr Biol* **20**, 880-885 (2010).